博 士 論 文

Atomistic simulations of microstructural evolution in crystalline materials and the extension of their timescale based on state-to-state dynamics

（結晶性材料中微細組織発達の原子論的シミュレーションと
State-to-state ダイナミクスに基づくその時間スケールの拡張）

Sho Hayakawa

早 川　 頌

Atomistic simulations of microstructural evolution in crystalline materials and the extension of their timescale based on state-to-state dynamics

（結晶性材料中微細組織発達の原子論的シミュレーションと
State-to-state ダイナミクスに基づくその時間スケールの拡張）

Sho Hayakawa

A dissertation submitted in partial fulfillment of
the requirements for the degree of

Doctor of Philosophy

Department of Systems Innovation
School of Engineering
University of Tokyo

May 2019

Acknowledgements

I am deeply indebted to many people. Every amount of support from them was indispensable to making this dissertation a reality.

First, I would like to express my deepest appreciation to Prof. Taira Okita, who provided an immeasurable amount of advice, encouragement, and support to me. It has been a great honor and pleasure to work under his supervision. I owe what I am today as a scientist to him.

I am grateful to Dr. Mitsuhiro Itakura. He has provided numerous insightful comments and suggestions, which have always enriched my research. I would like to express my gratitude to Dr. Yuri N. Osetsky, Prof. Haixuan Xu, and Dr. Sutatch Ratanaphan. The research collaborations with them were valuable experiences to me; they motivated me to work on a global stage. I will never forget their friendly hospitality.

I would like to thank the members of Okita Laboratory: Junichi Hirabayashi, Yujiro Hayashi, Yingjuan Yang, Takahumi Dojo, Kohei Doihara, Yilun Hu, Ridong Du, Guangyou Qiang, Akihide Kawamitsu, Kota Ninomiya, Kyosuke Shibasaki, Yukiya Adachi, Satoshi Terayama, Yuki Iwase, Takao Baba, and Asako Natsuaki. The fruitful discussions and daily conversations with them have made my graduate study an enjoyable journey. I also convey my thanks to Motohiro Sato and Masataka Ishihara for supporting my research with beers in their hands.

Last but not the least, I would like to express my sincere gratitude to my family. Without their love, support, and understanding throughout my life, I could have not come this far.

Table of contents

List of Figures

List of Tables

Abbreviations

MD: Molecular dynamics

SIA: Self-interstitial atom

PES: Potential energy surface

FEM: Finite element method

DRE: Dual resolution element

kMC: kinetic Monte Carlo

OKMC: Objective kinetic Monte Carlo

AKMC: Atomistic kinetic Monte Carlo

MEP: Minimum energy path

FCC: Face-centered cubic

SFE: Stacking fault energy

SP: Saddle point

SEAKMC: Self-evolving atomistic kinetic Monte Carlo

SPS: Saddle point search

AV: Active volume

EM/BCS: Energy minimization with basins-constructed space

TPSA: Temperature parallel simulated annealing

BCC: Body-centered cubic

PKA: Primary knock-on atom

SFT: Stacking fault tetrahedron

TEM: Transmission electron microscopy

CNA: Common neighbor analysis

HCP: Hexagonal close-packed

MS: Molecular statics

LAMMPS: Large-scale atomic/molecular massively parallel simulator

EAM: Embedded atom method

SA: Simulated annealing

Chapter 1 Introduction

1.1 Overall Background

In modern society, there are numerous large artifact systems, such as electric power plants and ships. These systems are deeply connected to our lives, such that we can say that modern society cannot be developed without them. Therefore, failure of artifact systems can directly lead to the collapse of the sustainability of society; consequently, the improvement and reinforcement of these systems based on scientific knowledge are essential. The integrity of structural materials in artifact systems is key for their safe operation. Further, these structural materials are used under certain objectives and conditions; further complications are imposed because these objectives and conditions can drastically change in accordance with the social environment [1]. For instance, structural materials can be exposed to external forces beyond our initial estimation owing to natural disasters; a change in the operating purpose of the system due to extreme competition and demand fluctuations can subject structural materials to inappropriate conditions without our realization. Hence, analysis of the use state of a material based on the design at the point of initial construction and the conventional maintenance engineering is not sufficient to ensure the integrity of structural materials.

These considerations motivate us to employ computational approaches. To investigate the change in material properties through simulation, it is necessary to develop multiscale modeling schemes which encompass various lengthscales and timescales. This is because material degradation phenomena in real situations occur far beyond atomistic scales, while the behavior of microstructures, which are smaller than the meshes used for discretization, governs the property changes in materials. Meanwhile, the lengthscales and timescales in each simulation method are varied over different scales, and no simulation method continuously covers all the scales. Hence, schemes that bridge the scale gap between each method are necessary in addition to the simulation methods themselves (Figure 1.1). In particular, given that the behavior of microstructures is primarily responsible for changes in material properties, as stated above, the schemes need to seamlessly bridge the scale gaps from atomistic scales. The construction of multi-scale modeling schemes contributes not only

to a comprehensive understanding of material behaviors but also to their prediction in future operating conditions based on the current state of the materials. Therefore, the development and improvement of these schemes are necessary for achieving a breakthrough in conventional simulation schemes.

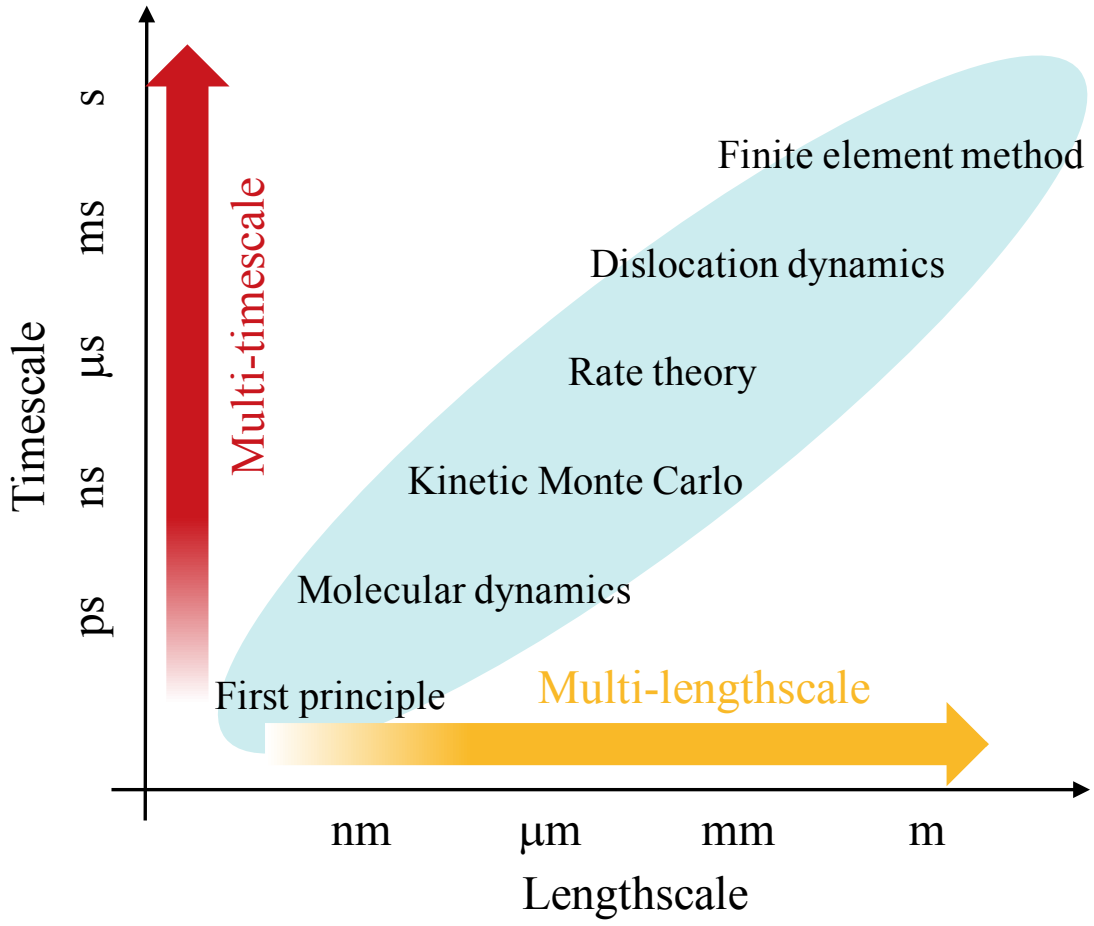

Figure 1.1 Conventional simulation methods and their corresponding lengthscales and timescales.

Molecular dynamics (MD) is a strong tool to investigate material behaviors in atomistic scales. MD is a numerical simulation method, where the dynamics of atoms are described by calculating the interatomic forces (Figure 1.2). Depending on the manner used to derive the interatomic forces, MD simulations are categorized into two groups, i.e., first principle MD and classical MD. In first principle MD, the behavior of electrons is derived based on *ab initio*

calculations, and the interatomic forces are calculated with very high precision. However, the calculation costs tend to be fairly high. Because the cost increases in proportion to $N^{3–4}$ (N: number of atoms in the system), the system size is usually limited to hundreds of atoms. Meanwhile, in classical MD, the interatomic forces are derived with the interatomic potential function, which is fitted to experimental data and first principle calculation results. If the interatomic potential function has sufficient accuracy, classical MD can simulate the correct dynamics of much larger systems than that in first principle MD because the calculation cost increases only in proportion to N via using the concept of the cutoff radius around atoms. Owing to the potential and wide applicability, classical MD simulations have been extensively employed not only in materials science but also in many other fields [2–9]. Note that we mainly focus on classical MD in this dissertation because several previous studies have shown that classical MD exhibits sufficient accuracy in most applications for pure iron and pure copper, which are the materials systems examined in this dissertation. Hereafter, the term “MD” is used to denote classical MD.

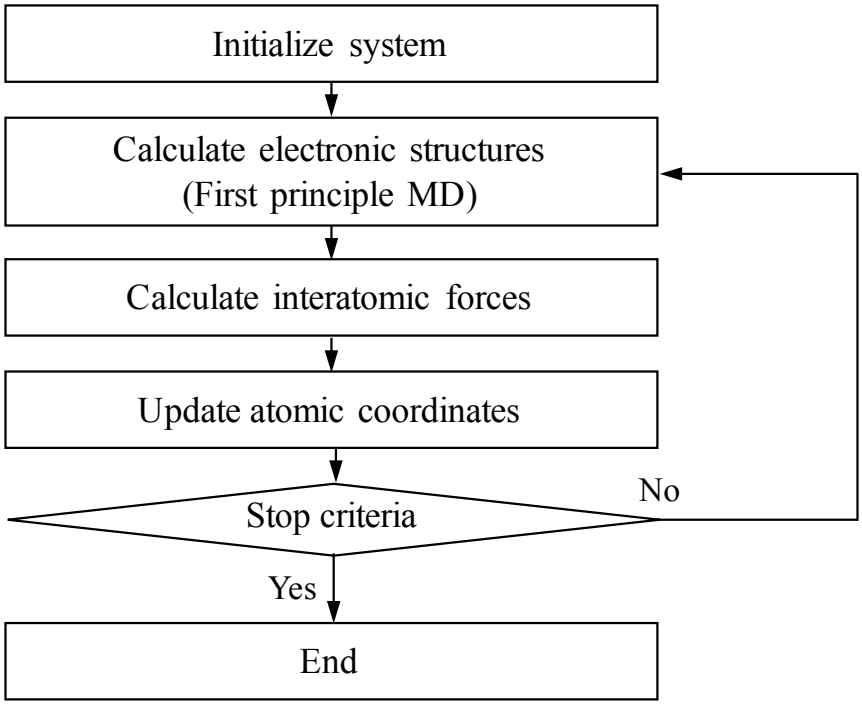

Figure 1.2 Flowchart of MD.

MD simulations have played an important role for many decades in understanding the microstructural behavior of structural materials. The structural materials employed in nuclear

power plants, for instance, are good examples where MD is primarily employed. It has been known that microstructural evolution in nuclear materials under irradiation occurs mainly in four phases in terms of the timescale (Figure 1.3): in the collision phase, neutrons strike atoms in the material, causing displacement of the atoms from their lattice sites – this results in the generation of numerous defects, such as self-interstitial atoms (SIAs) and vacancies (displacement cascade); in the cooling phase, the kinetic energies of the atoms in the cascade core region dissipate into the surrounding area, and most defects disappear through recombination events with the opposite type of defects; in the thermal phase, the surviving defects diffuse and interact with other defects, which can create defect clusters or undergo recombination events; in the diffusion phase, the surviving defects further diffuse beyond the original cascade region and interact with defects produced by other displacement cascades [10]. Many studies have confirmed that the defects and defect clusters produced under irradiation can cause severe degradation in material properties. Previous MD studies have shown that defect clusters can impede dislocation motion, leading to an increase in the yield stress (Figure 1.4) [11–15]. Therefore, it is very important to understand microstructural evolution under irradiation. As shown in Figure 1.3, the timescale of the microstructural evolution spans from femtoseconds to milliseconds; the change in the material properties can occur at even longer timescales, even on the order of years in some cases. Here, it should be highlighted that these multi-timescale phenomena originate from displacement cascades, which occur at a timescale on the order of 10^{-15} s, rendering their investigation by experimental approaches impractical. This indicates that MD is an essential technique to model the microstructural evolution under irradiation from the very beginning of the process. Therefore, numerous MD simulations have been conducted to elucidate the mechanism of defect formation under irradiation [10,16–21]. Moreover, extended MD techniques, such as machine-learning MD, where interatomic forces are derived with machine learning techniques [22], are now being extensively studied and developed. It is expected that MD simulations will be used more often in various fields in the future.

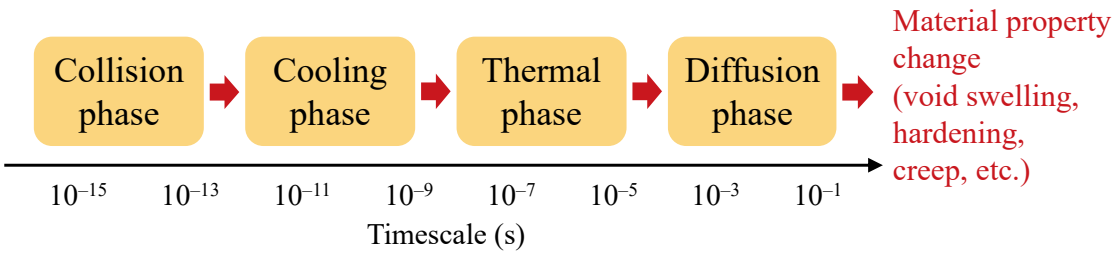

Figure 1.3 Schematic explanation of the timescales of microstructural evolution under irradiation.

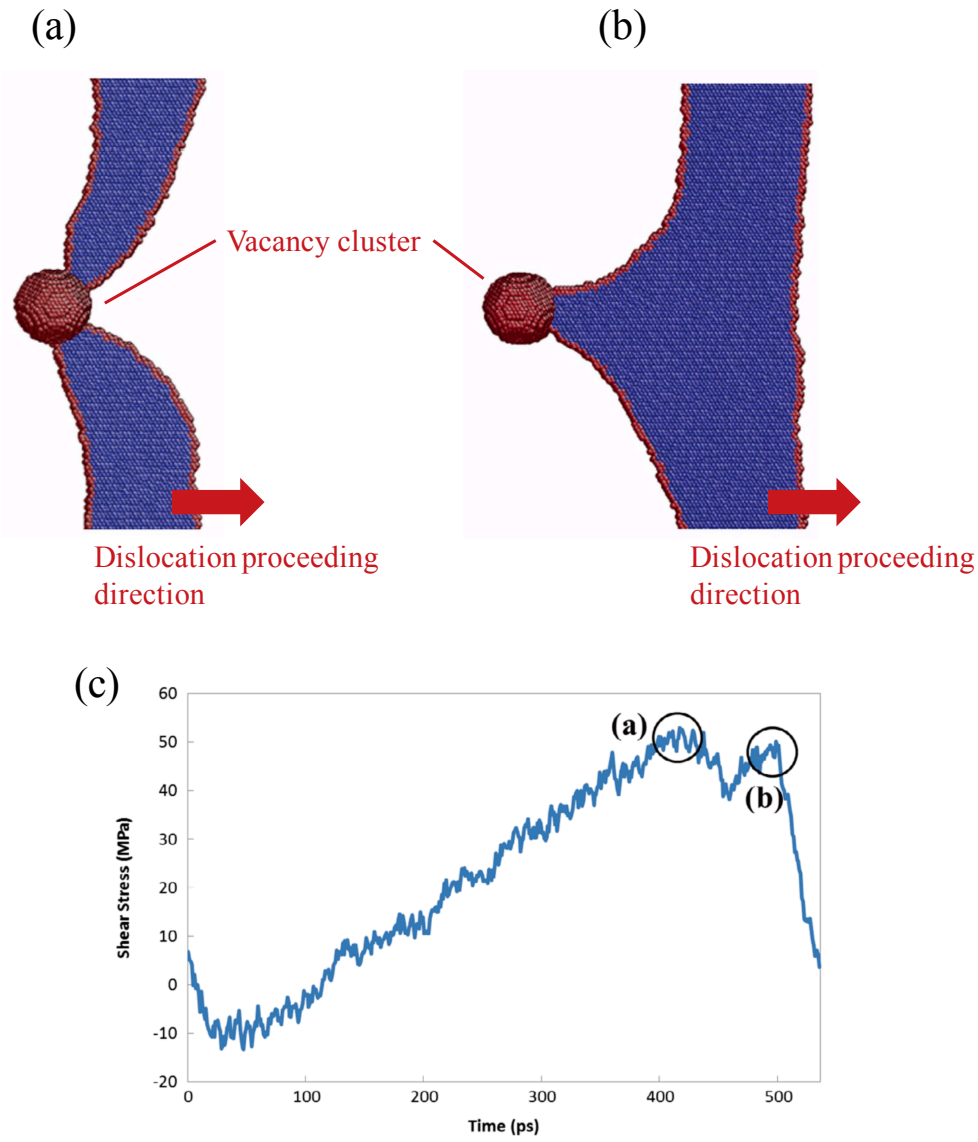

Figure 1.4 (a) and (b) Interaction between an edge dislocation and vacancy cluster in MD simulations, and (c) history of the applied shear stress during the interaction [12].

Every atomic vibration is tracked at each step in MD simulations; consequently, the size of the timestep needs to be of the order of 10^{-15} s to accurately describe the atomic vibrations, whose frequency is ~10^{12}–10^{13} Hz. This poses a limitation in the dynamics that MD can simulate. For instance, defects generated under irradiation diffuse in materials in the thermal and diffusion phases (Figure 1.3), and the required energy barrier (E_a) for typical diffusion event varies around 1.0 eV. Considering that the frequency (ν) of an event with a certain E_a at temperature, T, can be weighted by the Boltzmann factor, ν is described as:

$$\nu = A \exp\left(-\frac{E_a}{k_B T}\right) \tag{1.1}$$

where, A and k_B denote a pre-exponential factor and the Boltzmann constant, respectively. A is typically treated as a constant parameter independent of T. The specific value of A is usually ~10^{12}–10^{13}, and is set to be 10^{12}, here. By considering the reciprocal of ν, we can obtain the average waiting time (t_w) for the occurrence of a certain event with E_a:

$$t_w = \nu^{-1} = A^{-1}\exp\left(\frac{E_a}{k_B T}\right). \tag{1.2}$$

For instance, an event with E_a = 1.0 eV at 600 K (operating temperature of light water reactors) is calculated as ~10^{-4} s. This indicates that, when the timestep interval is set to 10^{-15} s, as many as ~10^{11} MD simulation steps are necessary to simulate the dynamics involving diffusion, which is a critical dynamics to understanding the microstructural evolution in materials. In addition, t_w values of an event with E_a = 1.0 eV at various temperatures from 200 K to 1000 K are shown in Figure 1.5. Note that the region of the typical timescale of MD simulations is illustrated in yellow, where the maximum simulation step is ~10^8 with a timestep interval of 10^{-15} s in most cases. The event cannot be sufficiently simulated in MD simulations even if the temperature is raised to 1000 K, which is higher than half the melting point of pure iron. These considerations demonstrate that it is unfeasible to simulate meso-timescale phenomena, such as diffusion, using the MD technique alone.

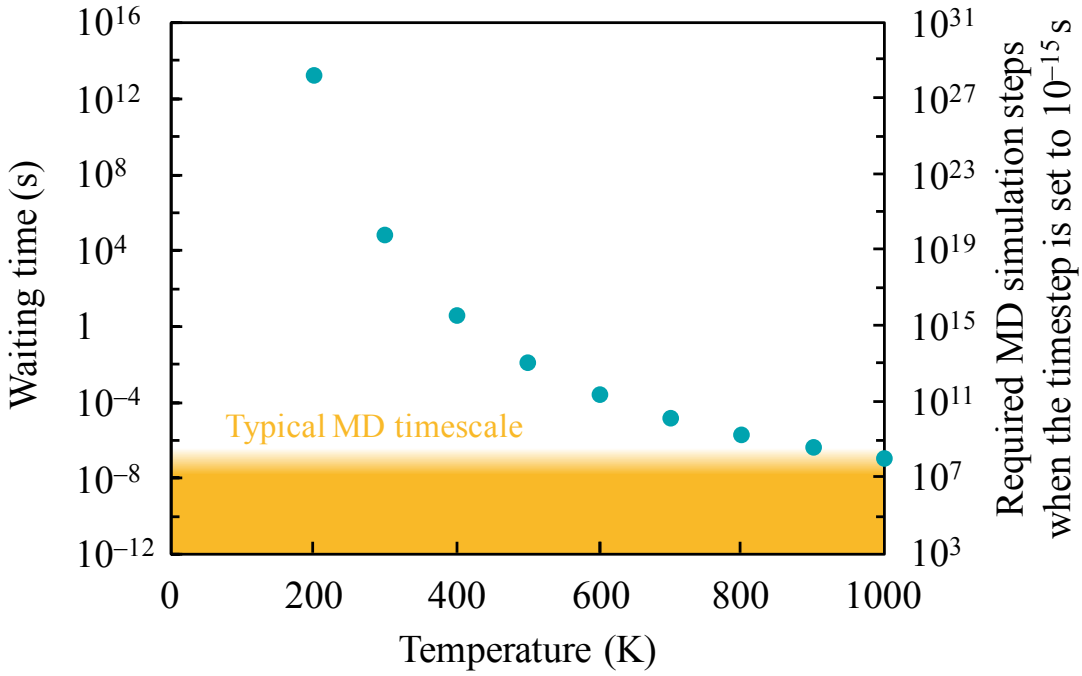

Figure 1.5 Values of t_w of an event with E_a = 1.0 eV at various values of T.

One potential solution to the MD timescale problem is to rely on the rapid improvement in the performance of supercomputers in recent decades. Figure 1.6 shows the performance development of supercomputing power since 1994 [23]. The performance has been improving exponentially with time, almost following Moore's law, according to which the number of transistors in a dense integrated circuit doubles about every 1.5 years [24]. If the supercomputing performance continues to improve with Moore's law, the computational ability will be improved by a factor of approximately ten every 5 years. Even under such an optimistic assumption, however, MD techniques will only enable us to simulate one occurrence of a phenomenon with E_a = 1.0 eV at room temperature, over 40 years from now.

To accelerate conventional MD simulations, some previous studies have developed so-called accelerated MD techniques [25–29]. For instance, metadynamics [26] and hyperdynamics [27] introduce a bias potential to modify the potential energy surface (PES), which renders the frequency of occurrence of rare events quite high. In addition, temperature accelerated dynamics [29] increases the simulation temperature to enhance the occurrence of infrequent events, and then advances the simulated time in accordance with frequency at the low target temperature. These techniques can reach much longer timescales than can be obtained in conventional MD. Still, the accessible timescale is relatively limited because

atomic vibrations need to be accurately tracked.

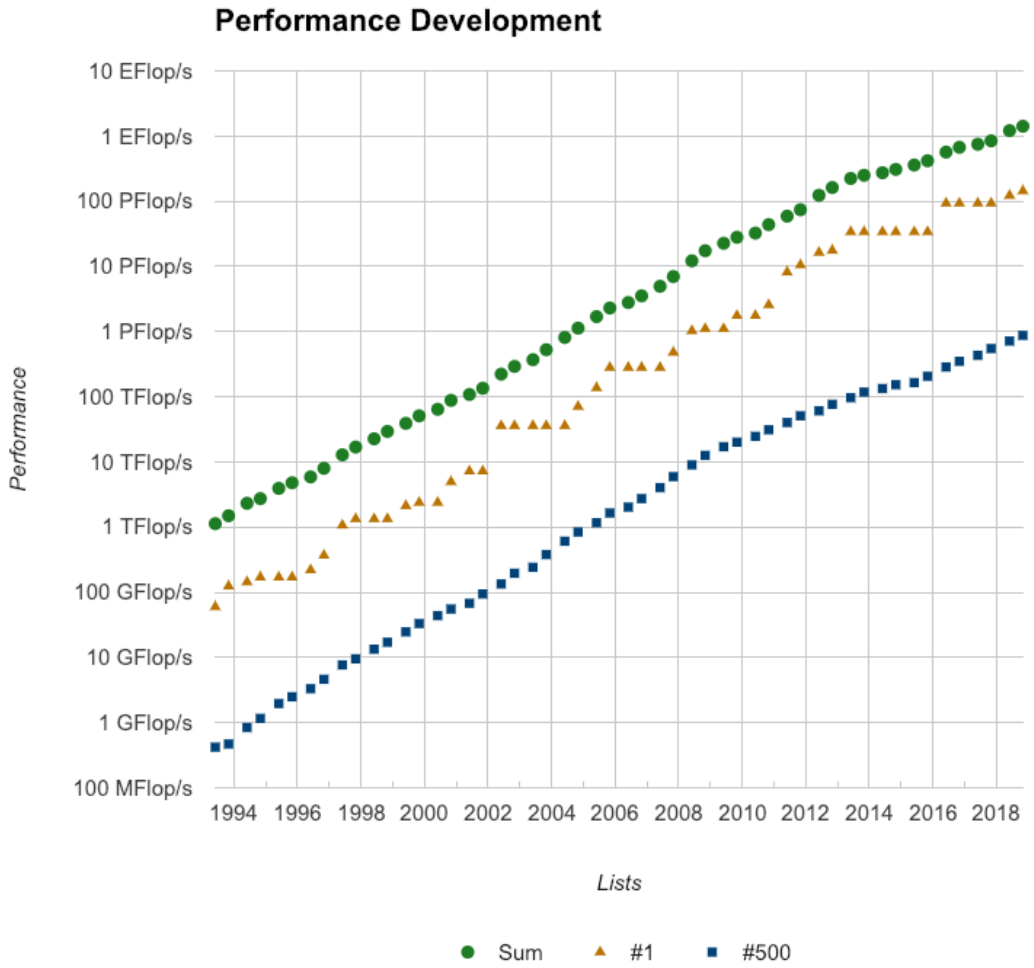

Figure 1.6 Performance development of supercomputing power in recent decades [23].

The scale limitation in MD is also a serious problem for lengthscales. As mentioned above, the MD calculation cost increases in proportion to the number of atoms in the simulation cell. This restricts the system size to ~10,000,000 atoms typically, which corresponds to a cubic cell with an edge length of tens of nanometers. We note that the calculation cost increases drastically with an increase in the edge length because the number of atoms in the cell increases in proportion to the third power of the edge length. Importantly, even under the assumption of Moore's low, the available edge length is only extended to tens of micrometers, even 40–50 years from now.

Based on this, some pioneering studies have focused on extending the MD lengthscale

since the 1990s, by introducing the finite element method (FEM) to MD, in a scheme termed "MD-FEM concurrent coupling" [30]. In this scheme, regions disordered due to the presence of defects are treated with atomistic approaches, while regions close to the structure of a perfect lattice are treated with continuum modeling approaches. The key aspect of this hybrid scheme is the manner in which the two regions are connected while maintaining physical consistency. Kohlhoff et al. [30] set the transition region between the MD region and FEM region, where the atoms and nodes impose displacement boundary conditions each other. Broughton et al. [31] employed an approximation whereby the Hamiltonian on the MD-FEM boundary region is described as the average of the MD Hamiltonian and FEM Hamiltonian, and calculated the entire system behavior based on analytical mechanics. Fujita [32] introduced the concept of dual resolution elements (DREs), which behave as FEs toward FEM regions but atoms toward MD regions (Figure 1.7). In addition, short wavelength phonons entering the FEs are described based on Langevin dynamics in this scheme. Recently, Murashima et al. [33] coupled FEM with a well-known MD simulator, Large-scale Atomic/Molecular Massively Parallel Simulator [34], which has been used worldwide in MD simulations for many years. It should be noted that these studies are just a part of several studies on MD-FEM concurrent coupling schemes [35–44], indicating that challenges with multi-lengthscale modeling have garnered significant attention and much effort has been devoted to resolving them in recent decades (Figure 1.8).

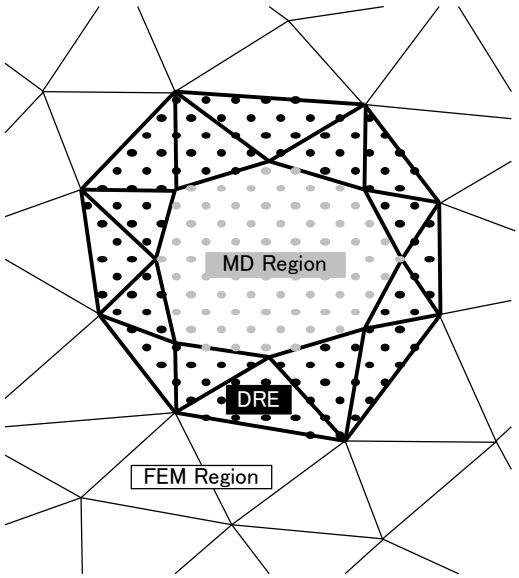

Figure 1.7 Concept of the DRE [32].

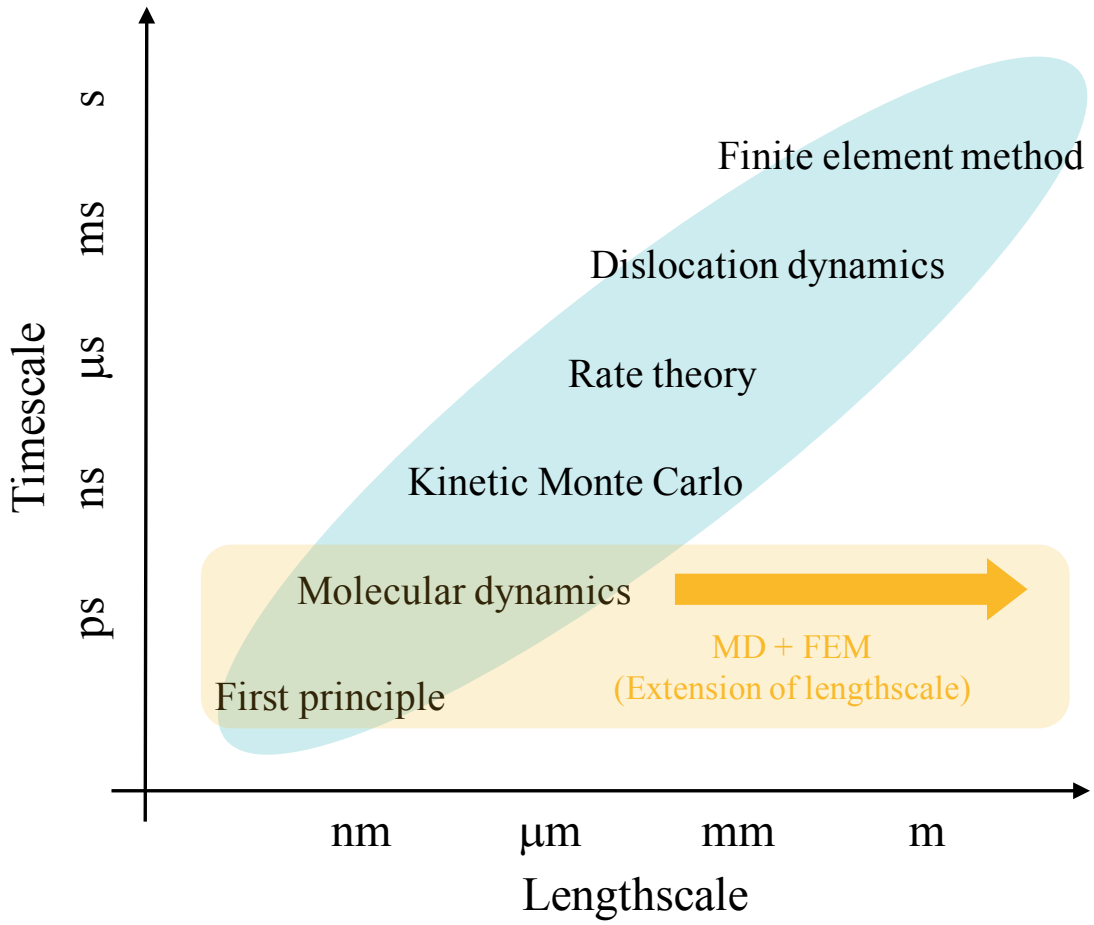

Figure 1.8 Extension of the lengthscale through MD-FEM concurrent coupling.

Regarding the timescale, on the other hand, the modeling approaches that use "state-to-state dynamics" can be effective to extend the timescale from the atomic-vibration level to longer scales. In state-to-state dynamics, each dynamic is modeled as the transition of the system from a certain energy basin to another beyond E_a on the PES (Figure 1.9 and 1.10). This transformation implies that we do not need to track every atomic vibration (~10^{12}–10^{13} Hz), enabling a significant extension of the accessible timescale. Kinetic Monte Carlo (kMC) is a useful tool for atomistic simulations that follows the concept of state-to-state dynamics (Figure 1.11) [45–47]. In kMC, we prepare an event list, where the possible transition patterns and their E_a values are listed. The occurring event at each step is stochastically chosen among the listed events while the probability at which each event is chosen is weighted by its occurring frequency. Note that the occurring frequency of the event i (ν_i) is described by (see

Eq. (1.1)):

$$\nu_i = A_i \exp\left(-\frac{E_a^i}{k_B T}\right) \tag{1.3}$$

where A_i and E_a^i are A and E_a for event i, respectively. Note that, to save on calculation costs, the value of A_i is usually set to be a constant parameter on the order of 10^{12}–10^{13}, reflecting the Debye frequency. In addition, the time increment at each step is performed using:

$$\Delta t = -\frac{\ln \rho}{\sum \nu_i} \tag{1.4}$$

where ρ is a random number on the interval (0, 1). The time increment is dependent on the occurrence frequency, which is a function of E_a. This implies that the drastic increment in the simulated time is achieved if the E_a values of the listed events are relatively high. Hence, we can calculate meso-timescale dynamics, such as diffusion; in some cases, the accessible timescale can be extended even on the order of milliseconds or longer [48].

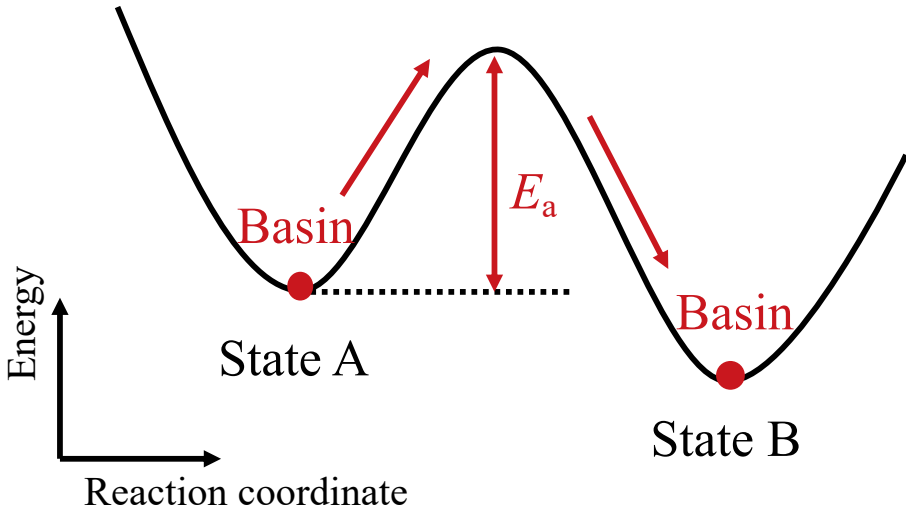

Figure 1.9 Schematic explanation of the concept of state-to-state dynamics.

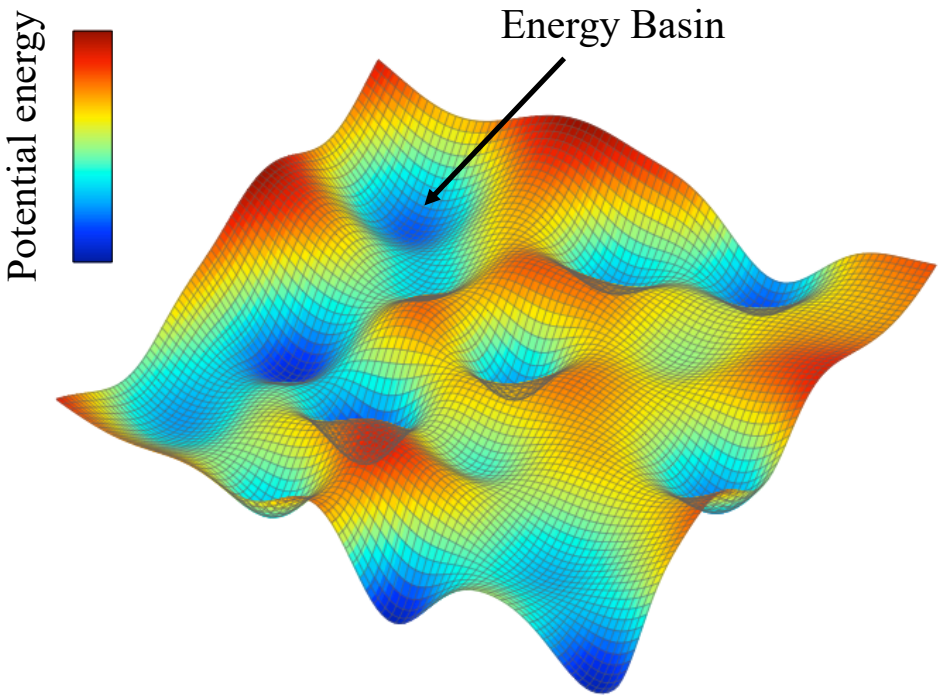

Figure 1.10 Schematic image of two-dimensional PES.

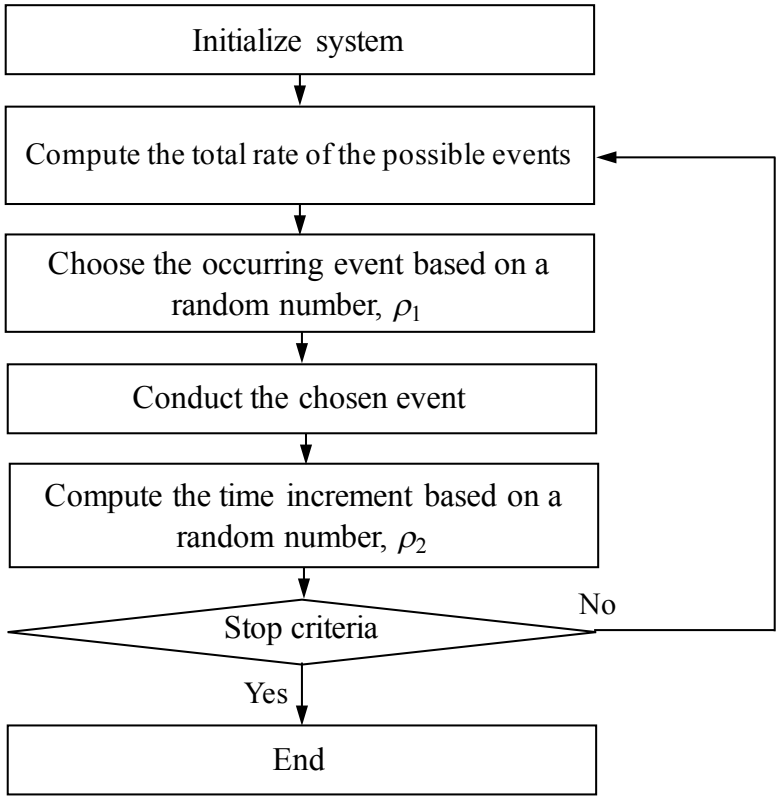

Figure 1.11 Flowchart of the kMC algorithm.

Conventional kMC is classified into two types: objective kMC (OKMC) [49,50] and atomistic kMC (AKMC) [51]. In OKMC, a microstructure of interest is treated as an object and atomic-scale details are not considered; this significantly increases the computation speed. Meanwhile, AKMC considers the complete atomic configuration and in principle is more realistic than OKMC. Because of its power, kMC has been applied to a very wide range of applications not only in materials science but also in many other fields [49–54]. In addition, some previous studies conducted kMC simulations coupled with another atomistic method. Xu et al. [55] performed kMC simulations to investigate the meso-timescale evolution of defects produced through irradiation in iron, using the results of the MD cascade simulations as inputs. Okita et al. [56–58] performed kMC simulations on the three-dimensional behavior of an SIA cluster, where they evaluated E_a values of the listed events by MD simulations, considering the complex strain field around the diffusing atoms. Swinburne et al. [59] also conducted kMC simulations on the three-dimensional behavior of an SIA cluster; here, they constructed a simple model to derive E_a during the kMC simulations through numerous calculations using the nudged elastic band method, which is another atomistic simulation method for extracting the minimum energy path (MEP) of certain dynamics [60]. While maintaining a certain level of atomistic fidelity, these studies have achieved a significant extension of the timescale, up to hundreds of seconds [48].

One feature in conventional kMC, however, poses a severe limitation for simulations: possible events need to be sampled and listed *a priori*. This can lead to flawed system behavior because an intuition-based definition of possible events can often overlook essential dynamics. The diffusion mechanism for adatoms on Al (1 0 0) surfaces is one such example. Until the 1990s, adatoms on the Al (1 0 0) surface were thought to diffuse on the surface through single adatom hops, based on intuition. A density functional theory calculation, however, clarified that a two-atom concerted event is the dominant mechanism for the diffusion, where the adatoms penetrate the surface while pushing one of the surface atoms out onto the surface (Figure 1.12) [61]. This study demonstrates that the dominant adatom diffusion mechanism on the surface is a much more complicated process than previously considered; moreover, it also shows how untrustworthy intuition-based models can be. Owing to this limitation, the development of multi-timescale schemes by coupling MD and the conventional kMC carries the inherent risk of severe lack of atomistic-scale information.

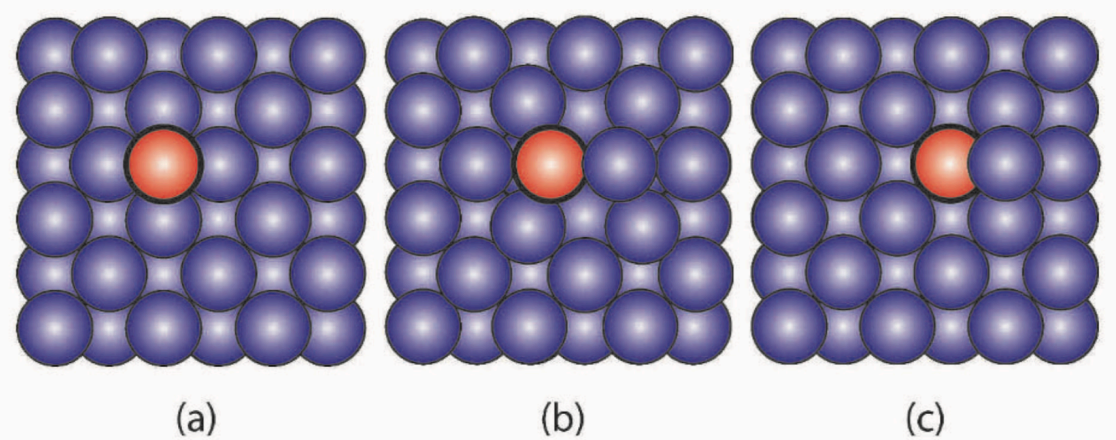

Figure 1.12 Schematic explanation of the dominant mechanism of adatom diffusion on the Al (1 0 0) surface: (a) initial state, (b) transition state, and (c) final state [47].

In contrast to multi-lengthscale schemes, to our knowledge, no strong candidates exist which can handle multi-timescale simulation schemes in the current research environment. Nevertheless, it is very important to develop schemes accessible to timescales of macroscopic degradation phenomena while reflecting sufficient information from the atomistic scale. In other words, there is an insufficiency in the components of current multi-scale modeling frameworks, and breakthroughs are required to resolve this (Figure 1.13). Therefore, the development and improvement of multi-timescale simulation schemes are essential to enhance current modeling technologies.

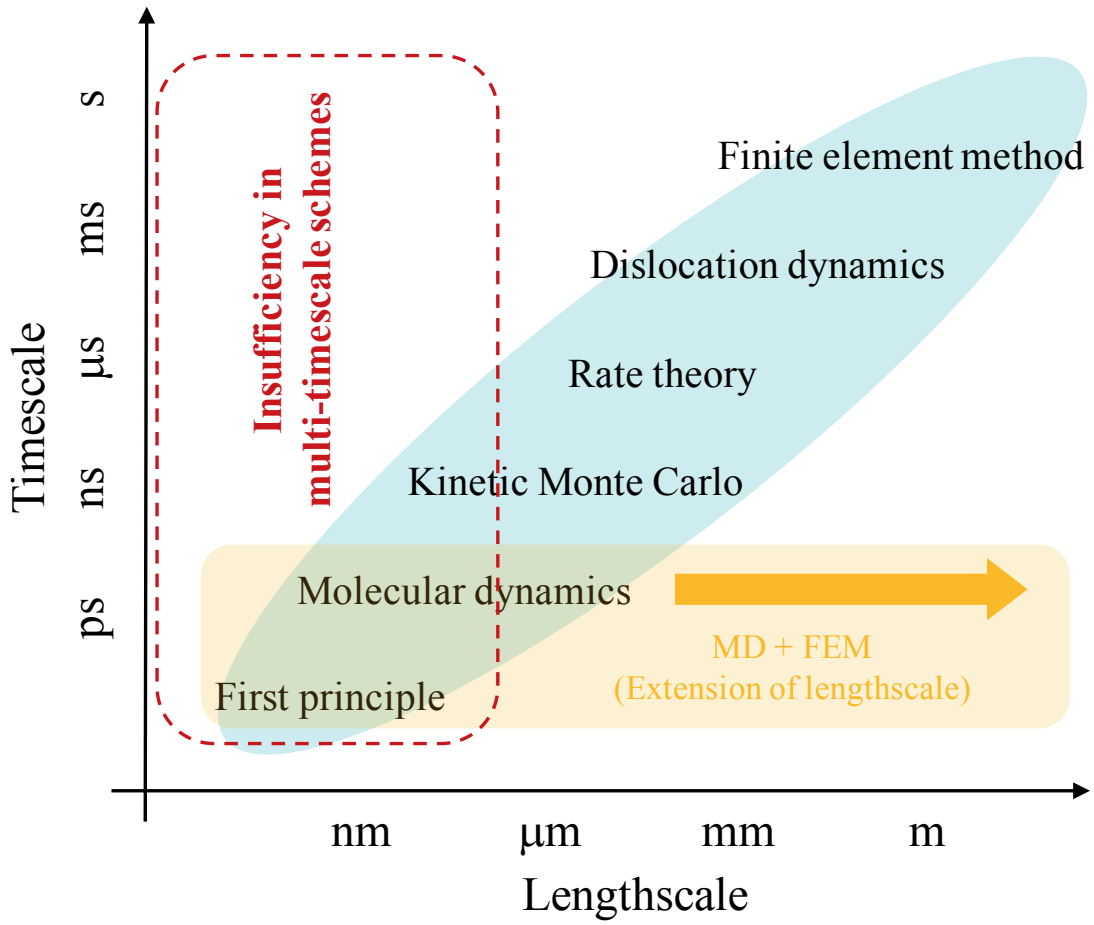

Figure 1.13 Insufficiency in multi-timescale modeling schemes in the current multi-scale modeling framework.

1.2 Goal and contents of this dissertation

As stated above, the macroscopic degradation phenomena we face in real situations occur far beyond atomistic scales, while the behavior of microstructures governs property changes in materials. Hence, the development and improvement of multi-scale modeling frameworks, which bridge the scale gap between each simulation method, are essential for ensuring the integrity of structural materials in modern artifact systems. Regarding multi-lengthscale schemes, several studies are devoted to extending the accessible lengthscale while maintaining atomistic fidelity. Meanwhile, for multi-timescale schemes, there is no strong candidate for extending the accessible timescale with sufficient atomistic details. It is

necessary to compensate for the insufficiency of multi-timescale methods in the multi-scale modeling framework. The goal of this dissertation is to develop and improve multi-timescale simulation schemes that have the capability of both meso-timescale simulation and atomistic fidelity. These will provide breakthroughs to current modeling technologies, improving them to the next level. Thus, this dissertation details the following work (Figure 1.14).

Chapter 2

In Chapter 2, we perform MD simulations on the defect formation processes under irradiation in face-centered cubic (FCC) metals, with a particular focus on the strain effect for the dependence of the defect formation on stacking fault energy (SFE). Note that irradiation-induced defect formation occurs on the order of 10^{-15} s (Figure 1.3) and is a very complex phenomenon where numerous atoms with high kinetic energy collide with each other in a short period. Previous studies have shown that even a difference in the atomic velocity distribution could affect the results [62–64]. Therefore, the MD technique, which can treat atomistic details down to atomic vibrations, is very suitable in this application, while it is difficult to apply event-based simulation methods following state-to-state dynamics, where the direct effects of atomic vibrations on dynamics are ignored. Owing to timescale limitations, it is challenging to sustain simulations after the thermal phase, i.e., the phase where surviving defects diffuse out of the cascade core region, by the MD technique; nevertheless, the results obtained here will be useful input parameters for models based on state-to-state dynamics.

Chapter 3

Recently, on-the-fly kMC techniques have gathered significant attention as kMC methods that maintain atomistic fidelity very close to that of MD. In on-the-fly kMC, at each step, we search for saddle points (SPs) on PES which exists around the energy basin in which the system exists at that moment. The event list for that step is constructed based on the identified SPs. Consequently, we do not need to prepare the event list beforehand, as in conventional kMC, and dynamics beyond our intuition can be simulated. Since the first study using on-the-fly kMC in 2001 (adaptive kMC) [65], several types of on-the-fly kMC techniques have been proposed in recent years, e.g., self-learning kMC in 2005 [66], kinetic activation-relaxation technique in 2008 [67], kMC with the autonomous basin climbing

method in 2010 [68], and self-evolving atomistic kinetic Monte Carlo (SEAKMC) in 2011 [69]. These techniques enabled the simulation of dynamics which were outside the scope of MD and conventional kMC techniques, and provided valuable insights into microstructural evolution [70,71]. We can say that on-the-fly kMC schemes will certainly play an essential role in multi-timescale modeling schemes. In addition, many improved schemes for original on-the-fly kMC techniques have been proposed in the last several years, indicating that on-the-fly kMC schemes are still developing and improving, and more improvements are expected in the future.

One well-known problem of on-the-fly kMC is the high computational cost required for saddle point searches (SPSs); each technique has its own unique algorithm to address it. For instance, adaptive kMC and self-learning kMC recycle the information on SPs found in previous steps to construct the event list in the current step [66,72]; the kinetic activation-relaxation technique also employs a recycling scheme, where the concept of topology is introduced for storing and recycling SP information [67]. These schemes significantly accelerate the simulation; however, when the system visits configurations completely different from previous ones, the recycling scheme is not applicable and a high computational cost is required. Further, the computational cost for SPS increases drastically with an increase in the system size in most cases. This renders the system size to which on-the-fly kMC is applicable relatively small, although many critical microstructural evolution phenomena occur in a system with hundreds of thousands of atoms. Meanwhile, SEAKMC introduces a unique concept of active volume (AV) to solve that problem: AVs are set in regions where dynamics of interest may occur (usually around defects), and atoms outside the AVs are frozen during SPSs. The employment of AV considerably reduces the degrees of freedom of the system, even when the system contains a vast number of atoms. Indeed, a previous study employed SEAKMC for a system with 128,000 atoms [73]. Therefore, SEAKMC is a promising on-the-fly kMC technique, and improvement in SEAKMC will directly lead to an improvement in multi-timescale modeling schemes as a whole.

Therefore, we focus on improving SEAKMC in Chapter 3. Particularly, we propose acceleration schemes for SPS, which is a bottleneck procedure for the whole computational cost in SEAKMC, in order to increase the applicability of SEAKMC. Two acceleration schemes are proposed: (1) a multi-step procedure of SPS, where a relatively small AV is

initially used for obtaining a rough estimate of the SP configuration, followed by searches with sufficiently large AVs to obtain more accurate configurations. Here, the SP information obtained by the SPS with the smaller AV is used as a 'prediction' for the SPS with the larger AV. (2) Recycling of previously identified SP configurations for future searches, which have not been implemented in SEAKMC, although other on-the-fly kMC techniques, such as self-learning kMC and the kinetic activation-relaxation technique, have shown a significant acceleration in calculations owing to this scheme. In addition, we perform accelerated SEAKMC simulations using the results of the MD cascade simulations in Chapter 2 as input data. The meso-timescale behavior of irregularly shaped SIA clusters produced through irradiation is simulated while maintaining atomistic fidelity.

Chapter 4

In kMC event selection, when high-E_a events and low-E_a events are listed together, the low-E_a events are chosen with very high probability. For instance, when an event with E_a = 0.1 eV and E_a = 1.0 eV are listed together, their frequencies are calculated as ~2.1×10^{10} s^{-1} and ~1.6×10^{-5} s^{-1} at 300 K based on Eq. (1.1), respectively. Indeed, for some calculation cases in Chapter 3, most simulation steps involve simulating trivial events with very low E_a, with only slight atomic displacements; no significant change in the cluster shape is observed even after hundreds of steps. Such trivial events are called "flicker events". Since the simulated SIA clusters have energetically unfavorable shapes, these are supposed to eventually transform into stable configurations, namely, Frank loops or perfect loops. This indicates that SEAKMC cannot sufficiently simulate the meso-timescale evolution of these clusters when flicker events dominantly occur in the simulations. We note that the effects of flicker events present a problem not only in on-the-fly kMC but also in general kMC algorithms, implying that in some cases, it might be useful to employ approaches rather than kMC alone while maintaining the meso-timescale simulation capability and atomistic fidelity of on-the-fly kMC.

As stated above, the system dynamics is modeled as the transition between energy basins on the PES via state-to-state dynamics. Thus, the evolution of microstructures toward a stable state, including the transformation of irregularly shaped SIA clusters into stable configurations, corresponds to the system transition to lower-energy states through multiple basin-hops on the PES. Here, the task of exploring the stable state of the microstructures can

be modeled as the energy minimization in a topological space composed of the set of energy basins on the PES.

Based on the above, we develop a method for exploring the stable state of the microstructures based on an optimization algorithm, that is, energy minimization with basins-constructed space (EM/BCS). As the optimization algorithm, we choose temperature parallel simulated annealing (TPSA) [74,75] for two reasons: (1) we need to perform a global optimization and (2) an optimization based on a neighborhood search is suitable to the application here. TPSA has overcome the issues with high computational cost and adjustment of a proper cooling schedule in the simulated annealing method [76], and has been employed in a wide range of applications in both discrete and continuous optimization problems [74,75,77–80]. As in Chapter 3, we apply EM/BCS to the meso-timescale evolution of irregularly shaped SIA clusters produced through irradiation, using the results in Chapter 2 as input data. The transformation processes of these clusters into stable configurations are discussed in detail, with the change in system energy during the processes.

Chapter 5

Chapter 5 provides a summary of this dissertation. We highlight the contribution of our work to the goal of this dissertation. In addition, challenges and future perspectives of our work are discussed.

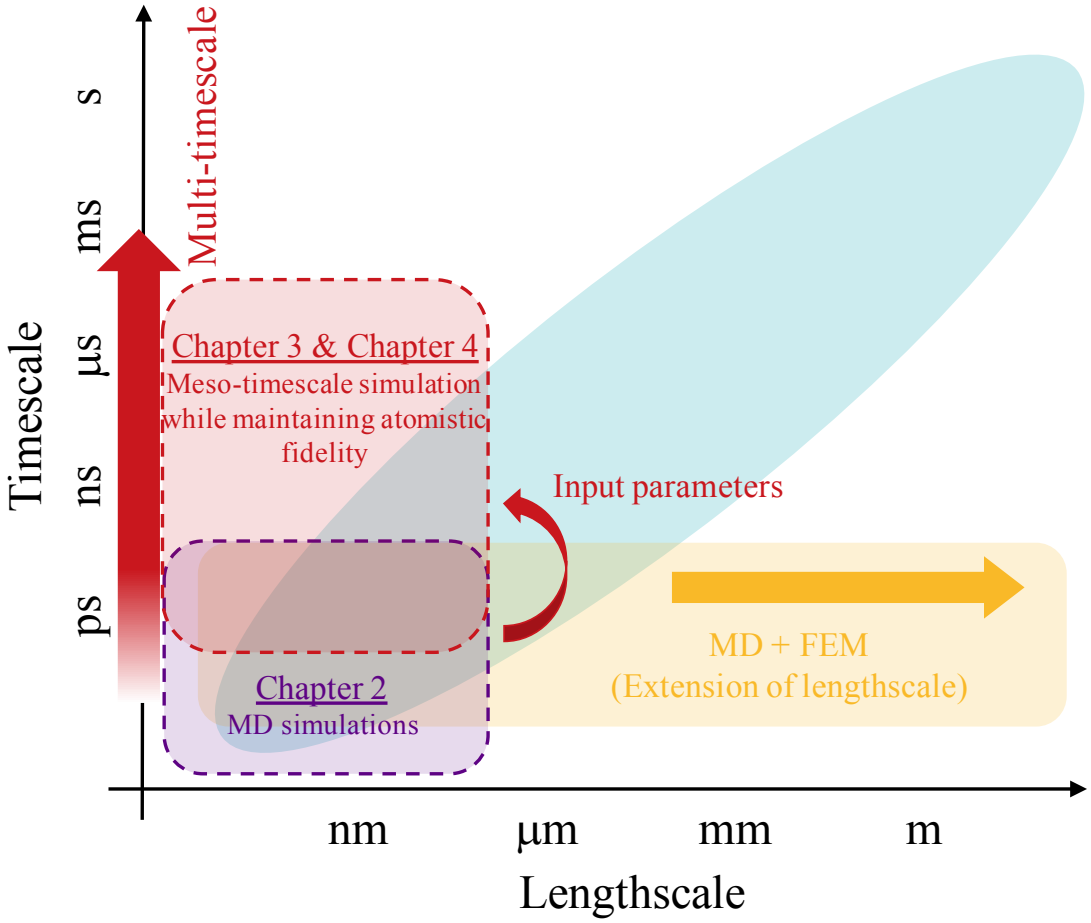

Figure 1.14 overall landscape of this dissertation.

References in Chapter 1

[1] T. Okita, T. Kawabata, H. Murayama, N. Nishino, M. Aichi, "A new concept of digital twin of artifact systems: synthesizing monitoring/inspections, physical/numerical models, and social system models," *Procedia CIRP*, vol. 79, pp. 667–672, 2019.

[2] W. Cai and L. S. Yip, "Molecular Dynamics," in *Comprehensive Nuclear Materials*, Amsterdam, Elsevier, 2012, pp. 249–265.

[3] R. Komanduri and L. M. Raff, "A review on the molecular dynamics simulation of machining at the atomic scale," *Proceedings of the Institution of Mechanical Engineers, Part B: Journal of Engineering Manufacture*, vol. 215, pp. 1639–1672, 2001.

[4] S. A. Hollingsworth and R. O. Dror, "Molecular dynamics simulation for all," *Neuron*, vol. 99, pp. 1129–1143, 2018.

[5] J. L. Gelpi, A. Hospital, R. Goni and M. Orozco, "Molecular dynamics simulations: Advances and applications," *Advances and Applications in Bioinformatics and Chemistry*, vol. 10, pp. 37–47, 2015.

[6] J. Zhang, F. Xu, Y. Hong, Q. Xiong and J. Pan, "A comprehensive review on the molecular dynamics simulation of the novel thermal properties of graphene," *RSC Advances*, vol. 109, pp. 89415–89426, 2015.

[7] X. Liu, D. Shi, S. Zhou, H. Liu, H. Liu and X. Yao, "Molecular dynamics simulations and novel drug discovery," *Expert Opinion on Drug Discovery*, vol. 13, pp. 23–37, 2018.

[8] X. Chen, "Molecular dynamics simulation of nanofluidics," *Reviews in Chemical Engineering*, vol. 34, pp. 5140–5148, 2018.

[9] C. P. Chui, W. Liu, Y. Xu and Y. Zhou, "Molecular dynamics simulation of iron – a review," *SPIN*, vol. 5, pp. 1540007-1–1540007-36, 2015.

[10] R. E. Stoller, "Primary radiation damage formation," in *Comprehensive Nuclear Materials*, Amsterdam, Elsevier, 2012, pp. 293–332.

[11] S. Hayakawa, Y. Hayashi, T. Okita, M. Itakura, K. Suzuki and Y. Kuriyama, "Effects of stacking fault energies on the interaction between an edge dislocation and an 8.0-nm-diameter Frank loop of self-interstitial atoms," *Nuclear Materials and Energy*, vol. 9, pp. 581–586, 2016.

[12] K. Doihara, T. Okita, M. Itakura, M. Aichi and K. Suzuki, "Atomistic simulations to evaluate effects of stacking fault energy on interactions between edge dislocation and

spherical void in face-centered cubic metals," *Philosophical Magazine*, vol. 98, pp. 2061–2076, 2018.

[13] S. Hayakawa, K. Doihara, T. Okita, M. Itakura, M. Aichi and K. Suzuki, "Screw dislocation–spherical void interactions in fcc metals and their dependence on stacking fault energy," *Journal of Materials Science*, accepted.

[14] Y. N. Osetsky and D. J. Bacon, "Void and precipitate strengthening in α-iron: what can we learn from atomic-level modelling?," *Journal of Nuclear Materials*, vol. 323, pp. 268–280, 2003.

[15] Y. N. Osetsky, D. Rodney and D. J. Bacon, "Atomic-scale study of dislocation–stacking fault tetrahedron interactions. Part I: mechanisms," *Philosophical Magazine*, vol. 86, pp. 2295–2313, 2006.

[16] L. Malerba, "Molecular dynamics simulation of displacement cascades in a-Fe: A critical review," *Journal of Nuclear Materials,* vol. 351, pp. 28–38, 2006.

[17] R. E. Voskoboinikov, Y. N. Osetsky and D. J. Bacon, "Computer simulation of primary damage creation in displacement cascades in copper. I. Defect creation and cluster statistics," *Journal of Nuclear Materials,* vol. 377, pp. 385–395, 2008.

[18] K. Nordlund, S. J. Zinkle, A. E. Sand, F. Granberg, R. Averback, R. E. Stoller, T. Suzudo, L. Malerba, F. Banhart, W. J. Weber, F. Willaime, S. L. Dudarev and D. Simeone, "Primary radiation damage: A review of current understanding and models," *Journal of Nuclear Materials,* vol. 512, pp. 450–479, 2018.

[19] A. J. Foreman, W. J. Phythian and C. A. English, "The molecular dynamics simulation of irradiation damage cascades in copper using a many-body potential," *Philosophical Magazine A,* vol. 66, pp. 671–695, 1992.

[20] W. J. Phythian, R. E. Stoller, A. J. Foreman, A. F. Calder and D. J. Bacon, "A comparison of displacement cascades in copper and iron by molecular-dynamics and its application to microstructural evolution," *Journal of Nuclear Materials,* vol. 223, pp. 245–261, 1995.

[21] Y. N. Osetsky, D. J. Bacon, B. N. Singh and B. D. Wirth, "Atomistic study of the generation, interaction, accumulation and annihilation of cascade-induced defect clusters," *Journal of Nuclear Materials,* vol. 307–311, pp. 852–861, 2002.

[22] J. Behler and M. Parrinello, "Generalized neural-network representation of high-

dimensional potential-energy surfaces," Physical Review Letters, vol. 98, pp. 146401-1–146401-4, 2007.

[23] TOP500. [Online]. Available: http://www.top500.org.

[24] G. Moore, "Cramming more components onto integrated circuits," Electronics, vol. 38, pp. 114–117, 1965.

[25] A. F. Voter, F. Montalenti and T. C. Germann, "Extending the time scale in atomistic simulation of materials," *Annual Review of Materials Research*, vol. 32, pp. 321–346, 2002.

[26] A. Laio and F. L. Gervasio, "Metadynamics: a method to simulate rare events and reconstruct the free energy in biophysics, chemistry and material science," Reports on Progress in Physics, vol. 71, pp. 126601-1–126601-22, 2008.

[27] A. F. Voter, "Hyperdynamics: accelerated molecular dynamics of infrequent events," *Physical Review Letters*, vol. 78, pp. 3908–3911, 1997.

[28] M. R. Sorensen and A. F. Voter, "Temperature-accelerated dynamics for simulation of infrequent events," *Journal of Chemical Physics*, vol. 112, pp. 9599–9606, 2000.

[29] A. F. Voter, "Parallel replica method for dynamics of infrequent events," *Physical Review B*, vol. 57, pp. R13985–R13988, 1998.

[30] S. Kohlhoff, P. Gumbsch and H. F. Fischmeister, "Crack propagation in b.c.c. crystals studied with a combined finite-element and atomistic model," *Philosophical Magazine A*, vol. 64, pp. 851–878, 1991.

[31] J. Q. Broughton, F. F. Abraham, N. Bernstein and E. Kaxiras, "Concurrent coupling of length scales: Methodology and application," *Physical Review B*, vol. 60, pp. 2391–2403, 1999.

[32] S. Fujita, "Effects of nanoscale deformation mechanism on structural reliability," Ph.D. thesis, Department of Quantum Engineering and Systems Science, School of Engineering, University of Tokyo, 2010.

[33] T. Murashima, S. Uratam and S. Li, "Coupling finite element method with Large Scale Atomic/Molecular Massively Parallel Simulator (LAMMPS) for hierarchical multiscale simulations," submitted.

[34] S. Plimpton, "Fast parallel algorithms for short-range molecular dynamics," *Journal of Computational Physics,* vol. 117, pp. 1–19, 1995.

[35] F. F. Abraham, J. Q. Broughton, N. Bernstein and E. Kaxiras, “Spanning the continuum to quantum length scales in a dynamic simulation of brittle fracture,” *Europhysics Letters*, vol. 44, pp. 783–787, 1998.

[36] S. Ogata, E. Lidorikis, F. Shimojo, A. Nakano, P. Vashishta and R. K. Kalia, “Hybrid finite-element/molecular-dynamics/electronic-density-functional approach to materials simulations on parallel computers,” *Computer Physics Communications*, vol. 138, pp. 143–154, 2001.

[37] E. Lidorikis, M. E. Bachlechner, R. K. Kalia, A. Nakano and P. Vashishta, “Coupling atomistic and continuum length scales in heteroepitaxial systems: Multiscale molecular-dynamics/finite-element simulations of strain relaxation in Si / Si_3N_4 nanopixels,” *Physical Review B*, vol. 72, pp. 115338-1–115338-16, 2005.

[38] H. Cheng, L. Wang, M. Du, C. Cao, Y. Wan, Y. He, K. Muralidharan, G. Greenlee and A. Kolchin, “Quantum, classical, and multi-scale simulation of silica–water interaction: molecules, clusters, and extended systems,” *Journal of Computer-Aided Materials Design*, vol. 13, pp. 161–183, 2006.

[39] R. E. Rudd and J. Q. Broughton, “Coarse-grained molecular dynamics and the atomic limit of finite elements,” *Physical Review B*, vol. 58, pp. R5893–R5896, 1998.

[40] R. E. Rudd and J. Q. Broughton, “Coarse-grained molecular dynamics: Nonlinear finite elements and finite temperature,” *Physical Review B*, vol. 72, pp. 144104-1–144104-32, 2005.

[41] J. A. Smirnova, L. V. Zhigilei and B. J. Garrison, “A combined molecular dynamics and finite element method technique applied to laser induced pressure wave propagation,” *Computer Physics Communications*, vol. 118, pp. 11–16, 1999.

[42] G. J. Wagner and W. K. Liu, “Coupling of atomistic and continuum simulations using a bridging scale decomposition,” vol. 190, pp. 249–274, 2003.

[43] W. K. Liu, E. G. Karpov, S. Zhang, H. S. Park, “An introduction to computational nanomechanicsand materials,” *Computer Methods in Applied Mechanics and Engineering*, vol. 193, pp. 1529–1578, 2004.

[44] B. Q. Luan, S. Hyun, J. F. Molinari, N. Bernstein and M. O. Robbins, “Multiscale modeling of two-dimensional contacts,” *Physical Review E*, vol. 74, pp. 046710-1–046710-11, 2006.

[45] A. B. Bortz, M. H. Kalos and J. L. Lebowitz, "A new algorithm for Monte Carlo simulation of ising spin systems," *Journal of Computational Physics,* vol. 17, pp. 10–18, 1975.

[46] D. T. Gillespie, "Monte Carlo simulation of random walks with residence time dependent transition probability rates," vol. 28, pp. 395–407, 1978.

[47] A. F. Voter, "Introduction to the kinetic Monte Carlo method," in *Radiation Effects in Solids*, Dordrecht, Springer, 2007, pp. 1–23.

[48] T. Okita, S. Hayakawa, M. Itakura, M. Aichi, S. Fujita and K. Suzuki, "Conservative climb motion of a cluster of self-interstitial atoms toward an edge dislocation in BCC-Fe," *Acta Materialia,* vol. 118, pp. 342–349, 2016.

[49] C. S. Becquart, A. Barbu, J. L. Bocquet, M. J. Caturla, C. Domain, C. -C. Fu, S. I. Golubov, M. Hou, L. Malerba, C. J. Ortiz, A. Souidi and R. E. Stoller, "Modeling the long-term evolution of the primary damage in ferritic alloys using coarse-grained methods," *Journal of Nuclear Materials,* vol. 406, pp. 39–54, 2010.

[50] M. J. Caturla, “Objective kinetic Monte Carlo methods applied to modeling radiation effects in materials,” *Computational Materials Science*, vol. 156, pp. 452–459, 2019.

[51] F. Soisson, C. S. Becquart, N. Castin, C. Domain, L. Malerba and E. Vincent, "Atomistic Kinetic Monte Carlo studies of microchemical evolutions driven by diffusion processes under irradiation," *Journal of Nuclear Materials,* vol. 406, pp. 55–67, 2010.

[52] C. C. Battaile, "The Kinetic Monte Carlo method: Foundation, implementation and application," *Computer Methods in Applied Mechanics and Engineering,* vol. 197, pp. 3386–3398, 2008.

[53] M. Kotrla, "Numerical simulations in the theory of crystal growth," *Computer Physics Communications,* vol. 97, pp. 82–100, 1996.

[54] G. H. Gilmer, H. Huang and C. Roland, "The film deposition: fundamentals and modeling," *Computational Materials Science,* vol. 12, pp. 354–380, 1998.

[55] H. Xu, Y. N. Osetsky and R. E. Stoller, “Cascade annealing simulations of bcc iron using objective kinetic Monte Carlo,” *Journal of Nuclear Materials*, vol. 423, pp. 102–109, 2012.

[56] T. Okita, S. Hayakawa, M. Itakura, M. Aichi, S. Fujita and K. Suzuki, "Conservative climb motion of a cluster of self-interstitial atoms toward an edge dislocation in BCC-

Fe," *Acta Materialia,* vol. 118, pp. 342–349, 2016.

[57] S. Hayakawa, T. Okita, M. Itakura, M. Aichi, S. Fujita and K. Suzuki, "Behavior of a self-interstitial-atom type dislocation loop in the periphery of an edge dislocation in BCC-Fe," *Nuclear Materials and Energy,* vol. 9, pp. 592–597, 2016.

[58] S. Hayakawa, T. Okita, M. Itakura, M. Aichi and K. Suzuki, "Interactions between clusters of self-interstitial atoms via a conservative climb in BCC-Fe," *Philosophical Magazine,* vol. 98, pp. 2311–2325, 2018.

[59] T. D. Swinburne, K. Arakawa, H. Mori, H. Yasuda, M. Isshiki, K. Miura, M. Uchikoshi, S. L. Dudarev, “Fast, vacancy-free climb of prismatic dislocation loops in bcc metals,” *Scientific Reports*, vol. 6, pp. 30596-1–30596-8, 2016.¥

[60] H. Jonsson, G. Mills and K. W. Jacobsen, “Nudged Elastic Band Method for Finding Minimum Energy Paths of Transitions,” in *Classical and Quantum Dynamics in Condensed Phase Simulations*, Villa Marigola, World Scientific, 1998, pp. 385–404.

[61] P. J. Feibelman, "Diffusion path for an Al adatom on Al (001)," *Physical Review Letters,* vol. 65, pp. 729–732, 1990.

[62] T. Okita, Y. Yang, J. Hirabayashi, M. Itakura and K. Suzuki, “Effects of stacking fault energy on defect formation process in face-centered cubic metals,” *Philosophical Magazine*, vol. 96, pp. 1579–1597, 2016.

[63] Y. Yang, T. Okita, M. Itakura, T. Kawabata and K. Suzuki, “Influence of stacking fault energies on the size distribution and character of defect clusters formed by collision cascades in face-centered cubic metals,” *Nuclear Materials and Energy*, vol. 9, pp. 587–591, 2016.

[64] D. Nakanishi, T. Kawabata, K. Doihara, T. Okita, M. Itakura and K. Suzuki, “Effects of stacking fault energies on formation of irradiation-induced defects at various temperatures in face-centred cubic metals,” *Philosophical Magazine*, vol. 98, pp. 3034–3047, 2018.

[65] G. Henkelman and H. Jonsson, “Long time scale kinetic Monte Carlo simulations without lattice approximation and predefined event table,” *Journal of Chemical Physics*, vol. 115, pp. 9657–9666, 2001.

[66] O. Trushin, A. Karim, A. Kara and T. S. Rahman, “Self-learning kinetic Monte Carlo,” *Physical Review B*, vol. 72, pp. 115401-1–115401-9, 2005.

[67] F. El-Mellouhi, N. Mousseau and L. J. Lewis, “Kinetic activationrelaxation technique: An off-lattice self-learning kinetic Monte Carlo algorithm,” *Physical Review B*, vol. 78, pp. 153202-1–153202-4, 2008.

[68] Y. Fan, A. Kushima and B. Yildiz, “Unfaulting mechanism of trapped self-interstitial atom clusters in bcc Fe: A kinetic study based on the potential energy landscape,” *Physical Review B*, vol. 81, pp. 104102-1–104102-7, 2010.

[69] H. Xu, Y. N. Osetsky and R. E. Stoller, “Simulating complex atomistic processes: On-the-fly kinetic Monte Carlo scheme with selective active volumes,” *Physical Review B*, vol. 84, pp. 132103-1–132103-4, 2011.

[70] Y. Fan, S. Yip and B. Yildiz, “Autonomous basin climbing method with sampling of multiple transition pathways: application to anisotropic diffusion of point defects in hcp Zr,” *Journal of Physics: Condensed Matter*, vol. 26, pp. 365402-1–365402-16, 2014.

[71] H. Xu, R. E. Stoller, Y. N. Osetsky and D. Terentyev, “Solving the puzzle of <1 0 0 > interstitial loop formation in bcc iron,” *Physical Review Letters*, vol. 110, pp. 265503-1–265503-5, 2013.

[72] L. Xu and G. Henkelman, “Adaptive kinetic Monte Carlo for first-principles accelerated dynamics,” *The Journal of Chemical Physics*, vol. 129, pp. 114104-1–114104-9, 2008.

[73] H. Xu, R. E. Stoller and Y. N. Osetsky, “Cascade defect evolution processes: Comparison of atomistic methods,” *Journal of Nuclear Materials*, vol. 443, pp. 66–70, 2013.

[74] K. Kimura and K. Taki, "Time-homogeneous parallel annealing algorithm," in *The 13th IMACS World Congress of Computation and Applied Mathematics*, Dublin, 1991.

[75] K. Konishi, K. Taki and K. Kimura, "Temperature parallel simulated annealing algorithm and its evaluation," *Transaction on Information Processing Society of Japan,* vol. 36, pp. 797–807, 1995.

[76] S. Kirkpatrick, C. D. Gelett Jr. and M. P. Vecchi, "Optimization by simulated annealing," *Science,* vol. 220, pp. 671–680, 1983.

[77] M. Miki, T. Hiroyasu and M. Kasai, "Application of the temperature parallel simulated annealing to continuous optimization problems," *JSPP,* vol. 41, pp. 1607–1616, 1999.

[78] W. Cai, D. J. Ewing and L. Ma, "Investigation of temperature parallel simulated annealing for optimizing continuous functions with application to hyperspectral

tomography," *Applied Mathematics and Computation,* vol. 217, pp. 5754–5767, 2011.

[79] M. Miki, T. Hiroyasu, M. Kasai, K. Ono and T. Jitta, "Temperature parallel simulated annealing with adaptive neighborhood for continuous optimization problem," *Computational Intelligence and Applications,* pp. 149–154, 2002.

[80] K. Konishi, M. Yashki and K. Taki, "An Application of Temperature Parallel Simulated Annealing to the Traveling Salesman Problem and its Efficient Implementation on the Distributed Memory Parallel Machine," *1996 Joint Symposium of Parallel Processing.*

Chapter 2 MD simulations of defect formation process in FCC metals under irradiation

2.1 Background

A characteristic feature of the structural materials of nuclear power plants is their use under neutron irradiation. Fast neutrons typically have kinetic energy (E_n) of the order of 1 MeV, and once the neutron invades materials and collides with the atoms of the materials, some amount of its kinetic energy is transferred to those atoms. The maximum energy transfer (E_m) in the case of an elastic collision between a neutron in motion with E_n and an atom at rest is described as

$$E_m = \frac{4M_1M_2}{(M_1 + M_2)^2} E_n \tag{2.1}$$

where M_1 and M_2 express the masses of the neutron and the atom, respectively. For instance, in body-centered cubic (BCC) iron, the collided atom obtains the average kinetic energy (E_{ave}) of ~35 keV when the neutron has E_n of 1 MeV and $E_{ave} = E_m/2$, following Eq. (2.1). Since the minimum kinetic energy necessary for an atom to displace from its lattice site (called the displacement threshold energy, E_d) is typically 20 to 40 eV for most metals and alloys used in structural materials [1], the collided atom can be displaced from its original site relatively easily, and can either locate between other atoms or strike another atom. In the latter case, another collision event is induced, and not surprisingly, if the kinetic energy transferred to the collided atom in the second collision is larger than E_d, a displacement of that atom occurs. Such an iterative series of collisions and displacements of atoms is called a "collision cascade" or a "displacement cascade." The atom initially struck by the neutron is called the primary knock-on atom (PKA), and it is known that the average kinetic energy transferred to the PKA (E_{PKA}) can vary as much as several tens of keV in light water reactors. Furthermore, E_{PKA} can increase to even several hundreds of keV in fusion reactors, where the structural materials can be exposed to ~14 MeV of neutron irradiation [2].

Atoms that recoil from their original site and locate between other atoms are called "SIAs",

while lattice sites that do not contain an atom are called "vacancies." In addition, these defects often form a cluster since it is usually a more energetically favorable state than existing individually. A stable configuration of defect clusters depends on various factors, including the material structure, cluster size, and the strain field that exists around the cluster. In FCC metals, four main types of stable configurations are observed: two types of planar dislocation loops for both SIA and vacancy clusters; namely, Frank (faulted) and perfect loops, and two types of three-dimensional configurations that form only with vacancy clusters; namely, stacking fault tetrahedra (SFTs) and voids [3]. Figure 2.1 shows the configuration of these clusters reproduced by atomistic simulations. Note that the configurations are visualized by the common neighbor analysis (CNA) algorithm [4,5], where the local structural environment is investigated, namely, FCC, BCC, hexagonal close-packed (HCP) or neither of them. In the figure, blue denotes atoms that have an HCP structure, i.e., a stacking fault structure, here; yellow denotes atoms that have neither an FCC, BCC, nor HCP structure. Atoms that have an FCC structure, namely, a structure of a perfect lattice here, are eliminated for visualizing defects.

(1) Frank loop (faulted loop)

A Frank loop contains a stacking fault area on its habit plane and is known as a sessile cluster. It forms on a close-packed plane, namely a $\{1\ 1\ 1\}$ habit plane with a Burgers vector of $\boldsymbol{b} = a_0/3\langle 1\ 1\ 1\rangle$, where a_0 is the lattice constant.

(2) Perfect loop

Atomistic simulations have confirmed that perfect loops glide one-dimensionally with very low activation energy along its Burgers vector direction; namely, the close packed direction of $\langle 1\ 1\ 0\rangle$ [6]. Note that, as seen in Figure 2.1, the loop edges that exist on a $\{1\ 1\ 1\}$ plane dissociate into Shockley partial dislocations, bounding stacking fault areas.

(3) Stacking fault tetrahedron

The formation of SFTs is confirmed only in FCC metals after irradiation, quenching from high temperature, and deformation [7–11]. Silcox and Hirsch proposed the formation mechanism of an SFT, where a vacancy platelet on a [1 1 1] plane collapses, which induces the dissociation of its edges to form stair-rod partial and Shockley partial dislocations, followed by the glide of the Shockley partial dislocations toward the apex of the tetrahedron, leading to the formation of SFT (the Silcox–Hirsch mechanism) [7]. This mechanism is verified by in situ observations of vacancy loops in quenched gold using transmission electron

microscopy (TEM) [12]. In addition, the direct formation of SFTs in the vacancy-rich cascade core during the "thermal spike phase" is confirmed by MD simulations and TEM observations [13–18].

(4) Void

The configuration of voids is roughly spherical, and mainly composed of facets that correspond to close-packed planes of the host lattice. The term "bubble" can be used to specify a void that contains gaseous species, such as helium.

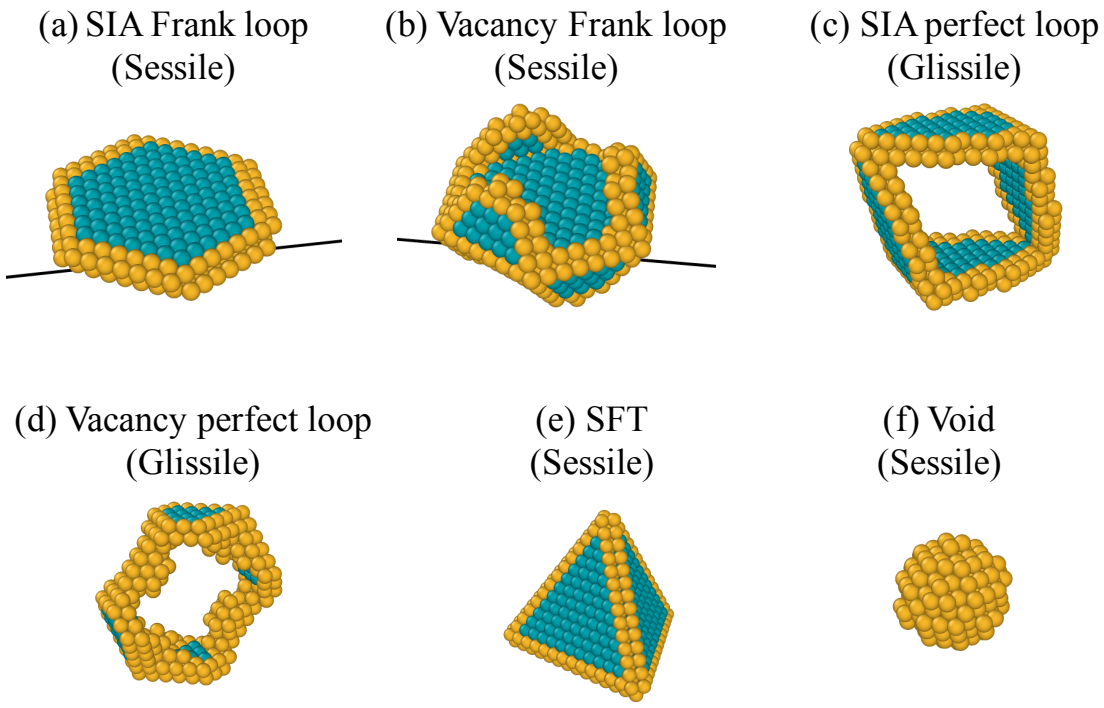

Figure 2.1 Stable configurations of defect clusters in FCC metals, visualized by CNA algorithm [4,5].

It is known that the behavior of these defect clusters considerably enhances microstructural evolution, which leads to substantial changes in material properties such as dimensional stabilities and mechanical properties. For instance, the supersaturation of vacancy defects, caused by the preferential absorption of SIA clusters by dislocations in a material, induces a macroscopic increase in the material's volume (void swelling, Figure 2.2) [19–25]; irradiation-induced defects can impede the movement of the dislocation, resulting in an increase in the material's yield stress (irradiation hardening, Figure 2.3) [27–31]. Further,

each defect and its cluster have their own geometry and mobility (Figure 2.4), and hence they uniquely contribute to the microstructural evolution. Therefore, understanding the defect formation process (i.e., quantifying the number of defects, their clusters produced through displacement cascades and the formation ratio of each type of defect under various conditions) is essential for evaluating the irradiation-induced degradation of the mechanical properties of structural materials.

The MD technique plays an important role in performing such a challenging task because defect formations occur over very short times and length scales—on the order of picoseconds and nanometers, respectively—that limit investigation by experimental and analytical approaches. Many MD simulations focusing on displacement cascades have been performed to date, which have varied conditions such as the materials, temperature, and E_{PKA} [32–37] (Figure 2.5). These simulations have clarified the atomic-level picture of the defect formation process under irradiation, and they have significantly contributed to a comprehensive understanding of microstructural evolution. Further, they provide useful input parameters for coarser-grained models of irradiation-induced mechanical property changes.

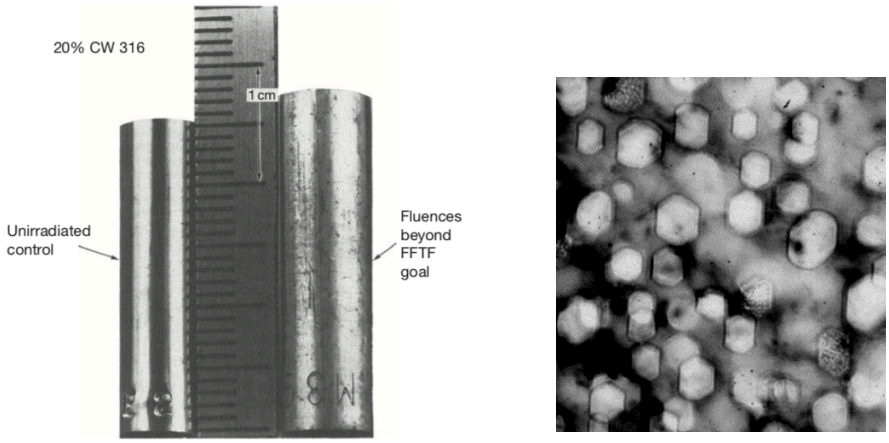

Figure 2.2 (a) Macroscopic increase in material's volume (unfueled 20 % cold-worked AISI 316 open cladding tube at ~75 dpa at 783 K) [19], and (b) supersaturation of vacancy defects (Fe–15Cr–16Ni, FFTF, 43.8 dpa at 700 K) [20].

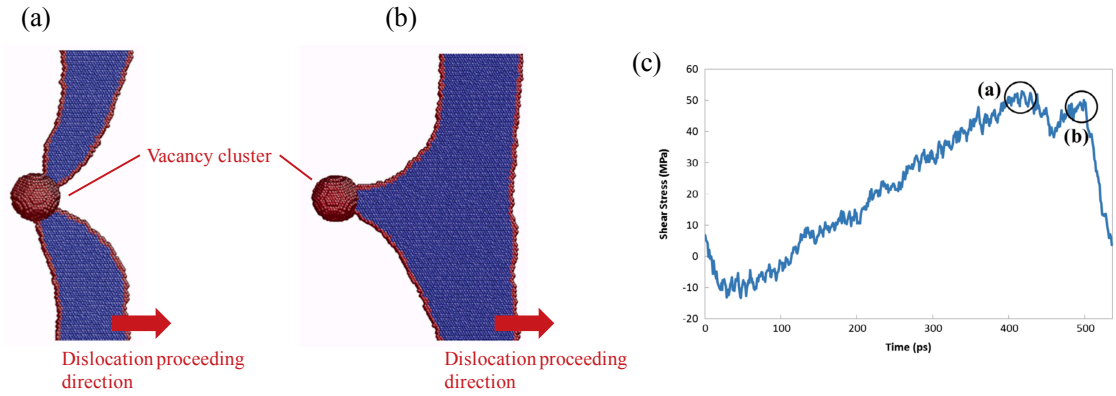

Figure 2.3 (a) and (b) Interaction between an edge dislocation and vacancy cluster in MD simulations, and (c) history of the applied shear stress during the interaction (reproduced from Figure 1.4) [26].

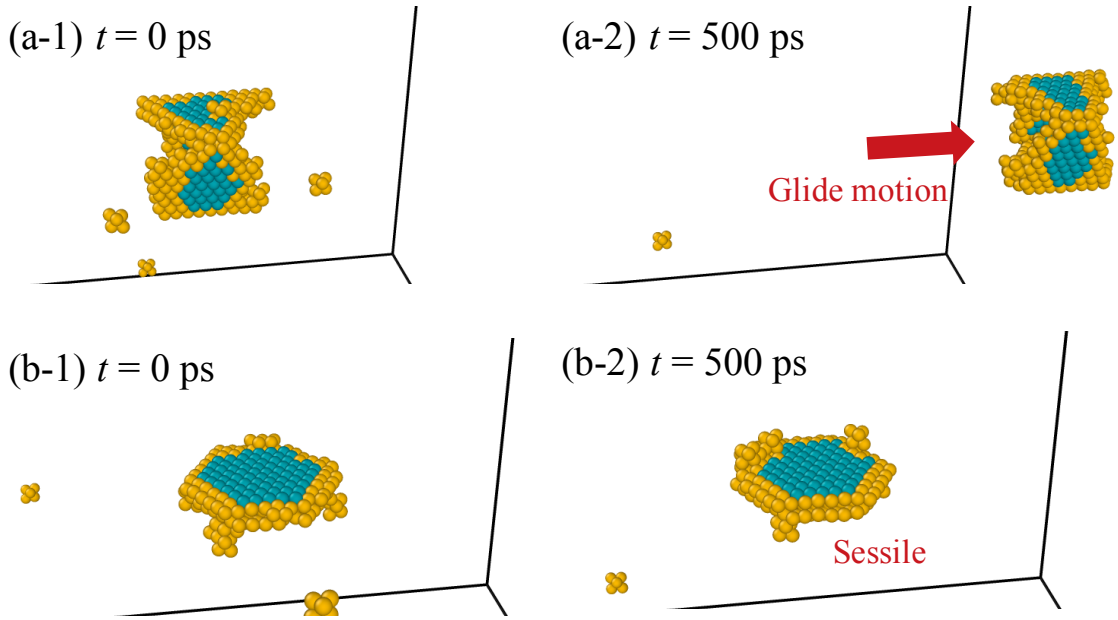

Figure 2.4 Examples of unique behaviors of each type of defect clusters: (a-1) and (a-2) behavior of an SIA perfect loop, which is glissile; (b-1) and (b-2) behavior of an SIA Frank loop, which is sessile.

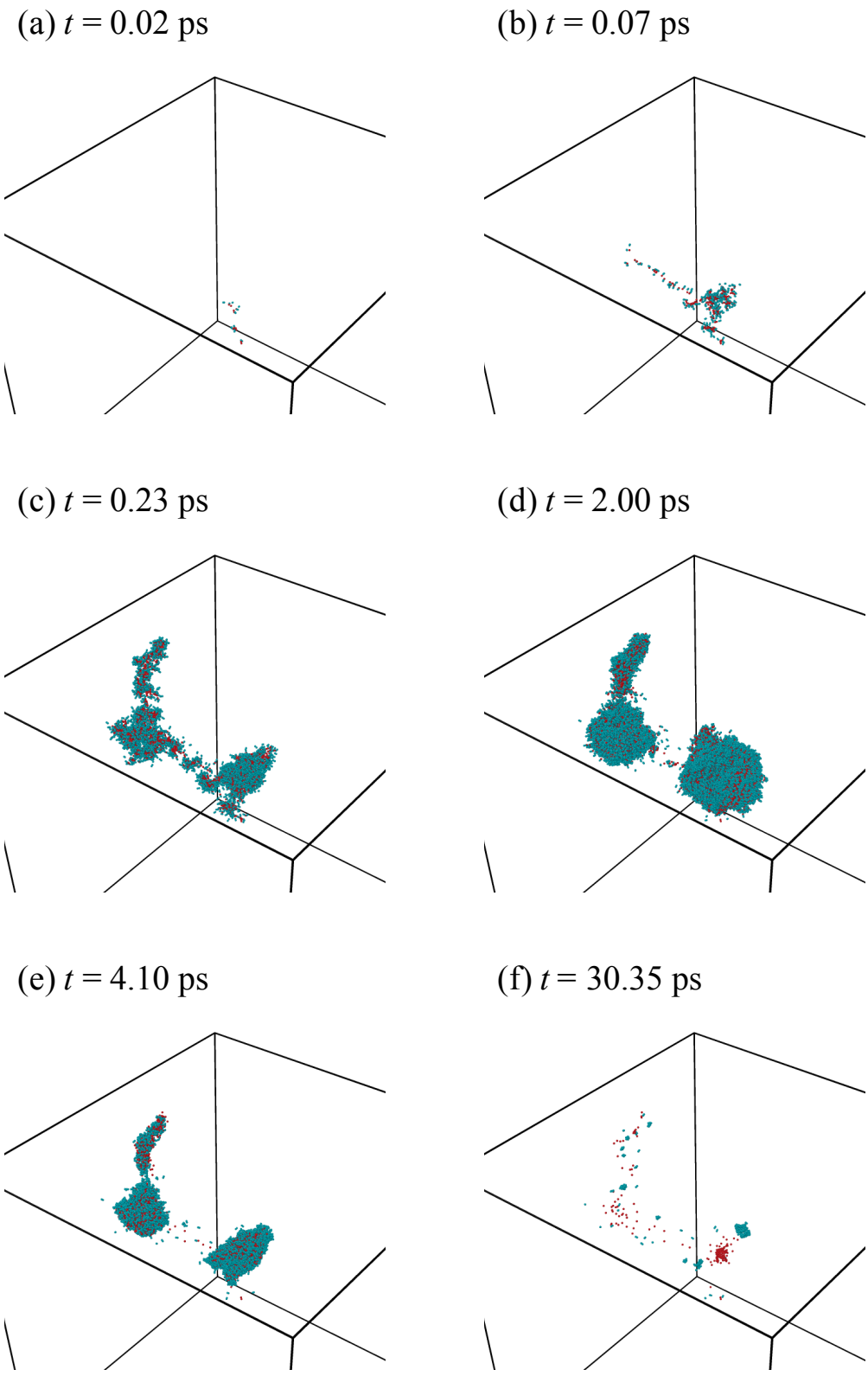

Figure 2.5 Examples of cascade displacements simulations at E_{PKA} = 50 keV and T = 300 K in copper using MD. Blue indicates SIAs; red indicates vacancies.

One important factor that should be considered when modeling irradiation-induced defect formations is the presence of internal and external strains on the materials. Based on this, several MD studies have focused on the effects of strain on the defect formation. Gao et al. [38] investigated the effects of uniform tensile strain on the formation of SIAs and their clusters in BCC iron under irradiation, followed by the study of Beeler et al. [39], which focused on the effects of various types of strain and PKA directions on cascade events in BCC iron. Wang et al. [40] studied the effects of strain on displacement cascades in tungsten and discussed the relationship between the strain direction and the PKA direction in detail. For HCP metals, Di et al. [41,42] evaluated the effects of strain on displacement cascades in zirconium with a uniaxial strain along either the $\langle a \rangle$ or $\langle c \rangle$ axis. In addition, Sahi et al. [43] investigated the effects of various strain types and temperatures on the defect formation process in zirconium under irradiation. Regarding FCC metals, Miyashiro et al. [44] studied the strain effects on the number of defects produced and the size distribution of defects in copper under irradiation. They employed a $[1\ 1\ 1]$ uniaxial strain, a hydrostatic strain, and an isometric strain, and the results indicated that the deformation anisotropy has a significant impact on the defect formation process. Later, they extended the study by investigating the influence of E_{PKA} on the defect formation under a $[1\ 1\ 1]$ uniaxial strain [45]. These studies have shown that the defect formation process through displacement cascades is considerably influenced by the presence of a strain field in the material, demonstrating the importance of considering the strain effect when modeling irradiation-induced defect formations.

On the other hand, SFE is a critical material property that controls microstructural behavior in FCC metals. SFE is defined as the energy necessary to form a unit area of stacking fault. As discussed in the second paragraph in this section, defect clusters in FCC metals, except for voids, contain stacking fault areas, which give rise to a strong dependence on SFE for their formation energy. Thus, the defect formation process is influenced by the SFE. Some studies have focused on this point, where the effects of SFE on the defect formation process under irradiation in FCC metals was evaluated by MD simulations [46–48]. The results show that the number of perfect SIA loops is larger at lower SFE, leading to an increased formation of glissile SIA clusters at lower SFE. According to classical dislocation theory, the formation energy of SIA perfect loops is assumed to be independent of SFE, and the ratio of glissile SIA clusters decreases with a decrease in SFE because of the lower formation energy of Frank

loops at lower SFE [49]. In this theory, however, the edge dissociation of SIA perfect loops is not taken into consideration although atomistic simulations clearly exhibit the presence of stacking fault areas at the cluster edges, as shown in Figure 2.1, which leads to the opposite trend of the glissile clusters ratio dependence on SFE than that observed in atomistic simulations. Such insights regarding the mobility of defect clusters are quite important because the subsequent microstructural evolution is significantly affected by the behavior of the clusters [50–53], particularly in metals that have low SFE, such as austenitic stainless steels (~16–34 mJ m^{-2}, depending on the temperature [54]). However, these studies did not consider the effect of strain field on the defect formation process, although previous studies have shown that there is a significant impact of strain on defect formation in FCC metals [44,45]. Therefore, it is necessary to verify that the SFE dependence of the defect formation observed in previous studies [46–48] is valid in the presence of a strain field.

In this section, we study the effects of strain fields on the SFE dependence of the number of defects produced, size distributions of defect clusters, configurations of SIA clusters, and ratio of glissile SIA clusters under irradiation. MD simulations of displacement cascades are performed to elucidate these dependencies while applying Poisson's deformation to the simulation cell and using interatomic potentials that differ only in SFE. In addition, the defect formation energies were calculated by molecular statics (MS) and MD simulations; the results are discussed together with those of the cascade simulations.

2.2 Simulation methods

2.2.1 Cascade simulations

The displacement cascade simulations were performed with the Large-scale Atomic/Molecular Massively Parallel Simulator (LAMMPS) [55]. For elucidating the unique contribution of the SFE effect on the defect formation process, six sets of embedded atom method (EAM)-type interatomic potentials, developed by Borovikov et al., were used for calculating interatomic forces during the simulations [56]. Note that these potentials were developed based on the potential for pure Cu [57], and the value of SFE in the potentials was changed while other material properties were kept almost constant (Table 2.1). The Ziegler-Biersack-Littmark universal potential was used to describe the interatomic forces at short

distances [58], which was smoothly joined to the EAM-type potential using fifth-order spline functions [46]. The simulation cell was oriented along the $[\bar{1}\,\bar{1}\,2]$, $[1\,\bar{1}\,0]$, and $[1\,1\,1]$ directions, and the cell dimensions along each direction were ~50 nm. The cell contained ~10,000,000 atoms in total, and periodic boundary conditions were applied along all directions. The lattice constant was scaled in accordance with the thermal expansion to render the stress in the cell as negligible. Previous studies have shown that the deformation anisotropy considerably affects the number of displaced atoms [44] and that the number of SIA perfect loops controls the obtained ratio of glissile SIA clusters [46–48]. Based on these, a tensile strain with a magnitude of 0.5 % was applied along the $[1\,\bar{1}\,0]$ direction, and a compressive strain was applied along the $[\bar{1}\,\bar{1}\,2]$ and $[1\,1\,1]$ directions, following the Poisson's ratio. The value of Poisson's ratio for each potential was obtained with other atomistic simulations and the elasticity. The procedure has been explained in detail elsewhere [59]. The strained cell was equilibrated for ~10 ps at 600 K, which was used as the initial state before starting the cascade simulations. Note that a previous study has shown that the SFE effect on the ratio of glissile SIA clusters tends to be apparent at 600 K [48].

Table 2.1 Material properties of the interatomic potentials used.

Property	#1	#2	#3	#4	#5	#6
Intrinsic SFE (mJ/m^2)	14.6	24.8	44.1	61.6	94.6	186.5
Lattice constant (Å)	3.639	3.639	3.639	3.639	3.639	3.638
Cohesive energy (eV/atom)	–3.425	–3.416	–3.423	–3.429	–3.428	–3.427
Vacancy migration energy (eV/atom)	0.91	0.91	0.92	0.93	0.95	1.00
Vacancy formation volume (Ω_f/Ω_0)	0.703	0.705	0.708	0.710	0.717	0.731
⟨1 0 0⟩ dumbbell distance (Å)	2.079	2.077	2.076	2.081	2.081	2.080
Formation energy (eV/atom)						
Vacancy	1.11	1.12	1.11	1.10	1.07	1.03
Interstitial	2.82	2.81	2.81	2.82	2.82	2.81
Elastic constant (GPa)						
C_{11}	173	174	174	175	175	178
C_{12}	128	127	127	127	127	125
C_{44}	84	84	84	84	84	83
Melting point (K)	1349	1352	1353	1355	1356	1351

After the equilibrium state of the cell was obtained, an atom near the center of the cell was then given the extra kinetic energy, with the velocity directed in [1 3 5], which was chosen to avoid channeling and prevent the atom from experiencing extremely low and high E_d [60]. Based on the results of a previous study showing that a larger E_{PKA} leads to an enhanced formation of larger clusters, E_{PKA} was set to 50 keV to observe more clearly the effects of SFE on the defect formation processes [47]. Once E_{PKA} was transferred, the simulation was run for ~100 ps with a variable timestep so that the displacement of the fastest atom was less than 1 % of the lattice constant within a single timestep. This value was as low as 10^{-17} s in the initial stage of the simulation while a much larger timestep on the order of 10^{-15} s was allowed after the initiation of the cascade. The simulations were performed in the microcanonical ensemble. To obtain statistically meaningful results, at least 25 independent simulations were conducted for each condition by changing the initial distribution of atomic velocities. Simulations under no strain were also performed to clearly illustrate the strain effect on the defect formation process.

2.2.2 Defect analysis

The Wigner-Seitz defect analysis was conducted to find the defects produced. Note that the energy minimization, using the conjugate gradient method, was performed before the defect analysis to remove the effect of thermal vibration. Groups of four SIAs or more are treated as SIA clusters, and groups of three vacancies or more are treated as vacancy clusters, based on previous studies [33,61]. The dislocation extraction algorithm was used to identify the type of SIA cluster produced; namely, a perfect loop or a Frank loop [62,63]. Generally, SIA clusters have the two energetically stable configurations described above. In real situations, however, some SIA clusters produced through displacement cascades have an irregularly shaped configuration, although it is energetically unstable (Figure 2.6). Identifying the type and character of such SIA clusters is not straightforward. Here, we employed the following procedure to identify their mobility, which was previously reported [48]: the displacements of every SIA cluster are recorded from ~38 to ~50 ps, from ~88 to ~100 ps, and from ~50 ps to ~100 ps. If any displacement along one of the close-packed directions (i.e., ⟨1 1 0⟩) is larger than twice the magnitude of the Burgers vector, the cluster is defined as a glissile one; otherwise, we defined the cluster as a sessile one. This reduced the risk of

identifying a cluster motion caused by core diffusion as a glide.

Figure 2.6 Examples of irregularly shaped SIA clusters produced through displacement cascades.

2.2.3 Calculations of defect formation energies

To elucidate the underlying mechanism of the strain effect on the defect formation, the formation energies of each type of defect were calculated and contrasted with the cascade results obtained. A defect cluster or a Frenkel pair was created at the center of the cubic cell containing ~450,000 or ~45,000 atoms, respectively. Periodic boundary conditions were applied along each direction. The calculated cluster types were a $a_0/2\langle 1\ 1\ 0\rangle$ perfect loop and a $a_0/3\langle 1\ 1\ 1\rangle$ Frank loop for an SIA cluster, and a $a_0/2\langle 1\ 1\ 0\rangle$ perfect loop, a $a_0/3\langle 1\ 1\ 1\rangle$ Frank loop, an SFT and a spherical void for a vacancy cluster. The size of each cluster was varied up to ~120 SIAs/vacancies. It should be noted that previous studies have confirmed that there are two types of Frank loops observed in FCC metals: ones with $\langle 1\ 1\ 0\rangle$ edges and ones with $\langle 1\ 2\ 1\rangle$ edges. The former were observed in Cu and Au [64] and the latter were observed in austenitic stainless steels and Ni [65,66]. Since the interatomic potentials used here were developed based on the potential for pure Cu, Frank loops with $\langle 1\ 1\ 0\rangle$ edges were created in all the simulations. Once the cluster, with the exception of an SFT, was created in the cell, the system energy was minimized using the conjugate gradient method. The obtained system energy (E_{sys}), subtracted by the cohesive energy (E_{coh}) multiplied by the number of atoms in the cell (N_{atoms}), was defined as the formation energy (E_{f}):

$$E_{\mathrm{f}} = E_{\mathrm{sys}} - E_{\mathrm{coh}} \cdot N_{\mathrm{atoms}} \tag{2.2}$$

SFTs were created based on the Silcox–Hirsch mechanism [7]: an equilateral triangular platelet on a [1 1 1] plane was placed at the center of the cell, followed by MD simulations at 600 K for 10–20 ps, resulting in the formation of an SFT. Previous MD studies have also

confirmed the formation of SFTs by the Silcox–Hirsch mechanism [67,68]. Once an SFT was formed, the system energy was minimized accordingly. Note that three independent calculations for evaluating the formation energy of an SFT were performed, and no variation of the results was observed among them. The strain effect on the formation energy of each cluster was also investigated. The strain was applied in the same manner as with the cascade simulations: a Poisson's deformation with a tensile strain magnitude of 0.5 % along the $[1\ \bar{1}\ 0]$ direction was applied while the magnitude was varied from –1.5 to 1.5 % for a Frenkel pair.

2.3 Results

First, we show the results of the MD cascade simulations. Figure 2.7 shows the number of residual defects (N_F) at each SFE under conditions of applied strain and no strain. Note that N_F is defined as the number of SIAs or vacancies that survived at the cooling phase. It is seen that there is no clear dependence of N_F on SFE under applied strain or no strain conditions, agreeing with the results of previous studies where N_F was evaluated under conditions of no strain at E_{PKA} = 1–50 keV and T = 100 K [46,47], and at E_{PKA} = 50 keV and T = 300 K [48]. These results clearly indicate that the strain field does not strongly influence the SFE dependence of N_F. Meanwhile, the value of N_F increases by ~30–70 under the applied strain over the whole range of SFE. Nogarett et al. developed an analytical model (the NRT model) to compute the total number of atoms displaced by a given PKA with E_{PKA}, described as:

$$N_{\mathrm{NRT}} = \kappa \frac{T_{\mathrm{d}}(E_{\mathrm{PKA}})}{2E_{\mathrm{d}}} \tag{2.3}$$

where κ is the displacement efficiency and T_d is called the "damage energy" and is a function of E_{PKA} [69]. The T_d is the PKA energy in which the energy loss of electronic excitation and ionization are considered. The NRT model is a standard tool to compute atomic displacement rates and is often used to derive the defect production efficiency as N_F/N_{NRT}. In this study, N_F/N_{NRT} is calculated as ~0.19 for the no strain condition. Note that κ and E_d are set to 0.8 and 30 eV, respectively, based on previous studies [1,70,71], and T_d is defined as being equal

to E_{PKA} because energy losses of electronic excitation and ionization are not included in MD simulations.

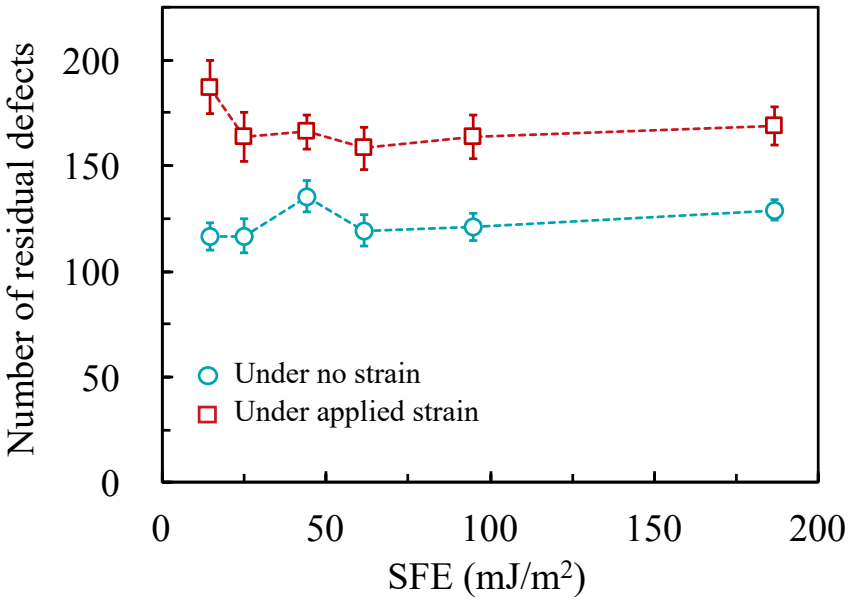

Figure 2.7 Number of residual defects under applied strain or no strain. The error bars denote twice the standard error of the average.

Figure 2.8 shows the number of each type of defect under no strain and applied strain: the number of (a) single SIAs, di-SIAs, tri-SIAs, and SIA clusters, and (b) single vacancies, di-vacancies, and vacancy clusters. Except for single vacancies, the number of defects observed shows no clear SFE dependence, and applying strain does not change this trend. In addition, the presence of a strain field does not lead to an increase in the number of each type of defect, except for single vacancies. Regarding single vacancies, the absolute number of them is much higher compared to the other types of defects, and the number increases slightly with an increase in SFE, and this trend is preserved under applied strain. In addition, applying strain enhances the formation of single vacancies by ~10–20.

Figures 2.9 and 2.10 show the size distribution of the clusters of SIAs and those of vacancies, respectively. It is observed that a variation of SFE does not change the size distribution of SIA or vacancy clusters. This agrees with previous studies, where the size distribution of defect clusters was examined using the same potentials at E_{PKA} = 1–50 keV

and T = 100 K [46,47] and at E_{PKA} = 50 keV and T = 300 K [48]. This trend is preserved under applied strain, as shown. Meanwhile, it seems that applying strain enhances the formation of larger SIA clusters, while the size of vacancy clusters formation increases uniformly with respect to size. This trend is observed over the whole SFE range. Miyashiro et al. also found a similar trend in the size distribution of formed SIA clusters, where they performed MD simulations of cascade events in Cu while changing E_{PKA} up to 30 keV under [1 1 1] uniaxial strain [45].

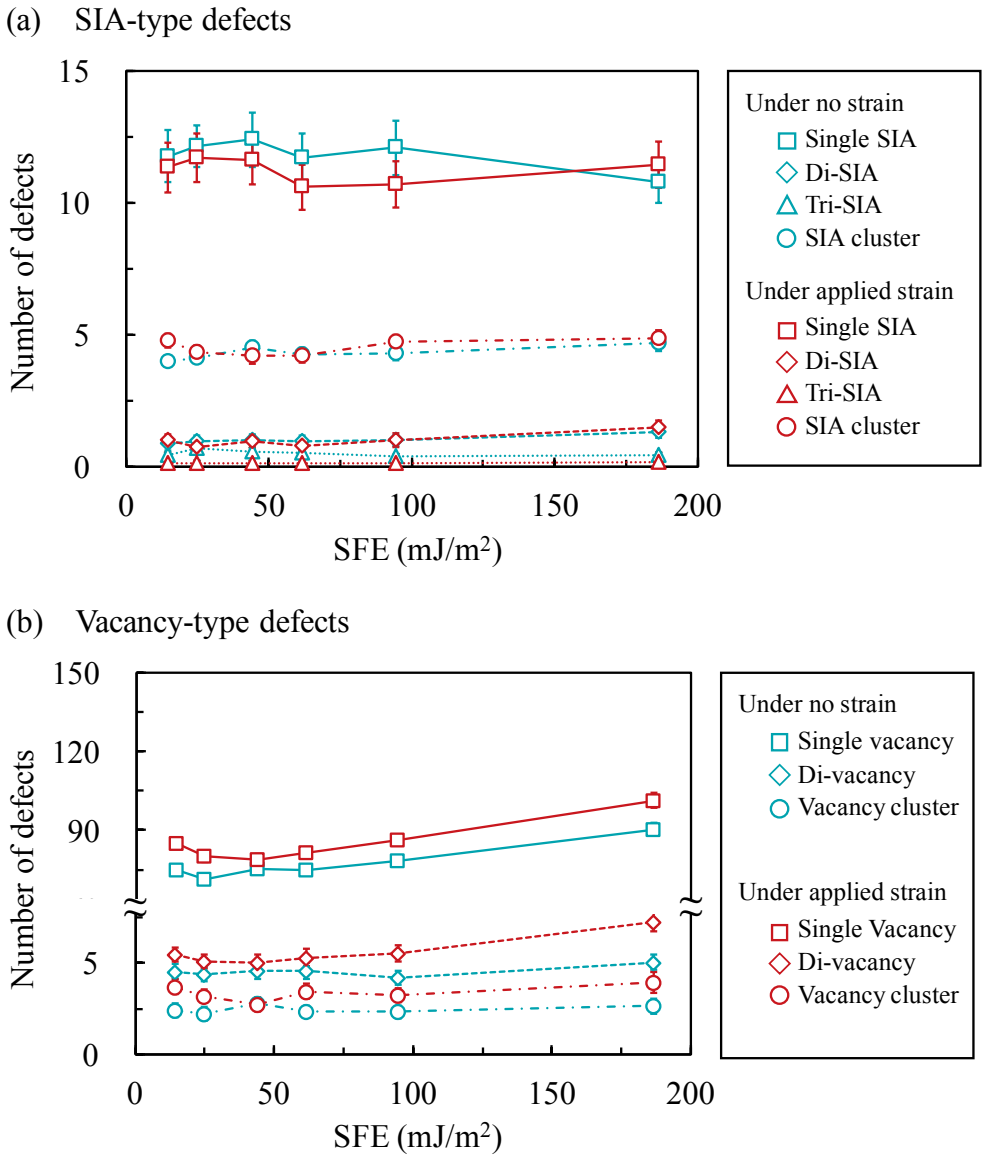

Figure 2.8 Number of defects formed relative to SFE under conditions of no strain or applied strain: (a) SIA defects and (b) vacancy defects.

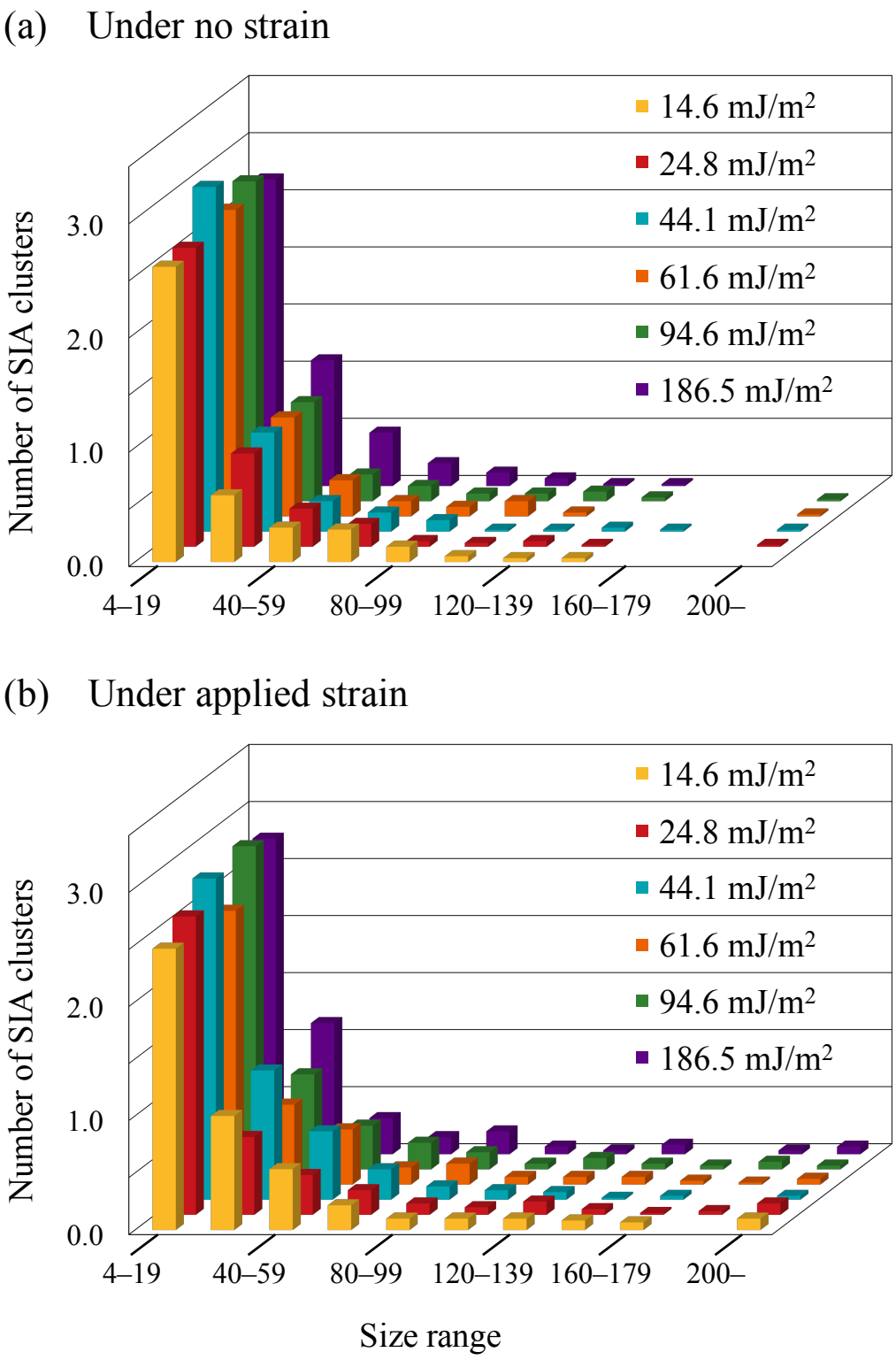

Figure 2.9 Size distribution of SIA clusters under (a) no strain and (b) applied strain

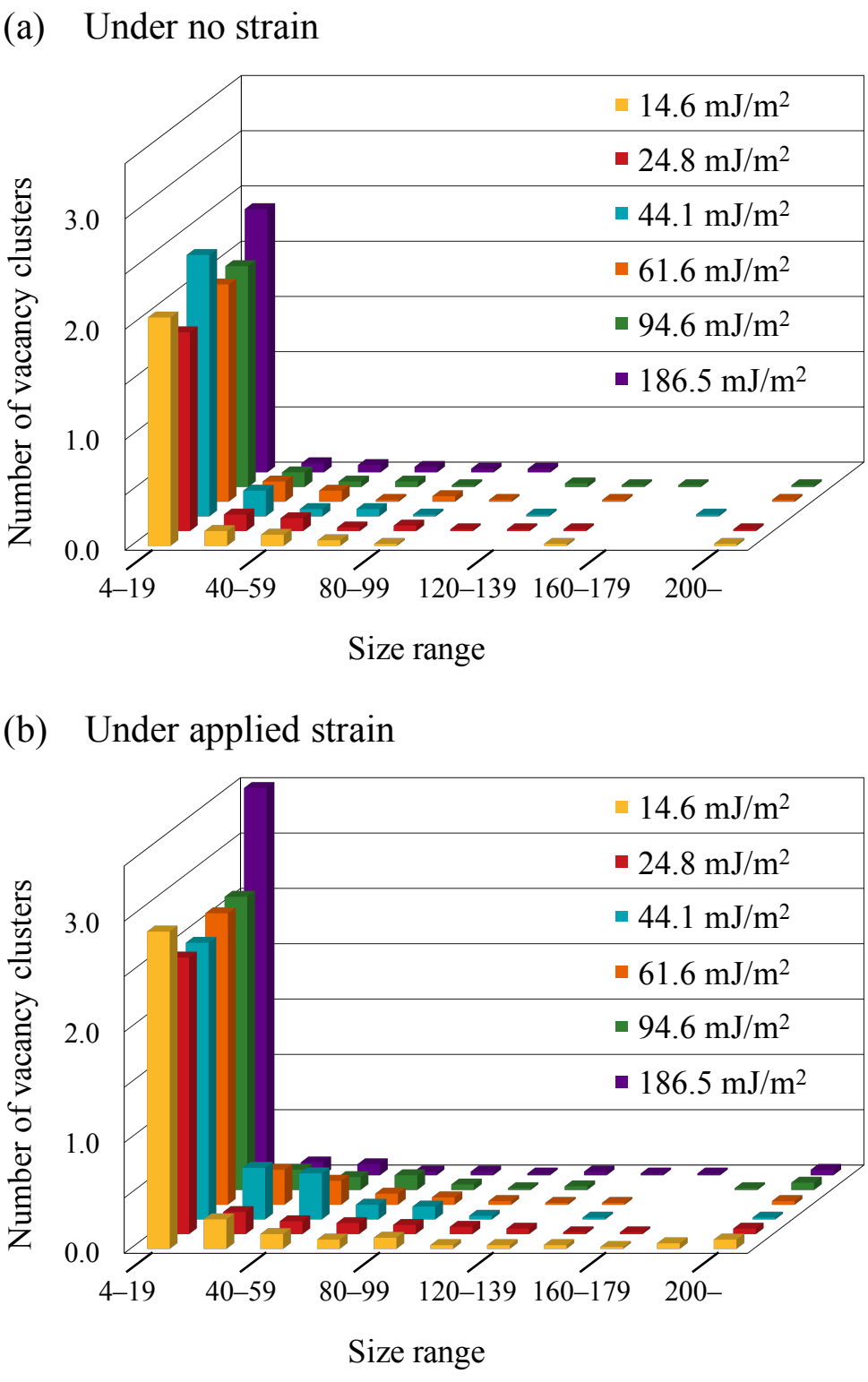

Figure 2.10 Size distribution of vacancy clusters under (a) no strain and (b) applied strain.

Figures 2.11–2.14 show the number of SIA perfect loops, SIA Frank loops, irregularly shaped glissile SIA clusters, and irregularly shaped sessile SIA clusters, respectively. The lines drawn in the figures were obtained by the least squares method. The number of SIA perfect loops decreases with an increase in SFE, as seen in Figure 2.11, which agrees with previous studies, where MD simulations of displacement cascades were performed using the same potentials as in this study at E_{PKA} = 20 or 50 keV and T = 100 K [46,47] and at E_{PKA} = 50 keV and T = 300 K [48]. In addition, the slopes of the two fitted lines in the figure are almost the same, indicating that the applied strain does not change the SFE dependence of the SIA perfect loop formation, while it enhances their formation to some extent. In dislocation theory, the formation energy of SIA perfect loops is independent of SFE because it does not consider the dissociation of loop edges into partial dislocations. This leads to the prediction that SIA perfect loop formation has no SFE dependence under irradiation [49]. In the simulations, however, almost all the SIA perfect loops produced through displacement cascades had edges that dissociated into partial dislocations bounding stacking fault areas (Figure 2.15). The formation of such SIA perfect loops with dissociated edges was also confirmed in previous studies [46–48]. Due to the creation of stacking fault areas at the edges, a strong dependence on SFE for the formation of SIA perfect loops is observed. Meanwhile, there is no clear dependence on SFE for SIA Frank loop formation under no strain and applied strain, as seen in Figure 2.12. Under applied strain, the number of formed SIA Frank loops slightly increases with an increase in SFE; however, the increase is within the statistical variation. Since Frank loops contain stacking fault areas on their habit plane (Figure 2.16), their formation is expected to be influenced by variations in SFE. In the simulations, however, the absolute number of formed Frank loops is very low, and is insufficient to clearly exhibit SFE dependence, even if Frank loop formation has SFE dependence. Figure 2.13 shows the number of irregularly shaped glissile SIA clusters, which indicates that there is no SFE dependence of their formation under no strain and applied strain. Further, applied strain does not strongly affect the formation of these SIA clusters. Meanwhile, the formation of irregularly shaped sessile SIA clusters is strongly affected by variations in SFE; the formation of these clusters increases with an increase in SFE. In addition, the strain decreases the number of them over the whole SFE range, while the trend with respect to SFE is not affected.

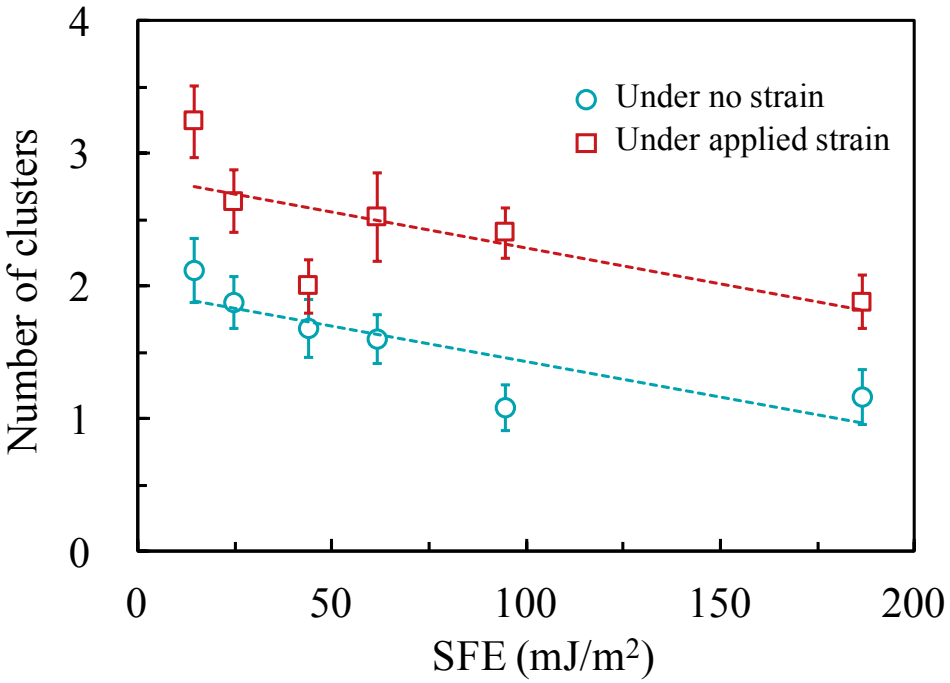

Figure 2.11 Number of SIA perfect loops

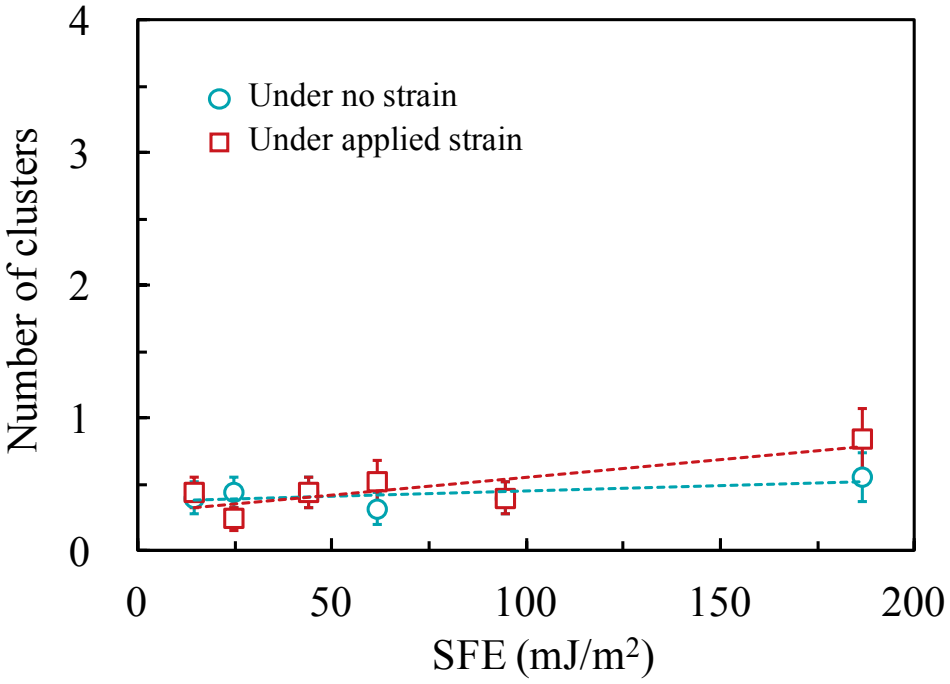

Figure 2.12 Number of SIA Frank loops

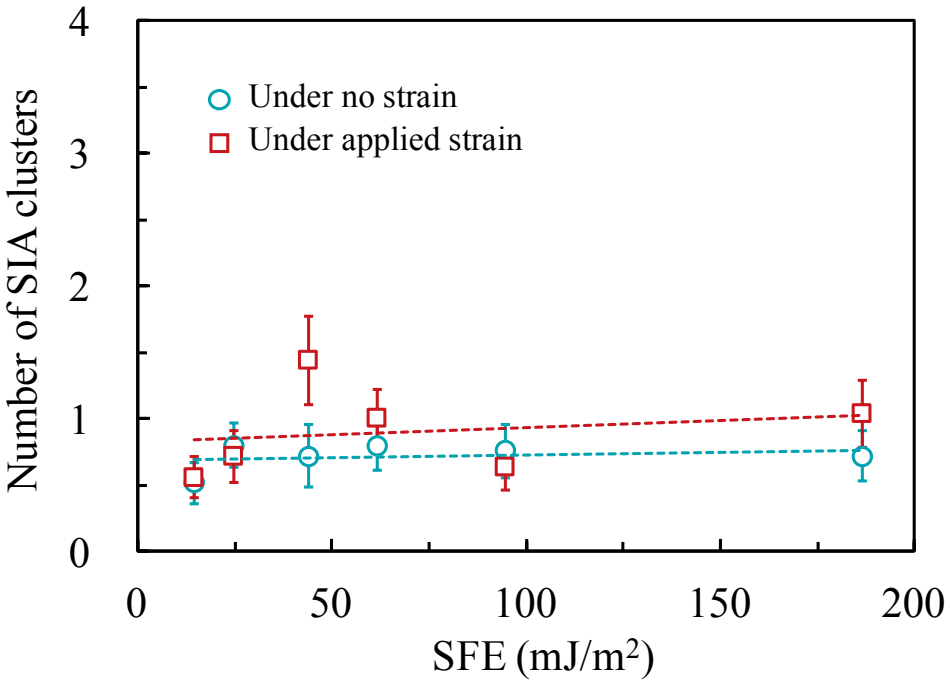

Figure 2.13 Number of irregularly shaped glissile clusters.

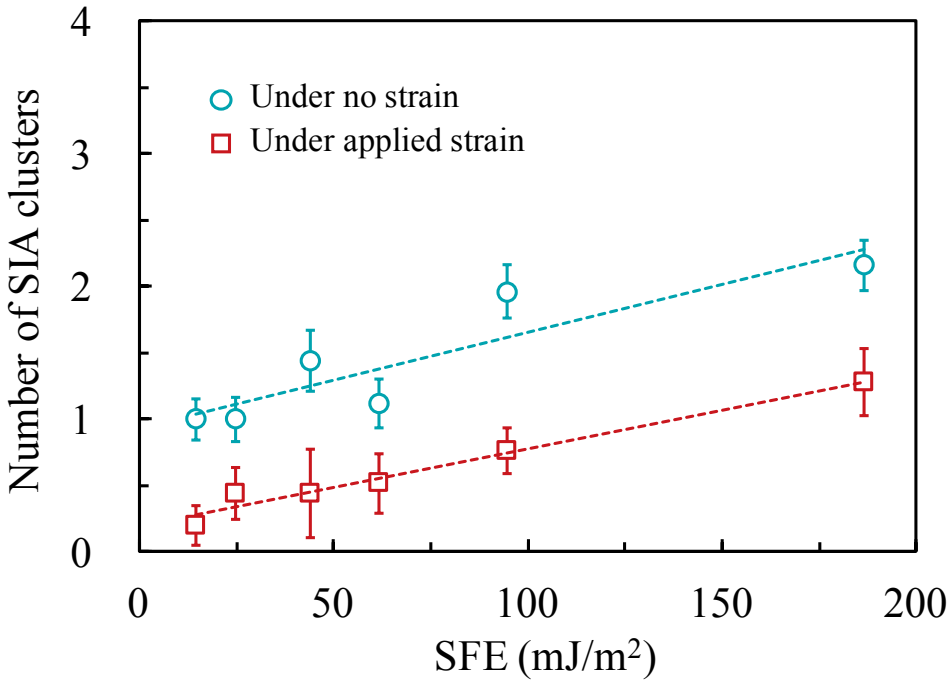

Figure 2.14 Number of irregularly shaped sessile clusters.

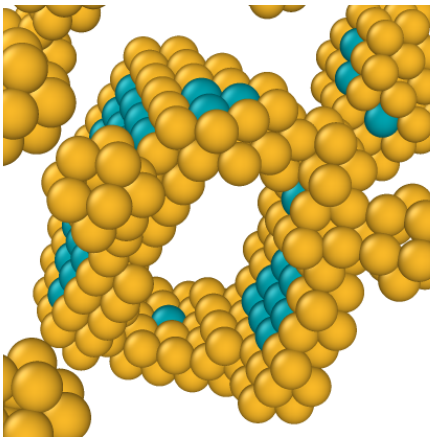

Figure 2.15 SIA perfect loop with split edges observed in the simulations.

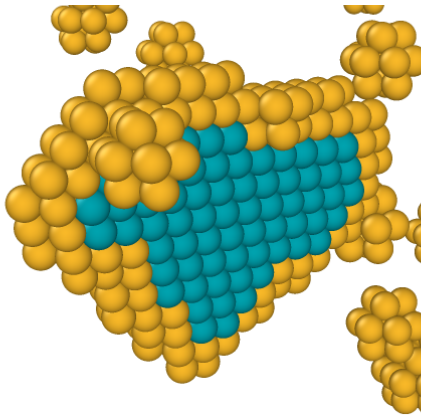

Figure 2.16 SIA Frank loop observed in the simulations.

Figure 2.17 shows the ratio of glissile SIA clusters, which are obtained by the numbers of each type of SIA cluster. The ratio of glissile SIA clusters decreases with an increase in SFE, which agrees with previous studies, conducted at E_{PKA} = 10–50 keV and T = 100 K [46,47] and E_{PKA} = 50 keV and T = 300 K [48]. This trend is preserved under applied strain, although the strain enhances the formation of glissile SIA clusters to some extent. The strong SFE dependence of glissile SIA clusters arises from two factors: a decrease in the number of SIA perfect loops with an increase in SFE and an increase in the number of irregularly shaped sessile SIA clusters with an increase in SFE, as seen in Figures 2.11 and 2.14, respectively. It should be noted that the opposite trend of the ratio of glissile SIA clusters with respect to SFE is obtained based on the dislocation theory owing to the assumption that the formation energy of SIA perfect loops is independent of SFE [49].

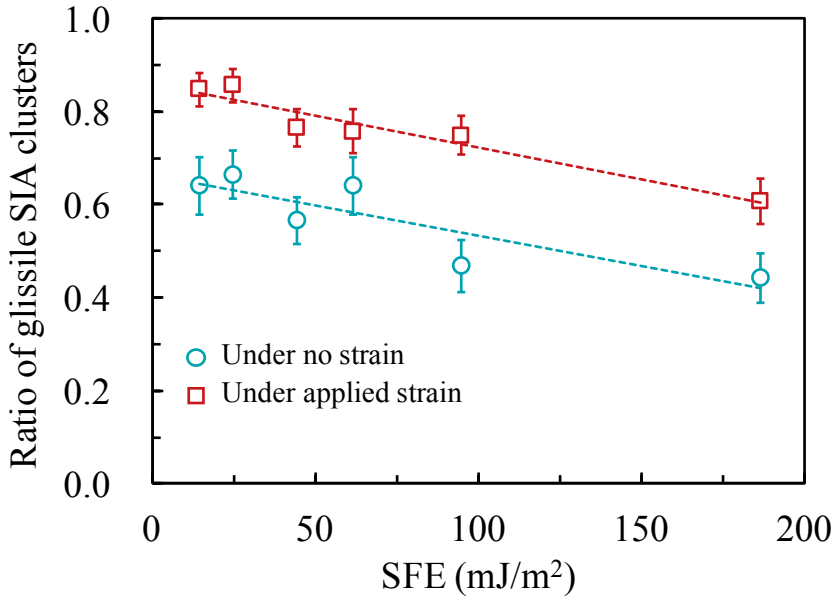

Figure 2.17 Ratio of glissile SIA clusters.

Figures 2.18–2.20 show the ratio of SIA perfect loops with each Burgers vector, the number of SIA perfect loops with a certain Burgers vector divided by the total number of SIA perfect loops produced. There is no clear SFE dependence over the whole SFE range under no strain and applied strain. Meanwhile, the absolute number of loops produced is dependent on the Burgers vector direction. The formation of $a_0/2\,[1\,\bar{1}\,0]$ loops is enhanced by the applied strain, while that of $a_0/2\,[1\,1\,0]$ loops is rarely observed, as seen in Figure 2.18. The simulation cell is elongated along the $[1\,\bar{1}\,0]$ direction yet compressed along the perpendicular direction. This renders the atomic distances along the $[1\,\bar{1}\,0]$ direction relatively short, and SIAs can aggregate between $(1\,\bar{1}\,0)$ planes relatively easily, while the opposite occurs along the $[1\,1\,0]$ direction. These results explain the geometrical preference of $a_0/2\,[1\,1\,0]$ loop formation.

Figures 2.21 and 2.22 show the ratio of SIA Frank loops with each Burgers vector, the number of SIA Frank loops with a certain Burgers vector divided by the total number of SIA Frank loops produced. There is no clear SFE dependence of the ratio over the whole SFE range under no strain and applied strain, although relatively large statistical variations are seen because the formation of SIA Frank loops is very infrequent. Regarding the strain effect on the formation, it is seen that the formation of SIA Frank loops with the $a_0/3\,[\bar{1}\,\bar{1}\,1]$ and $a_0/3\,[1\,1\,1]$ Burgers vector is rarely observed under applied strain. In this study, the

simulation cell is compressed along the direction perpendicular to $[1\ \bar{1}\ 0]$; hence, the atomic distances along the $[\bar{1}\ \bar{1}\ 1]$ and $[1\ 1\ 1]$ directions are relatively shortened and too energetically unstable for SIAs to aggregate between $(\bar{1}\ \bar{1}\ 1)$ or $(1\ 1\ 1)$ planes.

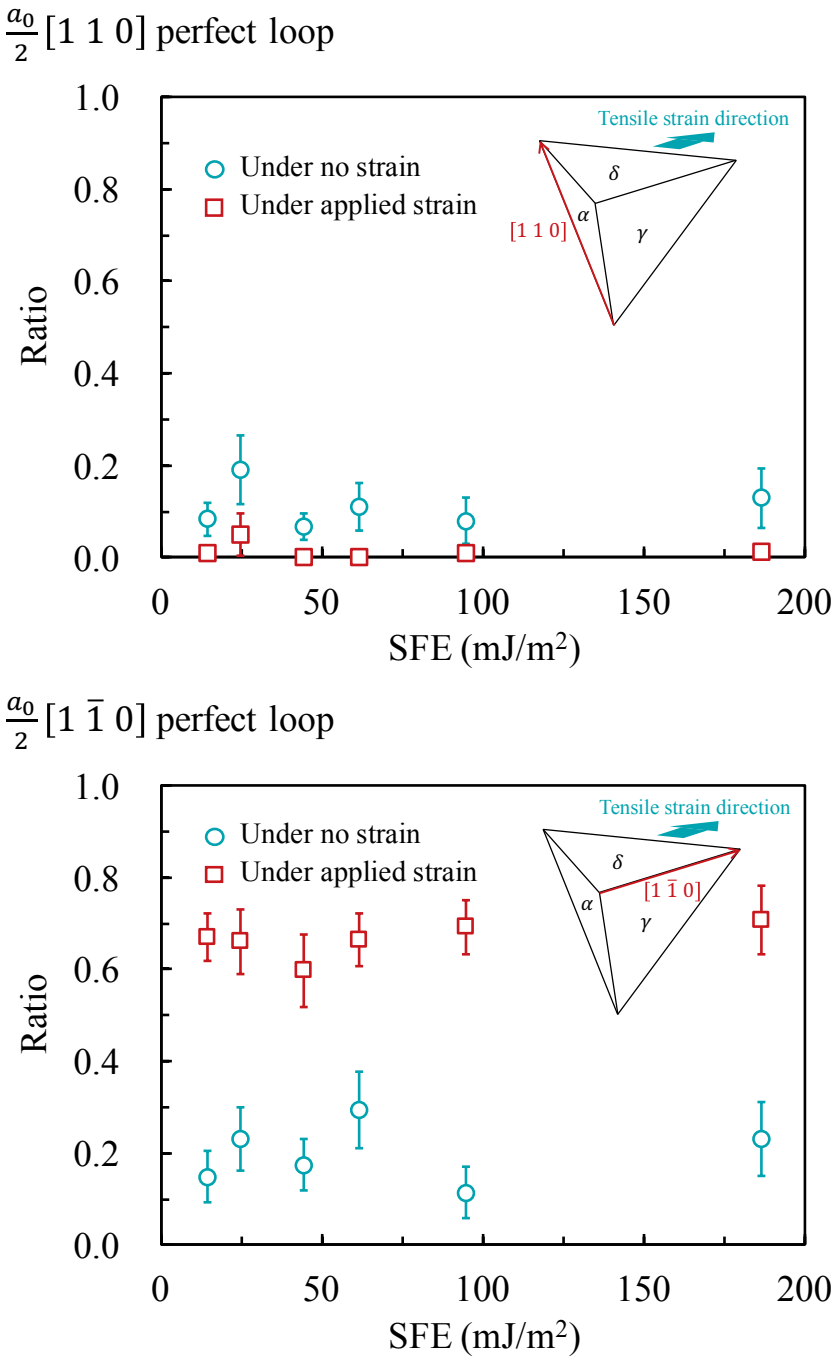

Figure 2.18 Ratio of SIA perfect loops with each Burgers vector: $a_0/2\,[1\ 1\ 0]$ and $a_0/2\,[1\ \bar{1}\ 0]$.

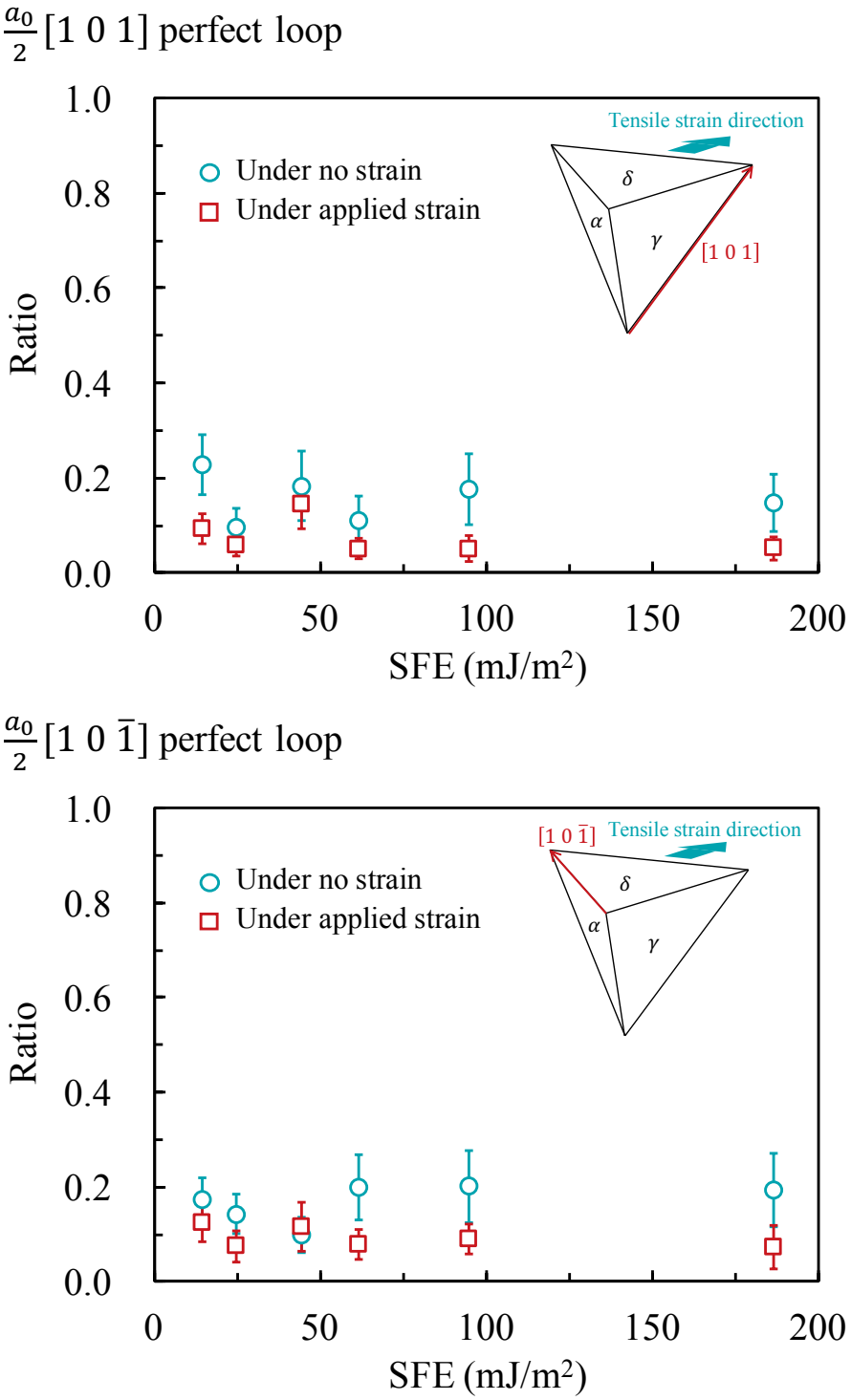

Figure 2.19 Ratio of SIA perfect loops with each Burgers vector: $a_0/2\,[1\ 0\ 1]$ and $a_0/2\,[1\ 0\ \bar{1}]$.

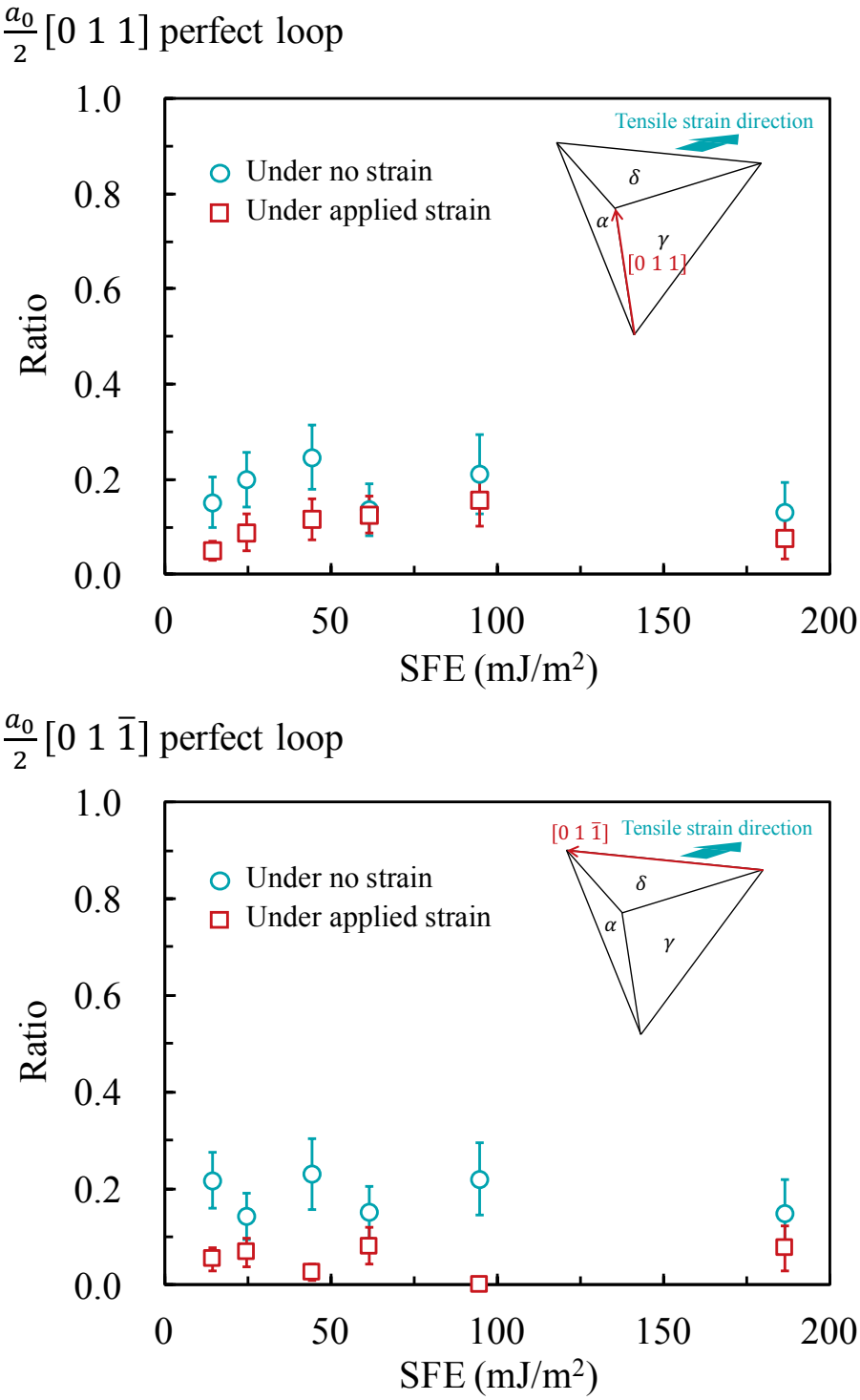

Figure 2.20 Ratio of SIA perfect loops with each Burgers vector: $a_0/2\,[0\,1\,1]$ and $a_0/2\,[0\,1\,\bar{1}]$.

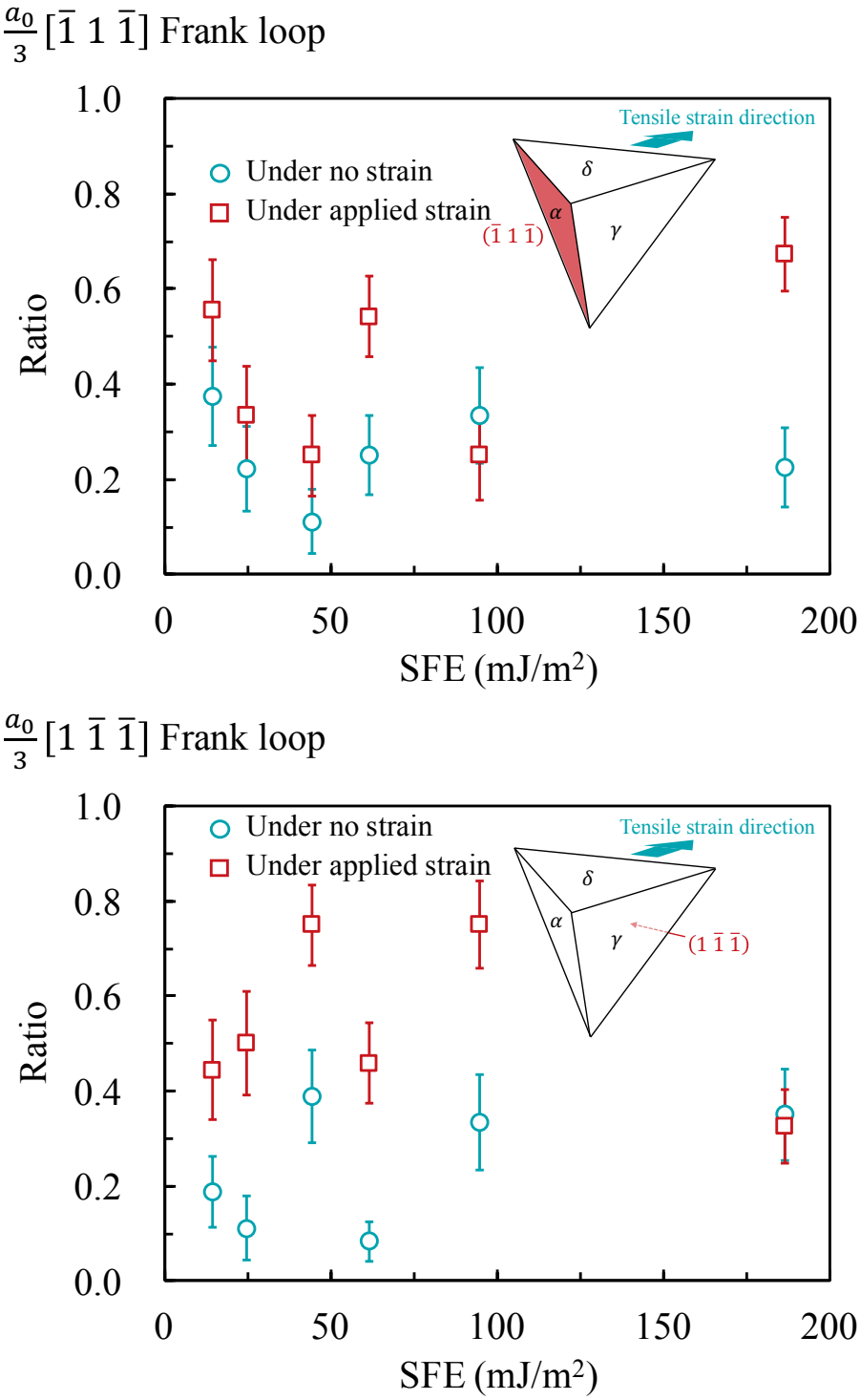

Figure 2.21 Ratio of SIA Frank loops with each Burgers vector: $a_0/3\,[\bar{1}\ 1\ \bar{1}]$ and $a_0/3\,[1\ \bar{1}\ \bar{1}]$.

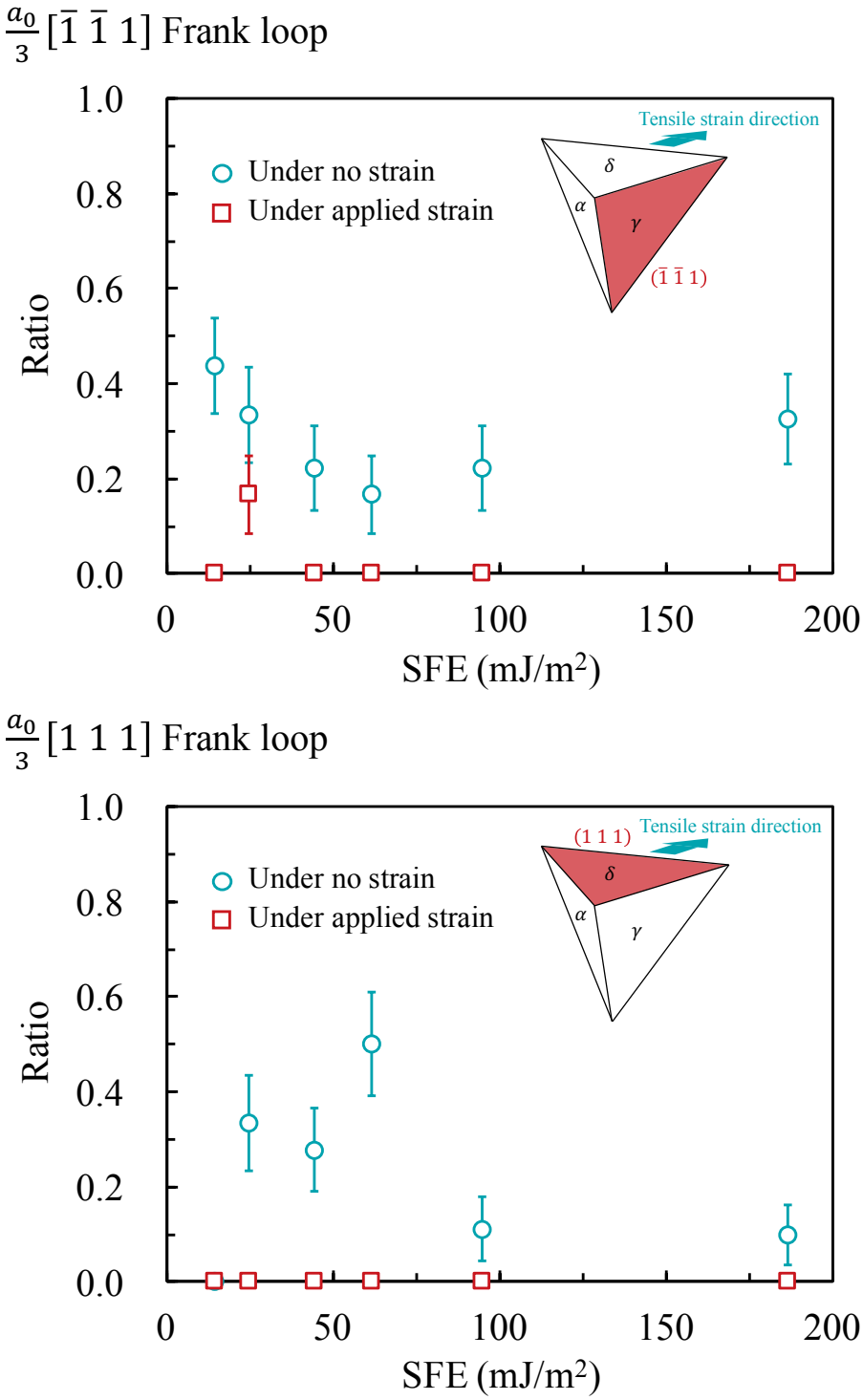

Figure 2.22 Ratio of SIA Frank loops with each Burgers vector: $a_0/3\,[\bar{1}\ \bar{1}\ 1]$ and $a_0/3\,[1\ 1\ 1]$.

2.4 Discussion

In this section, the MD results are discussed in detail, together with the formation energies of defect clusters and a Frenkel pair. Miyashiro et al. [44] found that the deformation anisotropy is a critical factor affecting N_F, while the volume increase caused by the deformation also induces an increase in N_F to some extent. Considering the strain employed in this study involved an anisotropic deformation and a volume increase of ~0.1 %, the observed increase in defect production, as seen in Figure 2.7, is mainly caused by these two factors. Further, Beeler et al. [39] investigated the strain effect on the formation energy of a Frenkel pair (E_f^{fp}) in BCC iron and found that the formation energy was reduced by the volume increase, which resulted in an increase in N_F. Similar effects of volume increase on the formation energy of a Frenkel pair were also observed in tungsten by Wang et al. [40], and in zirconium by Sahi et al. [43]. The variation of E_f^{fp} by applied strain was investigated for the interatomic potentials used in this study, as shown in Figure 2.23. Note that the horizontal axis expresses the strain along the tensile strain direction. It is observed that E_f^{fp} decreases with an increase in the strain, and this is one of the factors that caused the increase in N_F under applied strain, as shown in Figure 2.7. It is surprising that an energy difference as low as ~0.01–0.10 eV causes a significant variation in the number of defects produced by displacement cascadesg, which involve E_{PKA} values as high as tens of keV. Together with the fact that a decrease in E_f^{fp} through a volume increase is also observed in BCC and HCP materials, this is a common phenomenon regardless of crystal structure. In addition, the change in E_f^{fp} due to applied strain is not strongly affected by variations in SFE, which suggests that the increase in N_F due to the decrease in E_f^{fp} is almost independent of SFE. This leads to the implication that the effect of the deformation anisotropy on N_F is independent of SFE, under the assumption that the increase in N_F is mainly caused by the deformation anisotropy and the decrease in E_f^{fp}.

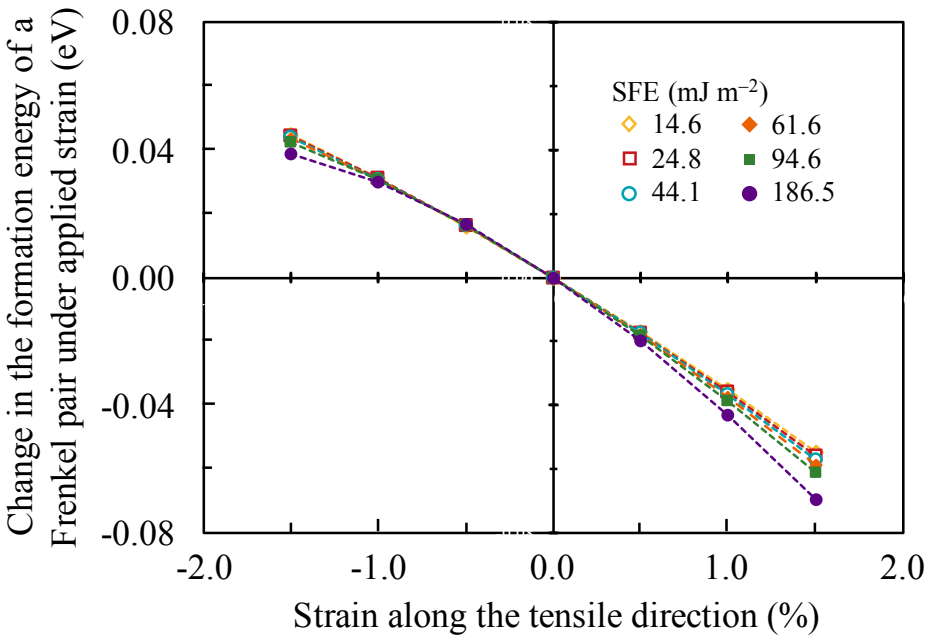

Figure 2.23 Formation energy of a Frenkel pair under various applied strains.

Figure 2.8 clearly shows that there is an imbalance between the increase in the number of SIA defects and the increase in the number of vacancy defects: the number of single vacancies increases by ~10–20 under applied strain, while the numbers of single SIAs, di-SIAs, tri-SIAs, and SIA clusters are almost unchanged. This implies that the increased amount of SIAs are contained by SIA clusters, and larger SIA clusters are formed under applied strain. Figure 2.24 shows the formation energies of each type of SIA cluster as a function of the number of SIAs composing the cluster (N_{SIA}): a rhombic perfect loop, a hexagonal perfect loop, and a hexagonal Frank loop. Note that the energies are derived with the interatomic potential at Γ_{SFE} = 44.1 mJ m^{-2}, and the Burgers vector direction is chosen so that the cluster becomes energetically most stable under the applied strain; namely, the $a_0/2\,[1\,\bar{1}\,0]$ for a perfect loop and the $a_0/3\,[1\,\bar{1}\,\bar{1}]$ for a Frank loop. It is clearly observed that the rhombic perfect loops are energetically the most stable configuration of SIA clusters, which agrees with a previous study where the formation energies of each type of SIA cluster were calculated in copper under no strain [72]. In addition, the strain decreases the formation energy of the SIA clusters, and the decreased amount was larger for larger clusters, indicating that the formation of larger SIA clusters is affected more strongly by strain. These trends are also observed when the energy calculations are employed using the other interatomic

potentials, which explains why the numbers of larger clusters tend to increase more under applied strain, as seen in Figure 2.9. Figure 2.25 shows the formation energies of each type of vacancy cluster as a function of the number of vacancies composing the cluster: a perfect loop, a Frank loop, an SFT, and a void. Note that the energies are derived with the interatomic potential at Γ_{SFE} = 44.1 mJ m^{-2}, and the Burgers vector direction is chosen so that the cluster becomes energetically most stable under applied strain; namely, the $a_0/2\,[1\,1\,0]$ for a perfect loop and the $a_0/3\,[\bar{1}\,\bar{1}\,1]$ for a Frank loop. It is observed that the formation energies of vacancy clusters do not change through the applied strain. Further, the formation energy of a single vacancy was also evaluated, and strain has little effect on it; the evaluated energy is 1.105 eV under no strain and 1.110 eV under applied strain. Similar negligible strain effects on the formation energies of vacancy defects are also observed when using other interatomic potentials. These results indicate that strain hardly affects the clustering of vacancies, leading to a uniform increase in the number of vacancy clusters over the whole size range under applied strain. Summarizing these considerations, the strain affects the formation energies of SIA clusters, especially of larger clusters, leading to a biased increase in the number of larger SIA clusters. Meanwhile, the formation energies of vacancy clusters are hardly affected by strain over the whole range of cluster sizes, leading to the uniform increase in the number of vacancy clusters.

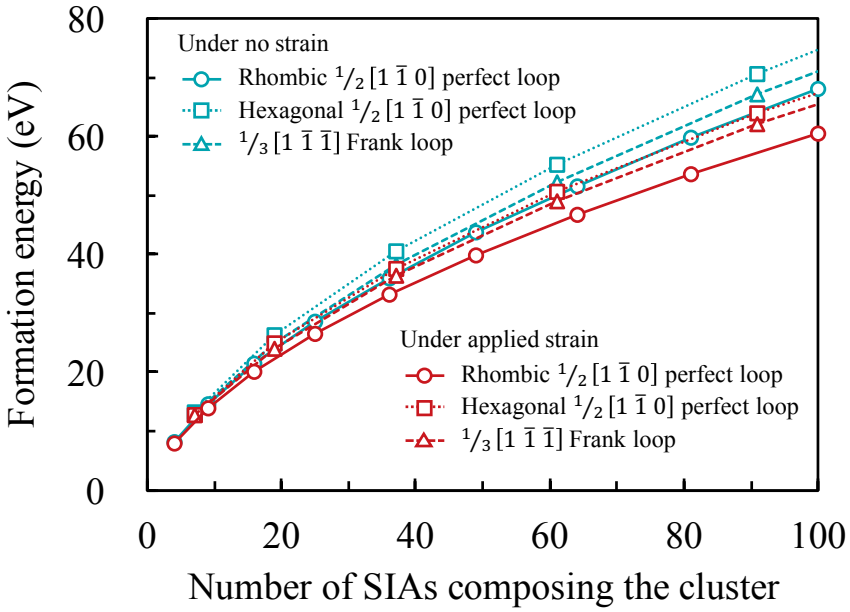

Figure 2.24 Formation energy of each type of SIA cluster.

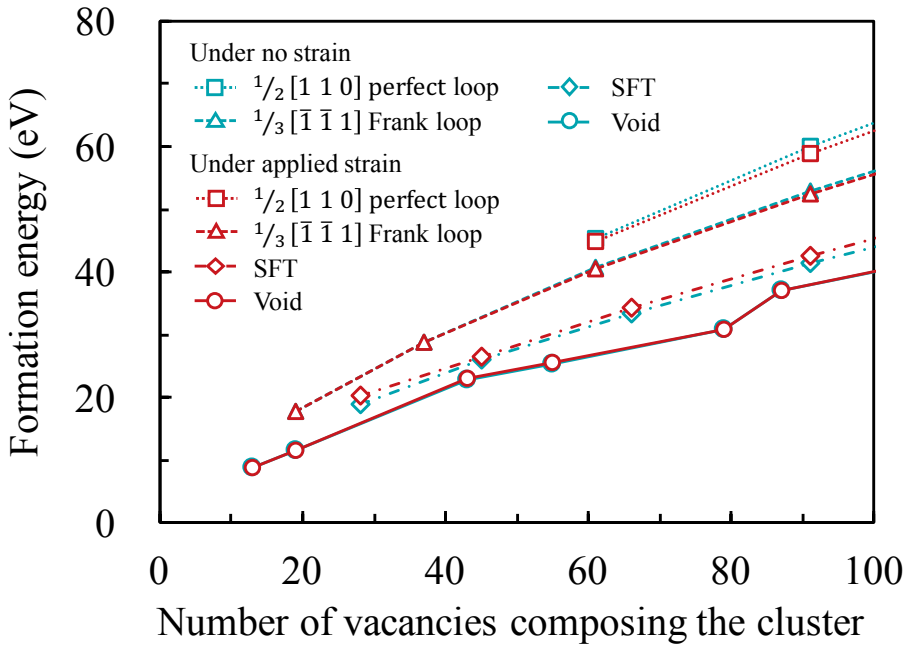

Figure 2.25 Formation energy of each type of vacancy cluster.

Figure 2.26 shows the change in the formation energy of each type of SIA cluster by applied strain as a function of SFE. Here, the Burgers vector of the loops is oriented along the direction that is most energetically favorable ($a_0/2\,[1\,\bar{1}\,0]$ for a perfect loop and $a_0/3\,[1\,\bar{1}\,\bar{1}]$ for a Frank loop, denoted in red), and the direction that is most energetically unfavorable ($a_0/2\,[1\,1\,0]$ for a perfect loop and $a_0/3\,[1\,1\,1]$ for a Frank loop, denoted in yellow) under applied strain. It is observed that there is no strong SFE dependence of the change in the formation energy by applied strain, regardless of the cluster configuration and cluster size. Therefore, the ratio of the number of SIA clusters with each Burgers vector to the total number of SIA clusters is influenced by the applied strain uniformly over the whole SFE range, as shown in Figures 2.18–2.22. In other words, the strain affects the formation energy of SIA clusters depending on the Burgers vector direction, not on the value of SFE.

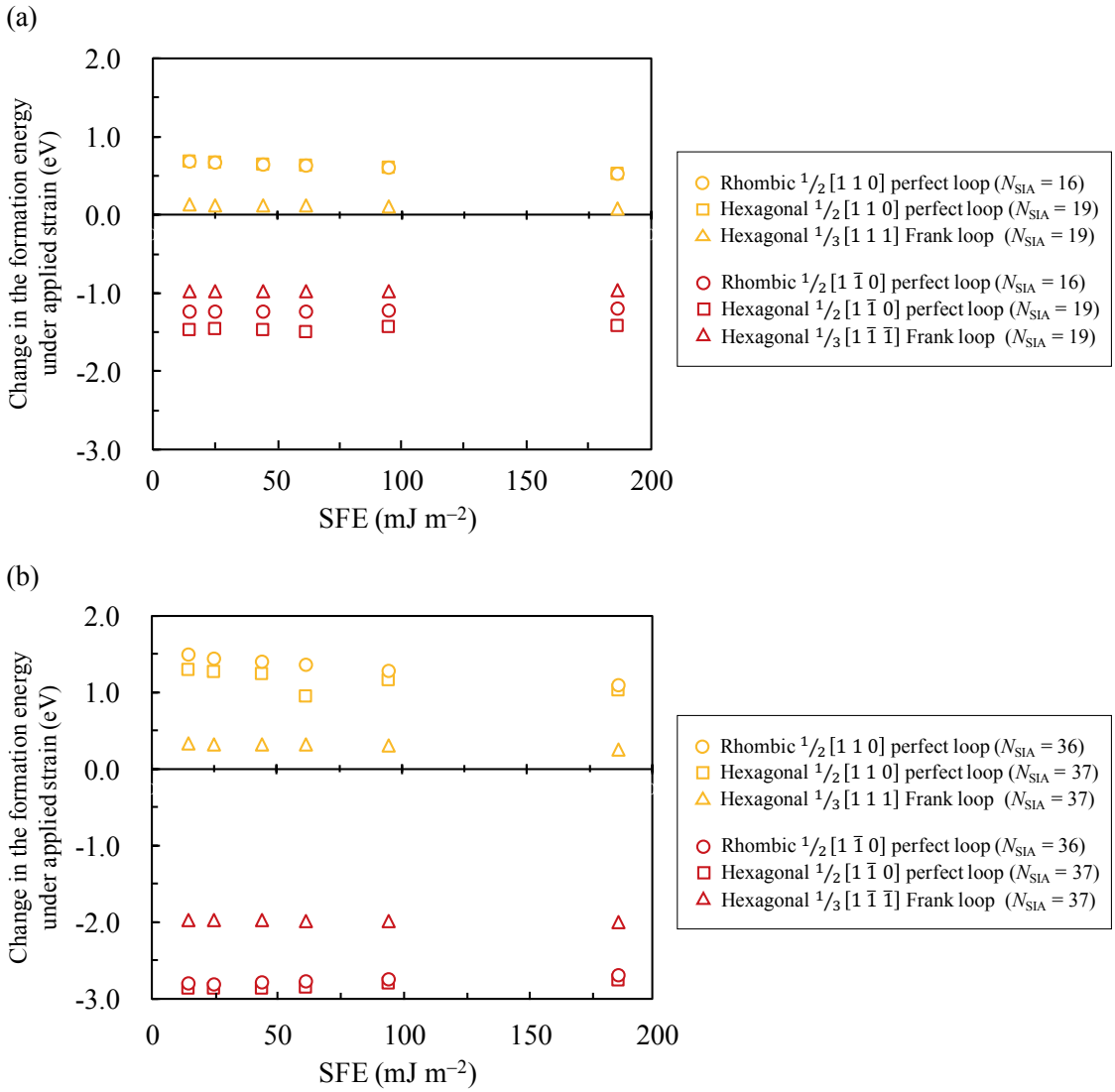

Figure 2.26 Change in the formation energy of each type of SIA clusters under applied strain.

The energetically stable configuration of SIA clusters depends on the shape, i.e., a perfect loop is a stable configuration for rhombic clusters while a Frank loop is a stable configuration for hexagonal clusters, as shown in Figure 2.24. The difference in the formation energy between these two configurations ($\Delta E_{\mathrm{F-P}}$) is quite relevant to the formation ratio of perfect loops and Frank loops under irradiation, which directly affects the ratio of glissile SIA clusters. Figure 2.27 shows $\Delta E_{\mathrm{F-P}}$ as a function of SFE: (a) N_{SIA} = 19 and 37 and (b) N_{SIA} = 61 and 91. Here, the Burgers vector of the loops is oriented along the direction that is most energetically favorable under applied strain, i.e., $a_0/2\,[1\,\bar{1}\,0]$ for a perfect loop and $a_0/3\,[1\,\bar{1}\,\bar{1}]$ for a Frank loop. Regarding the value of N_{SIA}, it increases as the loop becomes

larger, following $N_{SIA} = (N_{edge})^2$ for rhombic loops while $N_{SIA} = 3(N_{edge})^2 - 3N_{edge} + 1$ for hexagonal loops, where N_{edge} expresses the number of SIAs on the loops' edge. For comparing the energy of a rhombic perfect loop and that of a hexagonal Frank loop using the same N_{SIA}, the former is obtained by linear interpolation using the energy of the loop at $N_{SIA} = (N_{edge})^2$. The figure clearly shows that ΔE_{F-P} decreases with an increase in SFE, except for the case of $N_{SIA} = 61$ and 91 at $\Gamma_{SFE} = 186.5$ mJ m^{-2}. This is the main reason for the preferable formation of SIA perfect loops at lower SFE, as shown in Figure 2.11. Moreover, the values of ΔE_{F-P} are increased owing to the applied strain, which corresponds to the enhanced formation of SIA perfect loops over the whole SFE range under applied strain (Figure 2.11). Interestingly, the results indicate that an energy difference of the order of 1.0 eV causes a significant variation of defect formations through the cascade events, which involves E_{PKA} values as high as tens of keV.

On the other hand, the plots of $N_{SIA} = 61$ and 91 at $\Gamma_{SFE} = 186.5$ mJ m^{-2} deviate from the fitted lines obtained from the other SFE plots. This is because the SFE dependence of the formation energy is different between smaller SIA perfect loops and larger ones. Figure 2.28 shows SIA perfect loops of $N_{SIA} = 36$, 64, and 169 at $\Gamma_{SFE} = 44.1$ and 186.5 mJ m^{-2}. As discussed above, the edges of perfect loops split into partial dislocations bounding stacking fault areas. It should be noted that the partial dislocations need to constrict at the two vertices of the edge (indicated by red circles in the figure). Affected by this constriction, stacking fault areas tend to be narrower than the stacking fault ribbon of a line edge dislocation, particularly for smaller loops. With an increase in the loop size, the width of the stacking fault areas of the loops becomes wider and gets closer to that of a line edge dislocation, as seen in Figure 2.28 (a). This results in a more than linear relationship between loop formation energy and loop size. Contrarily, when a certain loop size is reached, the width of the stacking fault areas becomes almost equal to that of a line edge dislocation. Over this critical loop size, the width no longer becomes larger with an increase in the loop size, resulting in an almost linear relationship between loop formation energy and loop size. This relationship depicts the gentler curve of the formation energy increase with respect to loop size, compared with that below the critical loop size. In other words, the loop formation energy follows two kinds of loop-size dependences; namely, a more than linear dependence and a linear dependence, which switches at the critical loop size. This results in a larger ΔE_{F-P} over the critical loop

size. Obviously, the critical loop size is dependent on the value of SFE, and it becomes smaller at higher SFE. As seen in Figure 2.28, the stacking fault width at Γ_{SFE} = 186.5 mJ m^{-2} does not become wider over N_{SIA} = 64 while that at Γ_{SFE} = 44.1 mJ m^{-2} does. This indicates that the critical loop size at Γ_{SFE} = 186.5 mJ m^{-2} exists somewhere between N_{SIA} = 36 and 64. These results suggest that the trend of increasing ΔE_{F-P} with a decrease in SFE, discussed above, is valid only below the critical loop size. In the present study, the majority of generated SIA clusters are smaller than N_{SIA} = ~40, as shown in Figure 2.9, which led to the negligible influence of the ΔE_{F-P} of the clusters over the critical loop size, such as in the deviating plots at Γ_{SFE} = 186.5 in Figure 2.24 (b). Hence, the overall trend shows that the number of SIA perfect loops increases with a decrease in SFE.

As mentioned above, previous studies have also confirmed that the number of SIA perfect loops increases with a decrease in SFE [46–48]. In these studies, the employed E_{PKA} was varied up to 50 keV, and the sizes of produced SIA clusters were smaller than the critical loop size in most cases, which is also the case in this study. Meanwhile, considering that an increase in E_{PKA} induces an increase in the produced SIA cluster size [47], much larger SIA clusters are likely to be produced under irradiation with E_{PKA} of the order of 100 keV. Under such conditions, it is unclear whether the SFE dependence of SIA perfect loop formation that is obtained here would still be observed. To clarify this, it is necessary to perform cascade simulations under much higher E_{PKA} conditions in future studies.

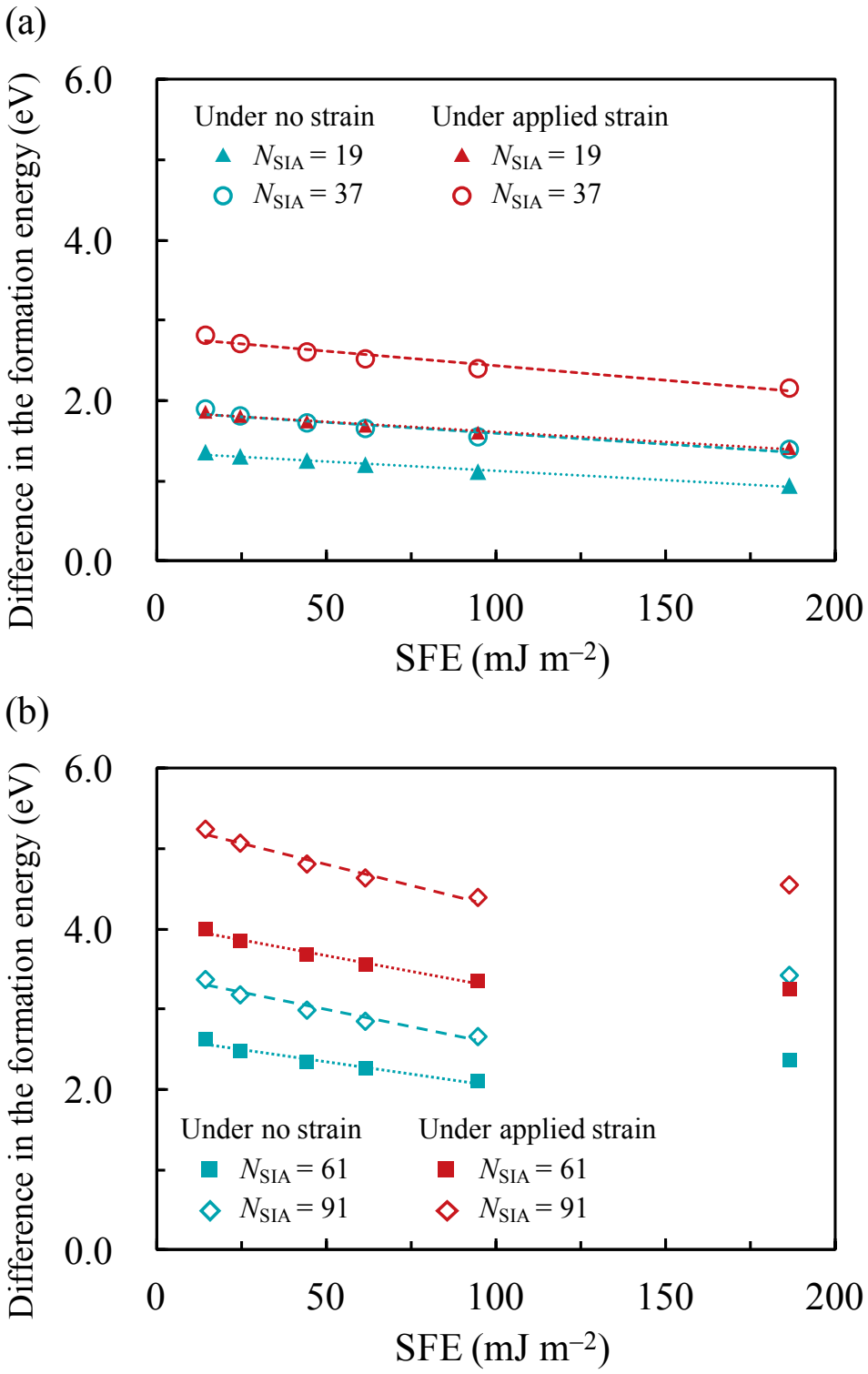

Figure 2.27 Change in the formation energy of each type of SIA cluster under applied strain.

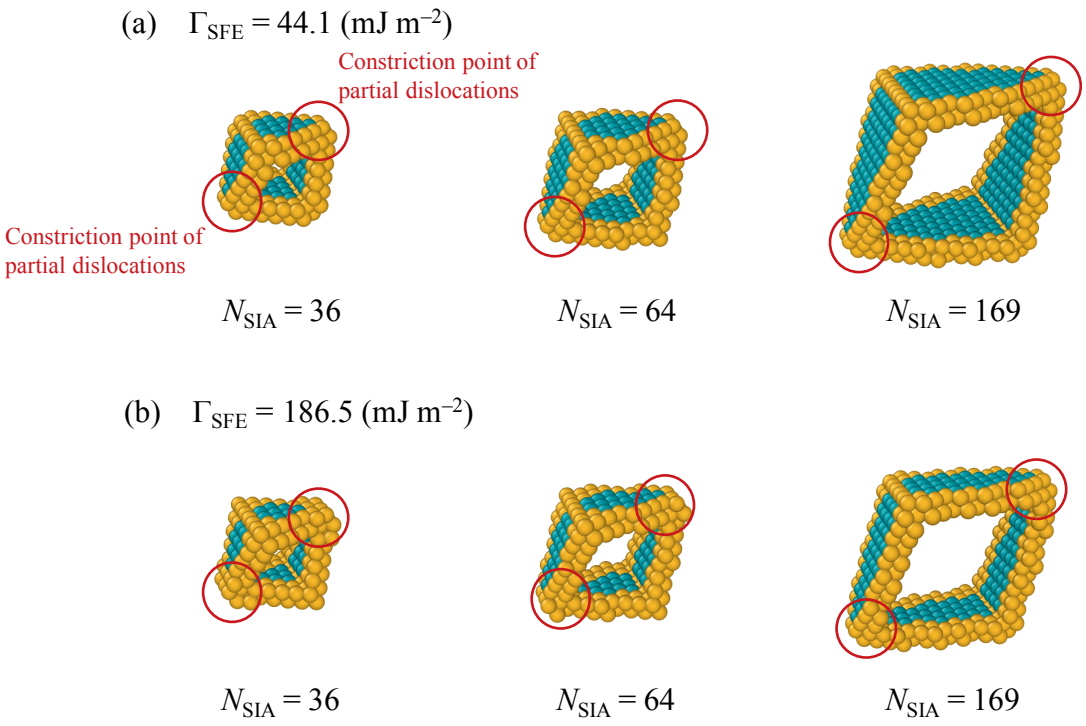

Figure 2.28 SIA Perfect loop configuration of N_{SIA} = 36, 64, and 169 at Γ_{SFE} = 44.1 and 186.5 mJ m^{-2}. Blue expresses stacking fault structure while yellow expresses irregular structure.

2.5 Conclusions

The MD simulations of displacement cascades in FCC metals under Poisson's deformation were performed using interatomic potentials differing only in SFE to elucidate the effects of strain on the SFE dependence of the defect formation process through cascade events. The results and insights obtained include:

- The value of N_F is independent of SFE, and applied strain does not change this independence. Meanwhile, the absolute value of N_F is increased by the applied strain to some extent, which is caused by a decrease in the formation energy of a Frenkel pair due to the volume increase under applied strain.
- Applied strain changes the size distribution of the produced SIA clusters: the formation of larger clusters is more enhanced under applied strain. This is because the formation energy of larger SIA clusters is lowered more significantly by applied strain.

Note that such a trend is observed over the whole SFE range employed in the present study.

- The number of SIA perfect loops is higher at lower SFE, which is observed over the whole SFE range. Furthermore, the trend is preserved under applied strain, and applied strain increases the absolute number of formed SIA perfect loops. This leads directly to the dependence in which the number of glissile SIA clusters increases with a decrease in SFE under no strain and applied strain. Based on the formation energy calculations for SIA clusters, it is found that the difference in the formation energy between an SIA perfect loop and an SIA Frank loop is a key factor for this trend.

The results obtained here indicate that, in lower SFE metals and at higher E_{PKA}, more glissile SIA clusters tend to form under irradiation. This is also supported by previous studies [46–48]. This leads to a more pronounced production bias of damage evolution through the one-dimensional transport of SIA perfect loops in materials. Considering the significant enhancement of the formation of glissile SIA clusters by the strain field, as observed in this study, it is essential to consider the strain field for modeling microstructural evolution through the cascade events.

References in Chapter 2

[1] ASTM E521, Standard practice for neutron radiation damage simulation by charged particle irradiation, Philadelphia: ASTM International: West Conshohocken, PA, 1996.

[2] R. E. Stoller, "Primary Radiation Damage Formation," in *Comprehensive Nuclear Materials*, Amsterdam, Elsevier, 2012, pp. 293–332.

[3] S. J. Zinkle, "Radiation-induced effects on microstructure," in *Comprehensive Nuclear Materials*, Amsterdam, Elsevier, 2012, pp. 65–98.

[4] J. D. Honeycutt and H. C. Andersen, "Molecular dynamics study of melting and freezing of small Lennard-Jones clusters," *Journal of Physical Chemistry*, vol. 91, pp. 4950–4963, 1987.

[5] D. Faken and H. Jonsson, "Systematic analysis of local atomic structure combined with 3D computer graphics," *Computational Materials Science*, vol. 2, pp. 279–286, 1994.

[6] Y. N. Osetsky, D. J. Bacon, A. Serra, B. N. Singh and S. I. Golubov, "Stability and mobility of defect clusters and dislocation loops in metals," *Journal of Nuclear Materials,* vol. 276, pp. 65–77, 2000.

[7] J. Silcox and P. B. Hirsch, "Direct observations of defects in quenched gold," *Philosophical Magazine,* vol. 4, pp. 72–89, 1959.

[8] M. L. Jenkins, "A weak-beam electron microscopy analysis of defect clusters in heavy-ion irradiated silver and copper," *Philosophical Magazine,* vol. 29, pp. 813–828, 1974.

[9] Y. Dai and M. Victoria, "Defect structures in deformed f.c.c. metals," *Acta Materialia,* vol. 45, pp. 3495–3501, 1997.

[10] S. J. Zinkle, "Microstructure and properties of copper alloys following 14-meV neutron irradiation," *Journal of Nuclear Materials,* vol. 150, pp. 140–158, 1987.

[11] B. N. Singh and S. J. Zinkle, "Defect accumulation in pure fcc metals in the transient regime: a review," *Journal of Nuclear Materials,* vol. 206, pp. 212–229, 1993.

[12] Y. Matsukawa and S. J. Zinkle, "One-dimensional fast migration of vacancy clusters in metals," *Science,* vol. 318, pp. 959–962, 2007.

[13] Y. N. Osetsky and D. J. Bacon, "Defect cluster formation in displacement cascades in copper," *Nuclear Instruments and Methods in Physics Research B,* vol. 180, pp. 85–90, 2001.

[14] K. Nordlund and F. Gao, "Formation of stacking fault tetrahedra in collision cascades,"

Applied Physics Letters, vol. 74, pp. 2720–2722, 1999.

[15] Y. N. Osetsky, A. Serra, M. Victoria, S. I. Golubov and V. Priego, "Vacancy loops and stacking-fault tetrahedra in copper," *Philosophical Magazine A,* vol. 79, pp. 2285–2311, 1999.

[16] M. Kiritani, "Observation and analysis of defect structure evolution from radiation damage by D-T fusion neutrons," *Journal of Nuclear Materials,* vol. 137, pp. 261–278, 1986.

[17] S. J. Zinkle and Y. Matsukawa, "Observation and analysis of defect cluster production and interactions with dislocations," *Journal of Nuclear Materials,* vol. 329–333, pp. 88–96, 2004.

[18] M. Kiritani, "Story of stacking fault tetrahedra," *Materials Chemistry and Physics,* vol. 50, pp. 133–138, 1997.

[19] J. L. Straalsund, R. W. Powell, B. A. Chin, *Journal of Nuclear Materials*, vol. 108–109, pp. 299–305, 1982.

[20] T. Okita, "Effects of dose rate on irradiation behavior in structural materials," Ph.D. thesis, Department of Quantum Engineering and Systems Science, School of Engineering, University of Tokyo, 2001.

[21] C. Cawthorne and E. J. Fulton, "Voids in irradiated stainless steel," *Nature*, vol. 216, pp. 575–576, 1967.

[22] F. A. Garner, "Recent insights on the swelling and creep of irradiated austenitic alloys," *Journal of Nuclear Materials*, vol. 122, pp. 459–471, 1984.

[23] F. A. Garner, M. B. Toloczko and B. H. Sencer, "Comparison of swelling and irradiation creep behavior of fcc-austenitic and bcc-ferritic/martensitic alloys at high neutron exposure," *Journal of Nuclear Materials*, vol. 276, pp.123–142, 2000.

[24] P. T. Heald, "The preferential trapping of interstitials at dislocations," *Philosophical Magazine A*, vol. 31, pp. 551–558, 1975.

[25] W. G. Wolfer, "The dislocation bias," *Journal of Computer-Aided Materials Design*, vol. 14, pp. 403–417, 2007.

[26] K. Doihara, T. Okita, M. Itakura, M. Aichi and K. Suzuki, "Atomic simulations to evaluate effects of stacking fault energy on interactions between edge dislocation and spherical void in face-centred cubic metals," *Philosophical Magazine*, vol. 98, pp.

2061–2076, 2018.

[27] L. K. Mansur, “Theory and experimental background on dimensional changes in irradiated alloys,” *Journal of Nuclear Materials*, vol. 216, pp. 97–123, 1994.

[28] M. L. Grossbeck, “Effect of radiation on strength and ductility of metals and alloys,” in *Comprehensive Nuclear Materials*, Amsterdam, Elsevier, 2012, pp. 99–122.

[29] B. N. Singh, A. J. E. Foreman and H. Trinkaus, “Radiation hardening revisited: role of intracascade clustering,” *Journal of Nuclear Materials*, vol. 249, pp. 103–115, 1997.

[30] C. Deo, C. Tome, R. Lebensohn and S. Maloy, “Modeling and simulation of irradiation hardening in structural ferritic steels for advanced nuclear reactors,” *Journal of Nuclear Materials*, vol. 377, pp. 136–140, 2008.

[31] S. J. Zinkle and G. S. Was, “Materials challenges in nuclear energy,” *Acta Materialia*, vol. 61, pp. 735–758, 2013.

[32] D. J. Bacon, F. Gao and Y. N. Osetaky, “The primary damage state in fcc, bcc and hcp metals as seen in molecular dynamics simulations,” *Journal of Nuclear Materials,* vol. 276, pp. 1–12, 2000.

[33] R. E. Voskoboinikov, Y. N. Osetsky and D. J. Bacon, “Computer simulation of primary damage creation in displacement cascades in copper. I. Defect creation and cluster statistics,” *Journal of Nuclear Materials,* vol. 377, pp. 385–395, 2008.

[34] Y. N. Osetsky, D. J. Bacon, B. N. Singh and B. D. Wirth, “Atomistic study of the generation, interaction, accumulation and annihilation of cascade-induced defect clusters,” *Journal of Nuclear Materials,* vol. 307–311, pp. 852–861, 2002.

[35] A. J. Foreman, W. J. Phythian and C. A. English, “The molecular dynamics simulation of irradiation damage cascades in copper using a many-body potential,” *Philosophical Magazine A,* vol. 66, pp. 671–695, 1992.

[36] W. J. Phythian, R. E. Stoller, A. J. Foreman, A. F. Calder and D. J. Bacon, “A comparison of displacement cascades in copper and iron by molecular-dynamics and its application to microstructural evolution,” *Journal of Nuclear Materials,* vol. 223, pp. 245–261, 1995.

[37] K. Nordlund, S. J. Zinkle, A. E. Sand, F. Granberg, R. Averback, R. E. Stoller, T. Suzudo, L. Malerba, F. Banhart, W. J. Weber, F. Willaime, S. L. Dudarev and D. Simeone, “Primary radiation damage: A review of current understanding and models,” *Journal of*

Nuclear Materials, vol. 512, pp. 450–479, 2018.

[38] F. Gao, D. J. Bacon, P. E. Flewitt and T. A. Lewis, "The influence of strain on defect generation by displacement cascades in a-iron," *Nuclear Instruments and Methods in Physics Research B,* vol. 180, pp. 187–193, 2001.

[39] B. Beeler, M. Asta, P. Hosemann and N. Gronbech-Jensen, "Effects of applied strain on radiation damage generation in body-centered cubic iron," *Journal of Nuclear Materials,* vol. 459, pp. 159–165, 2015.

[40] D. Wang, N. Gao, Z.G. Wang, X. Gao, W. H. He, M. H. Cui, L. L. Pang and Y. B. Zhu, "Effect of strain field on displacement cascade in tungsten studied by molecular dynamics simulation," *Nuclear Instruments and Methods in Physics Research B,* vol. 384, pp. 68–75, 2016.

[41] S. Di, Z. Yao, M. R. Daymond and F. Gao, "Molecular dynamics simulations of irradiation cascades in alpha-zirconium under macroscopic strain," *Nuclear Instruments and Methods in Physics Research B,* vol. 303, pp. 95–99, 2013.

[42] S. Di, Z. Yao, M. R. Daymond, X. Zu, S. Peng and F. Gao, "Dislocation-accelerated void formation under irradiation in zirconium," *Acta Materialia,* vol. 82, pp. 94–99, 2015.

[43] Q. Sahi and Y. Kim, "Molecular dynamics simulations of the coupled effects of strain and temperature on displacement cascades in a-zirconium," *Nuclear Engineering and Technology,* vol. 50, pp. 907–914, 2018.

[44] S. Miyashiro, S. Fujita and T. Okita, "MD simulations to evaluate the influence of applied normal stress or deformation on defect production rate and size distribution of clusters in cascade process for pure Cu," *Journal of Nuclear Materials,* vol. 415, pp. 1–4, 2011.

[45] S. Miyashiro, S. Fujita, T. Okita and H. Okuda, "MD simulations to evaluate effects of applied tensile strain on irradiation-induced defect production at various PKA energies," *Fusion Engineering and Design,* vol. 87, pp. 1352–1355, 2012.

[46] T. Okita, Y. Yang, J. Hirabayashi, M. Itakura and K. Suzuki, "Effects of stacking fault energy on defect formation process in face-centered cubic metals," *Philosophical Magazine,* vol. 96, pp. 1579–1597, 2016.

[47] Y. Yang, T. Okita, M. Itakura, T. Kawabata and K. Suzuki, "Influence of stacking fault

energies on the size distribution and character of defect clusters formed by collision cascades in face-centered cubic metals," *Nuclear Materials and Energy,* vol. 9, pp. 587–591, 2016.

[48] D. Nakanishi, T. Kawabata, K. Doihara, T. Okita, M. Itakura and K. Suzuki, "Effects of stacking fault energies on formation of irradiation-induced defects at various temperatures in face-centered cubic metals," *Philosophical Magazine,* vol. 98, pp. 3034–3047, 2018.

[49] D. Hull and D. J. Bacon, *Introduction to Dislocations,* Oxford: Pergamon, 1984.

[50] C. H. Woo and B. N. Singh, "Production bias due to clustering of point defects in irradiation induced cascades," *Philosophical Magazine A,* vol. 65, p. 889–912, 1992.

[51] C. H. Woo and B. H. Singh, "The concept of production bias and its possible role in defect accumulation under cascade damage conditions," *Physica Status Solidi,* vol. 159, pp. 609–616, 1999.

[52] B. N. Singh, M. Eldrup, A. Horsewell, P. Ehrhart and H. Dworschak, "On recoil energy dependent void swelling in pure copper," *Philosophical Magazine A,* vol. 80, pp. 2629–2650, 2000.

[53] S. I. Golubov, B. N. Singh and H. Trinkaus, "On recoil-energy-dependent defect accumulation in pure copper. Part II. Theoretical treatment," *Philosophical Magazine A,* vol. 81, pp. 2533–2552, 2001.

[54] C. C. Bampton, I. P. Jones and M. H. Loretto, "Stacking fault energy measurements in some austenitic stainless steels," *Acta Metall,* vol. 26, pp. 39–51, 1978.

[55] S. Plimpton, "Fast parallel algorithms for short-range molecular dynamics," *Journal of Computational Physics,* vol. 117, pp. 1–19, 1995.

[56] V. Borovikov, M. I. Mendelev, A. H. King and R. Lesar, "Effect of stacking fault energy on mechanism of plastic deformation in nanotwined FCC metals," *Modelling and Simulation in Materials Sciencen and Engineering,* vol. 23, pp. 055003-1–055003-16, 2015.

[57] M. I. Mendelev and A. H. King, "The interactions of self-interstitials with twin boundaries," *Philosophical Magazine,* vol. 93, pp. 1268–2178, 2013.

[58] J. F. Ziegler, J. P. Biersack and U. Littmark, "The stopping and range of irons in solids," New York: Pergamon, 1985.

[59] S. M. Rassoulinejad-Mousavi, Y. Mao and Y. Zhang, "Evaluation of copper, aluminum, and nickel interatomic potentials on predicting the elastic properties," *Journal of Applied Physics,* vol. 119, pp. 244304-1–244304-14, 2016.

[60] R. E. Stoller, G. R. Odette and B. D. Wirth, "Primary damage formation in bcc iron," *Journal of Nuclear Materials,* vol. 251, pp. 49–60, 1997.

[61] Y. N. Osetsky, D. J. Bacon, A. Serra, B. N. Singh and S. I. Golubov, "One-dimensional atomic transport by clusters of self-interstitial atoms in iron and copper," *Philosophical Magazine,* vol. 83, pp. 61–91, 2003.

[62] A. Stukowski and K. Albe, "Extracting dislocations and non-dislocation crystal defects from atomistic simulation data," *Modelling and Simulation in Materials Science and Engineering,* vol. 18, pp. 085001-1–085001-13, 2010.

[63] A. Stukowski, V. V. Bulatov and A. Arsenlis, "Automated identification and indexing of dislocations in crystal interfaces," *Modelling and Simulation in Materials Science and Engineering,* vol. 20, pp. 085007-1–085007-16, 2012.

[64] M. Kiritani and H. Takata, "Dynamic studies of defect mobility using high voltage electron microscopy," *Journal of Nuclear Materials,* vol. 69–70, pp. 277–309, 1978.

[65] M. Suzuki, A. Sato, T. Mori, J. Nagasawa, N. Yamamoto and H. Shiraishi, "In-situ deformation and unfaulting of interstitial loops in proton-irradiated steels," *Philosophical Magazine A,* vol. 65, pp. 1309–1326, 1992.

[66] L. Boulanger, F. Soisson and Y. Serruys, "Interaction between the deformation and the irradiation defect clusters in austenitic steels," *Journal of Nuclear Materials,* vol. 233, pp. 1004–1008, 1996.

[67] B. D. Wirth, V. Bulatov and T. Diaz de la Rubia, "Atomistic simulation of stacking fault tetrahedra formation in Cu," *Journal of Nuclear Materials,* vol. 283–287, pp. 773–777, 2000.

[68] T. Kadoyoshi, H. Kaburaki, F. Shimizu, H. Kimizuka, S. Jitsukawa and J. Li, "Molecular dynamics study on the formation of stacking fault tetrahedra and unfaulting of Frank loops in fcc metals," *Acta Materialia,* vol. 55, pp. 3073–3080, 2007.

[69] M. J. Nogarett, M. T. Robinson and I. M. Torrens, "A proposed method of calculating displacement cdose rates," *Nuclear Engineering and Design,* vol. 33, pp. 50–54, 1975.

[70] I. M. Torrens and M. T. Robinson, in *Radiation-Induced Voids in Metals*, *Proceedings*

of the 1971 International Conference Held at Albany, pp. 739–756, 1972.

[71] M. T. Robinson, "Basic physics of radiation damage production," *Journal of Nuclear Materials*, vol. 216, pp. 1–28, 1994.

[72] Y. N. Osetsky, A. Serra, B. N. Singh and S. I. Golubov, "Structure and properties of clusters of self-interstitial atoms in fcc copper and bcc iron," *Philosophical Magazine A,* vol. 80, pp. 2131–2157, 2000.

Chapter 3 Acceleration schemes for self-evolving atomistic kinetic Monte Carlo

3.1 Motivation and background

In Chapter 2, the defect formation process through displacement cascades was evaluated using MD simulations, with a focus on its dependence on SFE. An interesting finding was that the number of produced SIA perfect loops increased with a decrease in SFE, resulting in a larger number of glissile SIA clusters at lower SFE. Note also that the applied strain enhanced the formation of glissile SIA clusters. It has been known that the subsequent microstructural evolution is considerably affected by the behavior of glissile SIA clusters; the one-dimensional transport of SIA clusters triggers the production bias of damage evolution [1,2]. Therefore, the extracted insights from the study are quite important for modeling the microstructural evolution under irradiation. Meanwhile, as shown in Figures 2.13 and 2.14, some of the SIA clusters produced through displacement cascades had an irregularly shaped configuration (Figure 3.1). In particular, more than half of the SIA clusters produced were irregularly shaped under no strain at Γ_{SFE} = 186.5 mJ m^{-2}. As such irregular shapes are energetically unfavorable, these clusters were supposed to transform into stable configurations after a certain period through multiple diffusion events of atoms composing the cluster (core diffusion). However, as typical diffusion events require relatively high E_a and are beyond the scope of the MD timescale, the clusters remained energetically unstable configurations in the MD simulations. Consequently, the number of such irregularly shaped SIA clusters influenced the overall ratio of glissile SIA clusters, implying that, whichever configurations the irregularly shaped SIA clusters would resultantly transform into (Frank loop or perfect loop) could change the conclusion drawn in Chapter 2. In order to clarify this, it is necessary to investigate the resultant stable configuration of irregularly shaped clusters beyond the MD timescale. Furthermore, as shown in Figure 3.1, the produced SIA clusters have quite complex structures, which would also render the transformation process quite complex. Thus, the meso-timescale simulations that maintain atomistic fidelity are necessary for the investigation.

Figure 3.1 Irregularly shaped SIA clusters produced through the cascade simulations in Chapter 2. The figure has been reproduced from Figure 2.6.

A powerful tool for meso-timescale atomistic simulations is the on-the-fly kMC [3]. Its characteristic is on-the-fly construction of the event list at each step, which enables the simulation of complex phenomena that are unpredictable beforehand. In addition, on-the-fly kMC introduces the concept of state-to-state dynamics and follows the resident time algorithm for the time evolution of the simulation, as conventional kMC does [4,5]. Thus, on-the-fly kMC can reach the timescale far beyond that of MD while maintaining atomistic fidelity. However, the procedure for searching the possible events is usually very time-consuming. To address this issue, each on-the-fly kMC technique has its own unique algorithm. For instance, adaptive kMC recycles the information on the searched events for building the next-step event list instead of launching the event searches from scratch [6]. Self-learning kMC constructs a database for the obtained reaction path and its corresponding energy barriers for future usage [7,8]. The kinetic activation-relaxation technique introduces the concept of topology for identifying system configuration, where event searches for topologies that are already visited during previous steps are performed by recycling and refining the event list obtained at that step [9,10]. While these techniques efficiently search for possible events by using the information obtained at previous steps, they tend to be time-consuming for newly visited configurations, which renders it difficult to handle a large system. SEAKMC, on the other hand, uses a different approach—it introduces the concept of AV, where the dynamic process of interest may occur [11–14]. The SPs corresponding to the possible events are searched only within the AVs, not in the whole system, and all atoms outside the AV are frozen during the search. This considerably reduces the degrees of freedom for the search, leading to fast convergence to the SP and significant acceleration, even if the configuration is visited for the first time. Because of this benefit, SEAKMC has also been applied to relatively large systems with 128,000 atoms [15]. However, note also that the calculation cost increases drastically with the AV size, as seen in Figure 3.2, where the

dependence of computation time for an SPS on the AV size for iron bulk diffusion of an SIA is shown. Hence, treating relatively large defect clusters with SEAKMC is quite challenging, although they play an important role in microstructural evolutions. This demonstrates the necessity for finding additional acceleration techniques for SEAKMC to broaden its application to various practical problems. In addition, unlike adaptive kMC, self-learning kMC, and kinetic activation-relaxation technique, SEAKMC does not recycle the SP information for future searches. This could cause numerous redundant convergences to duplicate SPs throughout the simulation, resulting in a significant decrease in calculation efficiency, particularly in a system that contains symmetric defects, such as point defects or defect clusters.

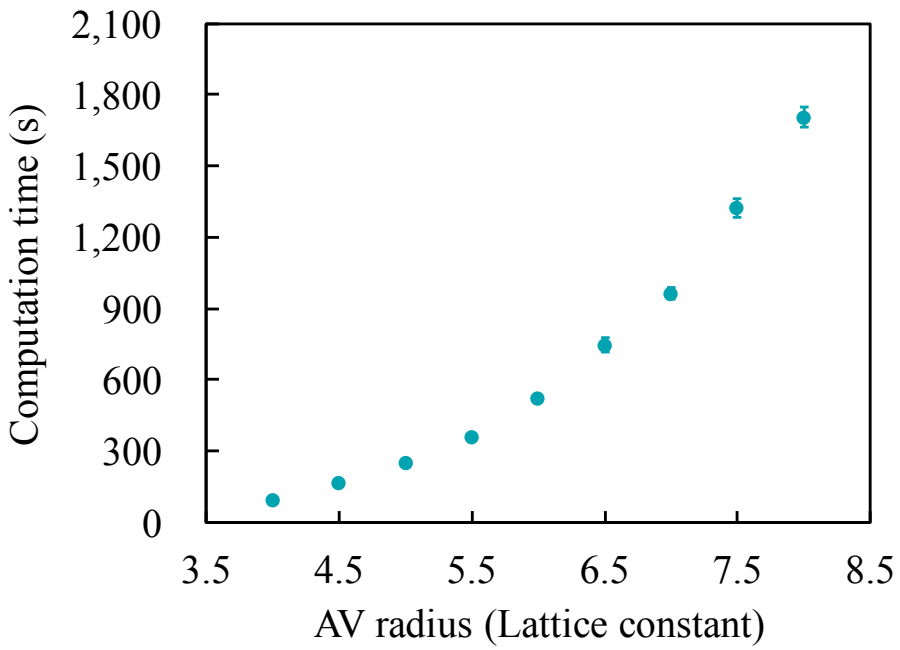

Figure 3.2 Dependence of computation time for SPS on AV size in case of an SIA bulk diffusion, where a spherical AV is employed. The calculations are conducted using a single core on E5-2690 Intel Xeon CPU at 2.90 GHz. The error bars represent the standard error over 10 samples.

In this chapter, we propose acceleration schemes for SEAKMC with the purpose of improving its capability and broadening its applicability, and demonstrate an application of the accelerated SEAKMC to the meso-timescale dynamics of an irradiation-induced defect

cluster in FCC metals. In the first part, two acceleration schemes that significantly speed up the original SEAKMC, are elaborated. The first is the multi-step procedure of SPS, where a relatively small AV is initially used for obtaining a rough estimate of the SP configuration, followed by searches with sufficiently large AVs for obtaining more accurate configurations. Here, the SP information obtained by the SPS with a smaller AV is used as the prediction of that with a larger AV. The second is the recycling of previously found SP configurations for future searches. To benchmark these schemes, the bulk diffusion of an SIA and a vacancy in iron is simulated using the accelerated SEAKMC, and its efficiency and fidelity are discussed in detail. Furthermore, a hybrid SPS framework, which couples the two acceleration schemes, is proposed, which achieves further acceleration of the calculations. The analysis of the diffusivity of an SIA cluster is presented to demonstrate the fidelity of the hybrid SPS framework. In the second part of this chapter, the accelerated SEAKMC is applied to investigate the meso-timescale evolution of an irregularly shaped sessile SIA cluster produced through the MD cascade simulations in Chapter 2. The transformation process of the clusters is discussed in detail, with an estimation of the time required for the transformation.

3.2 Acceleration scheme for SEAKMC

3.2.1 Overview of the original SEAKMC

First, an overview of the original SEAKMC method is briefly provided. A flowchart of the SEAKMC algorithm is depicted in Figure 3.3 [11]. At each step, the AVs are first characterized based on a certain criterion, such as comparisons of atomic positions with reference sites or checking the energy or stress deviations from the value of a perfect lattice. In the present study, we introduce spherical AVs with radius r_{AV}, centered around each SIA and vacancy, which are identified with Wigner–Seitz defect analysis. If the identified defects compose a cluster, resulting in the overlap of AV regions with those of the neighboring defects, we combine the regions and treat them as one AV (Figure 3.4). This procedure ensures the AV shape exactly follows the defect configuration, which leads to a more efficient AV shape than just setting one spherical AV to each cluster. This is effective, particularly for nonspherical defects such as dislocation loops. Note that r_{AV} should be sufficiently large such that physically correct dynamic processes are sampled through the SPS in the AV.

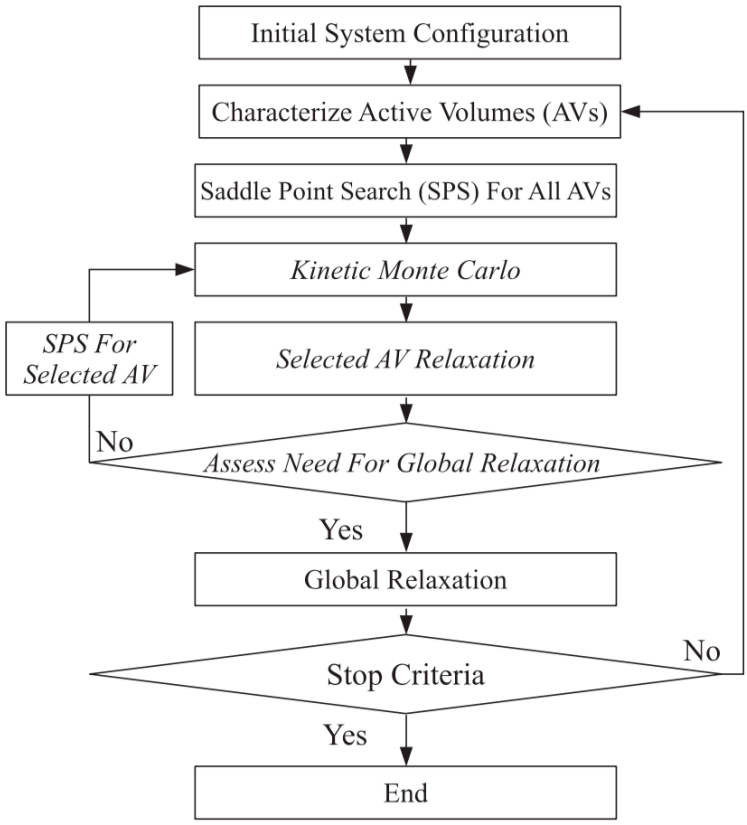

Figure 3.3 Flowchart of the original SEAKMC algorithm [11].

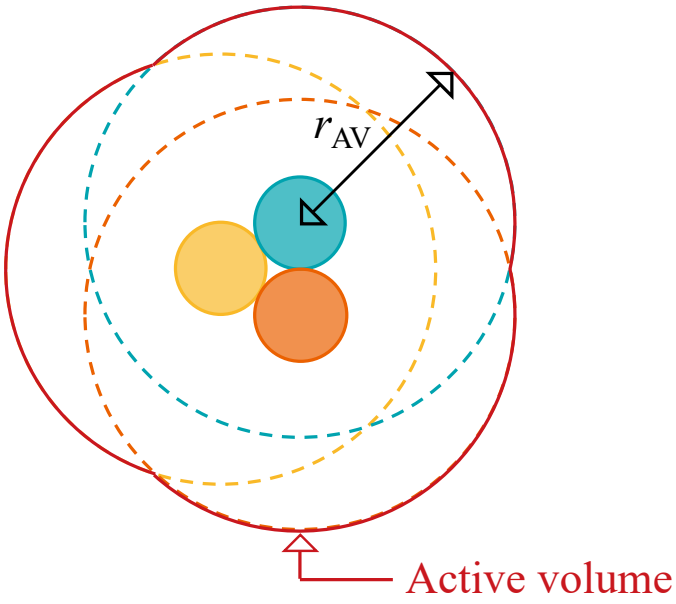

Figure 3.4 Schematic explanation of the manner of characterizing an AV when several AV regions overlap.

After characterizing AVs, the SPSs are launched in the AVs for building the kMC event list; the dimer method [16,17] is implemented in SEAKMC. Note that an atomic structure and an interatomic potential are the only required material inputs for this method. During the search, atoms outside the AV are frozen, which significantly reduces the number of necessary force calculations and limits the degrees of freedom of the system. The efficiency obtained owing to the introduction of AVs becomes more apparent as the system size increases. This is because only a few hundred/thousand atoms are active during the search, although the whole system contains a vast number of atoms. There are usually numerous SPs around a given initial state; therefore, multiple SPSs should be launched with different sets of random displacements from the state for obtaining as many SPs as possible. Duplicate SPs are usually found through multiple SPSs, and adding all of them to the event list leads to inaccuracy in simulated time. To avoid this, we conduct a duplication check every time a new SP is found in this study—if all atoms in the newly found SP configuration have a single corresponding atom in either of the already found SP configuration with a tolerance of 0.2 Å, we define them as identical SPs and add only one of them to the event list. Note that this procedure requires additional computational cost; however, the time required for SPSs is a bottleneck for SEAKMC and the duplication check would impose little delay of the simulation.

From the event list composed of sampled SPs and their corresponding *E*a, the occurring event is randomly chosen and the system clock is advanced using the residence time algorithm [4,5]. Static relaxation is then performed in the AV where the event occurs, such that the internal configuration is pushed over the chosen SP and relaxed to another local minimum state. Note that when the AVs in the system are sufficiently distant from each other, the SPS at the next step is only performed in the AV where the event occurs at the current step, because the configurations in the remaining AVs remain unchanged through the event. If it becomes necessary to re-determine the AV boundary (for example, the energy deviations at the boundary becomes larger than a certain threshold), the AVs are re-characterized, possibly leading to the merger of multiple AVs.

3.2.2 Acceleration scheme I: Multi-step procedure of SPS with increasing AV size

In this scheme, we begin an SPS with a relatively small r_{AV}. Although the SP configuration and corresponding E_{a} obtained at this stage usually contain some errors (the

value of E_a tends to be higher due to too few degrees of freedom), they are considered to be close to the ones with desired accuracy. For instance, when employing $r_{AV} = 2.8a_0$ and $4.2a_0$ for evaluating E_a of SIA bulk diffusion in iron (a_0: lattice constant), the obtained E_a values are ~0.31 and ~0.32 eV, respectively, indicating that the difference in E_a is as low as ~0.1 eV, although the AV with $r_{AV} = 4.2a_0$ is 1.5 times larger than that with $r_{AV} = 2.4a_0$. Based on this, we use the SP configuration obtained with the small r_{AV} as a "prediction" for SPSs with larger r_{AV}: after the SPS with a small r_{AV}, we launch the search again with a larger r_{AV} where the SP configuration obtained with the small r_{AV} is used as the initial AV configuration. The SPS based on the prediction is repeated while increasing the r_{AV} until the configuration and E_a with desired accuracies are obtained. This procedure significantly improves the efficiency of SPS because of two factors: (i) the number of interatomic force calculations, which dominates the calculation cost of the search, is considerably reduced, and (ii) the degree of freedom is significantly limited, leading to efficient convergence to the SP. Note that the use of a small r_{AV} has the inherent risk of overlooking some transition paths; therefore, special attention should be paid to the application of the technique, e.g., checking the sensitivity of dynamic processes to the initially introduced $r_{AV,}$ or rendering the AV shape to exactly follow the defect configuration so that the AV boundary is sufficiently distant from each atom constituting the defect cluster, as done in this study.

The gradual changes in E_a with increasing r_{AV} are shown in Figure 3.5. Here, we consider bulk diffusion in iron of an SIA and a vacancy, with an interatomic potential developed by Ackland et al. [18]. In both cases, with increasing r_{AV}, E_a converges to a certain value; the values are 0.31 eV for $r_{AV} = 4.2a_0$ and 0.63 eV for $r_{AV} = 3.6a_0$, for the SIA and vacancy diffusions, respectively. The values agree very well with those obtained by the original SEAKMC (~0.30 eV in the case of an SIA and ~0.63 eV in the case of a vacancy) [12]. We also examine the sensitivity of E_a to step size for increasing r_{AV} (Δr_{AV}), as shown in Figures 3.6–3.11. We find that changing Δr_{AV} causes no change in the converged value in both cases.

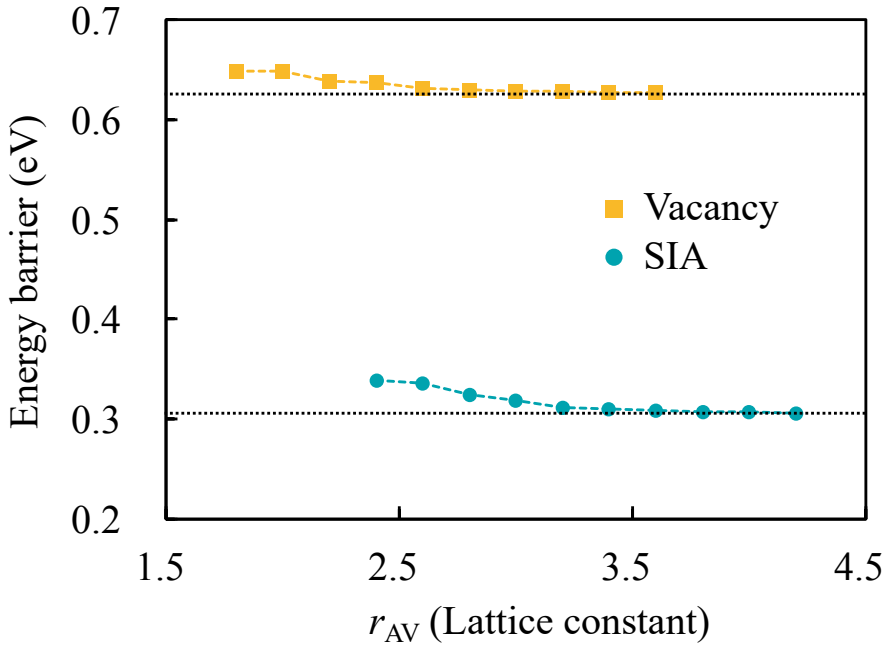

Figure 3.5 Gradual changes in E_a with increasing r_{AV} in the case of an SIA and a vacancy bulk diffusion in iron. The values of r_{AV} are changed from $2.4a_0$ to $4.2a_0$ and from $1.8a_0$ to $3.6a_0$ in steps of $0.2a_0$ for the SIA and the vacancy case, respectively.

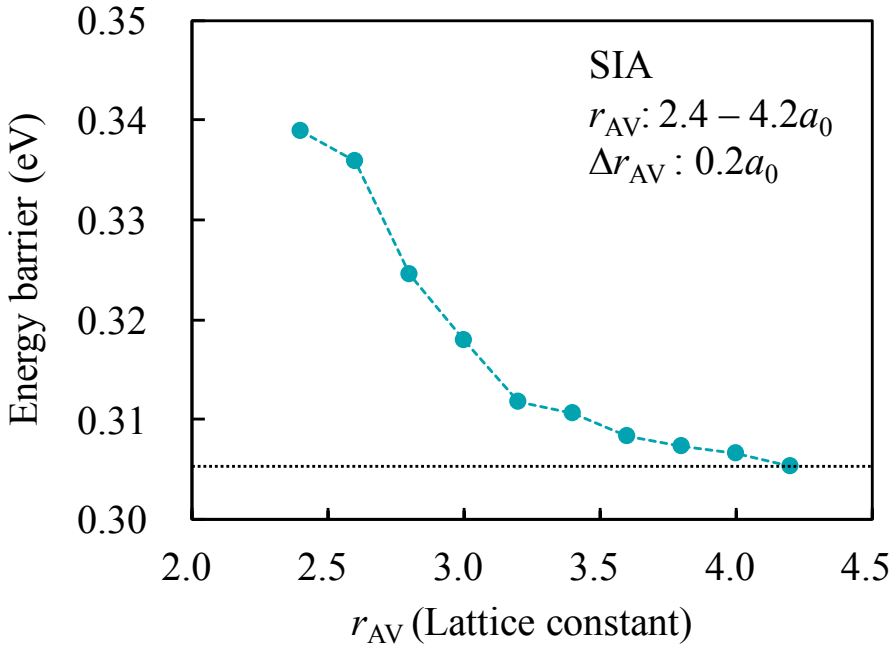

Figure 3.6 Converged E_a for SIA bulk diffusion when r_{AV} changes from $2.4a_0$ to $4.2a_0$ in steps of $0.2a_0$.

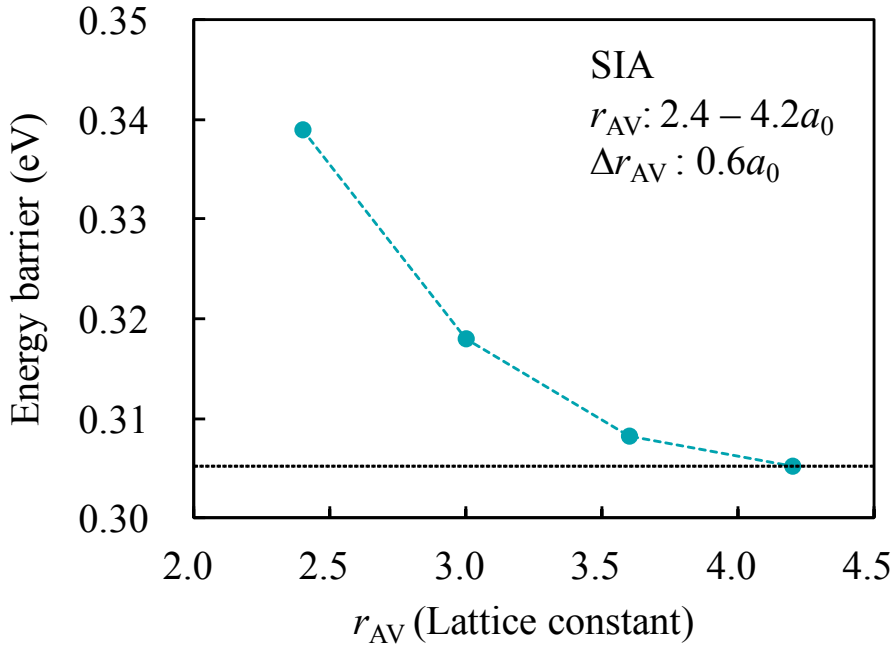

Figure 3.7 Converged E_a for SIA bulk diffusion when r_{AV} changes from 2.4a_0 to 4.2 a_0 in steps of 0.6a_0.

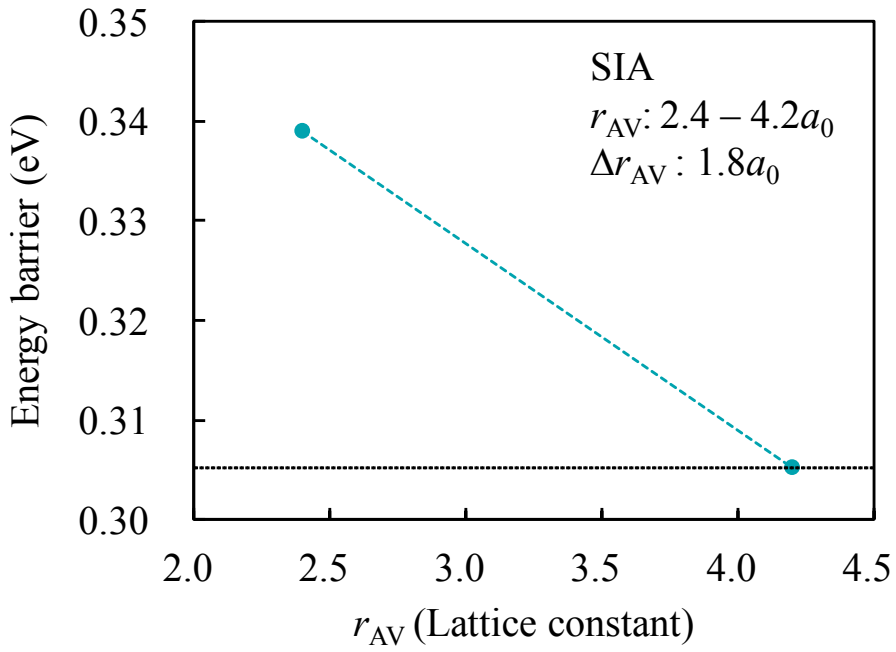

Figure 3.8 Converged E_a for SIA bulk diffusion when r_{AV} changes from 2.4a_0 to 4.2a_0 in steps of 1.8a_0.

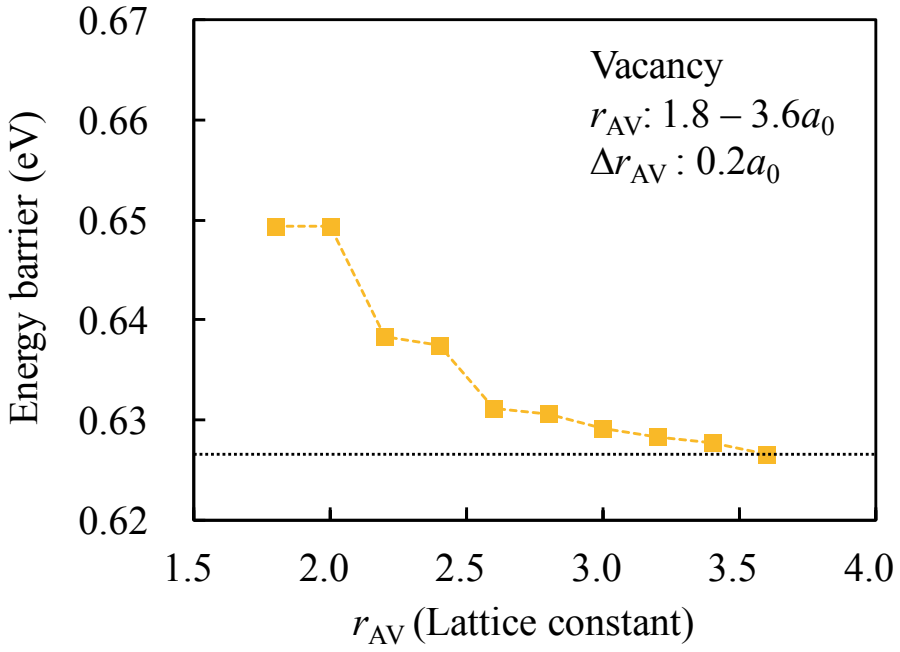

Figure 3.9 Converged E_a for vacancy bulk diffusion when r_{AV} changes from 1.8a_0 to 3.6a_0 in steps of 0.2a_0.

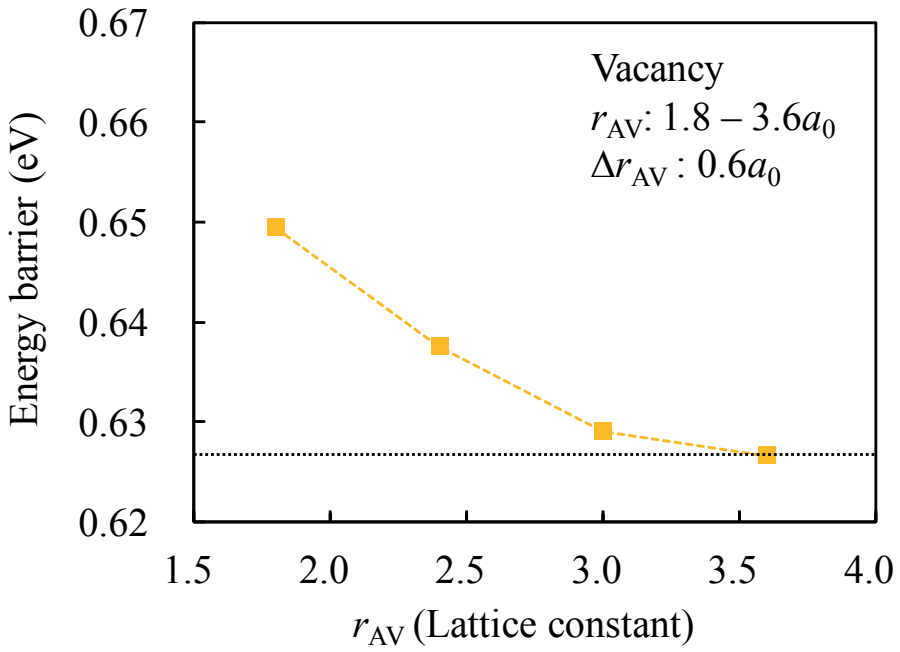

Figure 3.10 Converged E_a for vacancy bulk diffusion when r_{AV} changes from 1.8a_0 to 3.6a_0 in steps of 0.6a_0.

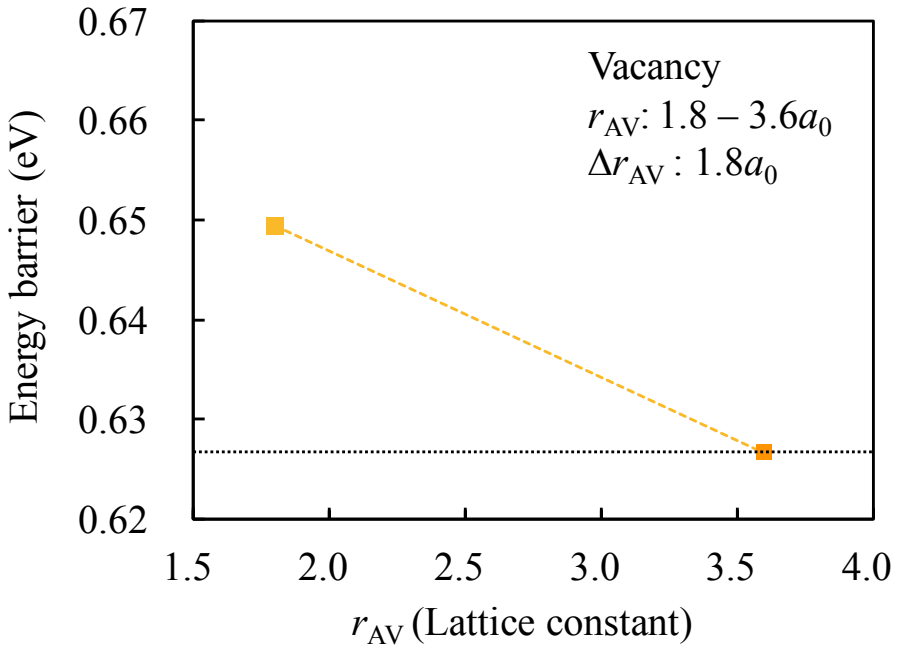

Figure 3.11 Converged E_a for vacancy bulk diffusion when r_{AV} changes from 1.8a_0 to 3.6a_0 in steps of 1.8a_0.

On the other hand, the efficiency of SPS with increasing r_{AV} varies for different Δr_{AV}. The computation time for finding the SP with different values of Δr_{AV} is shown in Figures 3.12 and 3.13. Note that the time is normalized by that obtained without increasing the r_{AV}. This clearly shows that the efficiency is enhanced as Δr_{AV} increases; the two-step increasing r_{AV}, namely the case where a sufficiently large r_{AV} is employed just after the initial one (Δr_{AV} = 1.8a_0), has the highest efficiency. As shown in Figures 3.6–3.11, the difference in E_a between the largest and smallest r_{AV} cases is only of the order of 0.01 eV, indicating that the SP configuration even at the smallest r_{AV} is almost accurate enough to easily converge to the desired SP at the largest r_{AV}. The ease of convergence at the largest r_{AV} is also seen in Figure 3.14, which shows the breakdown of the whole computation time in the case of SIA diffusion with Δr_{AV} = 1.8a_0, i.e., the ratio of computation time for SPS with r_{AV} = 2.4a_0 and 4.2a_0. As shown in the figure, the computation time with r_{AV} = 4.2a_0 is much shorter than that with r_{AV} = 2.4a_0, although the AV with r_{AV} = 4.2a_0 contains a much larger number of atoms. The SPS in the acceleration scheme presented here requires a convergence process to the SP for each AV size, i.e., every time the AV size increases, it is necessary to re-converge to the SP that corresponds to that AV size. This inevitably leads to a higher calculation cost. Note that,

because of this, just increasing the number of employed r_{AV} does not provide any advantage, and instead can considerably reduce the efficiency.

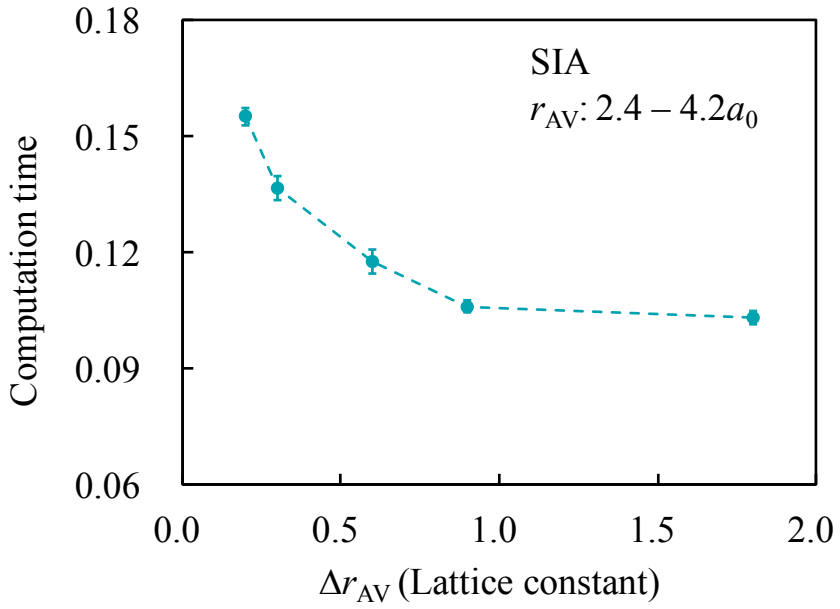

Figure 3.12 Comparison of computation time for finding the SP of the SIA bulk diffusion between different values of Δr_{AV}. The error bars represent the standard error over 10 samples.

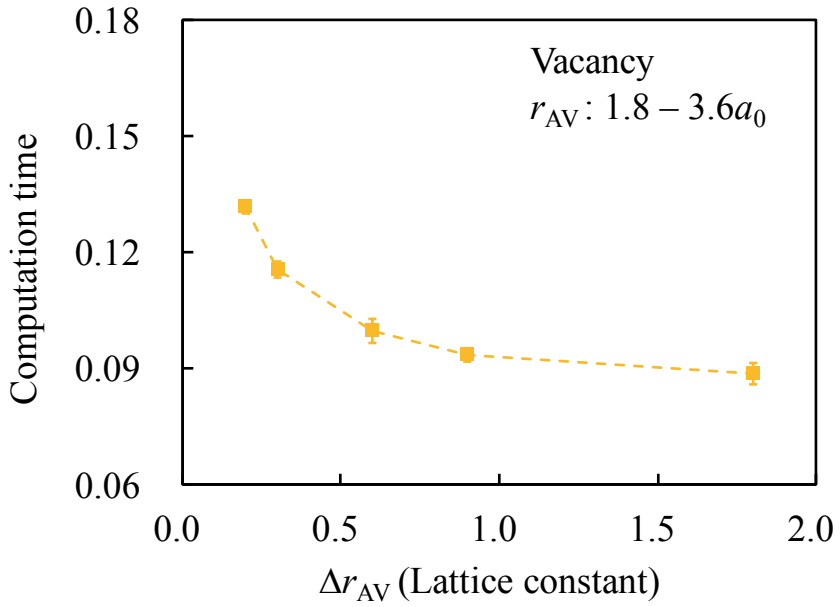

Figure 3.13 Comparison of computation time for finding the SP of the vacancy bulk diffusion between different values of Δr_{AV}. The error bars represent the standard error over 10 samples.

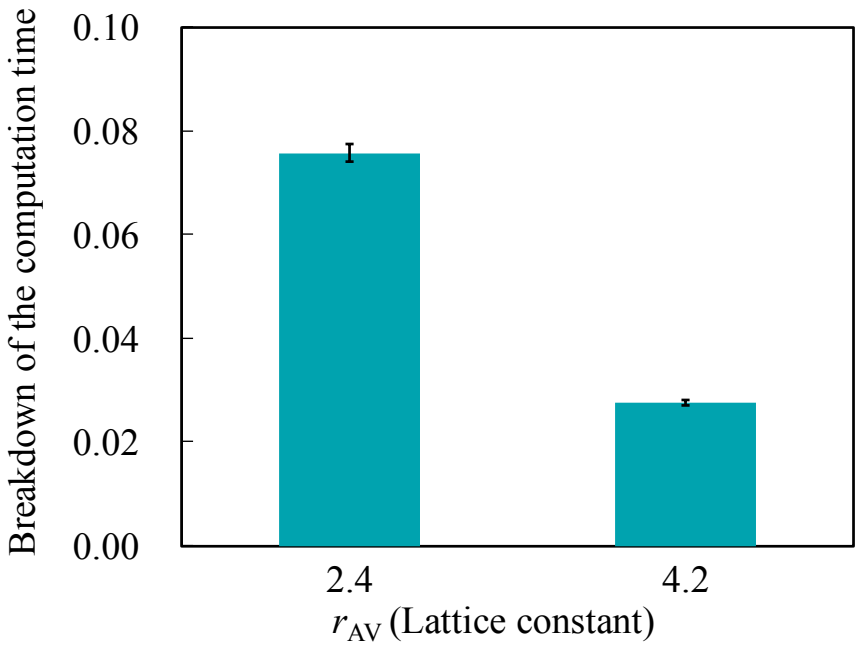

Figure 3.14 Breakdown of the whole computation time for an SPS for SIA bulk diffusion when a two-step evolving AV is employed: $r_{AV} = 2.4a_0$ and $4.2a_0$. The error bars represent the standard error over 10 samples.

3.2.3 Acceleration scheme II: Recycling of previous SP information for future searches

During the simulation, we often observe an AV configuration very similar to that of the previously visited configurations, especially when the AV contains a symmetrically structured defect. Correspondingly, a similar energy landscape is also obtained through the SPS in this case, motivating us to recycle the previous SP configurations as the prediction for the current SPS. The recycling procedure is performed as follows. We store AV configurations and corresponding SP configurations sampled during SPSs, and at each step, we check whether it is possible to identify the current AV configuration with either of the stored ones before conducting SPS. If possible, the current-step SPSs are started from the SP configurations associated with the identified AV; if not, recycling is not performed and the current-step SPSs are started from scratch, followed by storing the sampled SP configurations being associated with the current AV configuration. The identification criterion should be sufficiently strict so as not to identify physically unrelated AV configurations. We conduct an identification check of the current AV with each stored AV, and if each atom in the current

AV corresponds to a single atom in the stored AV with a tolerance of 0.2 Å, we assume, by definition, that the current and stored AVs are identical and employ SP recycling (Figure 3.15). Note that the previous SP configurations are used just for the prediction, and not directly employed as the current SP configurations. Because of this, the current AV configuration need not be exactly the same as the previous configuration, which considerably increases the number of applicable cases for stored configurations as predictions. For instance, considering SP configurations of the SIA bulk diffusion sampled under no strain field, they can also be used for diffusion in the presence of strain fields; as the SPS with the prediction proceeds, the configuration gradually incorporates the effect of the existing strain field, although it originally does not. In addition, the identification check is conducted only within the AV, not within the whole system; hence, only relative atomic environments around the defect affect the check, regardless of its absolute position in the system. Moreover, stored configurations can be used for other calculations, e.g., kMC repeated calculations or even under different conditions, such as different temperatures. These contribute to increasing employment of SP recycling and considerably reduce the necessary number of stored AV configuration patterns, leading to not only acceleration but also saving of computer memory.

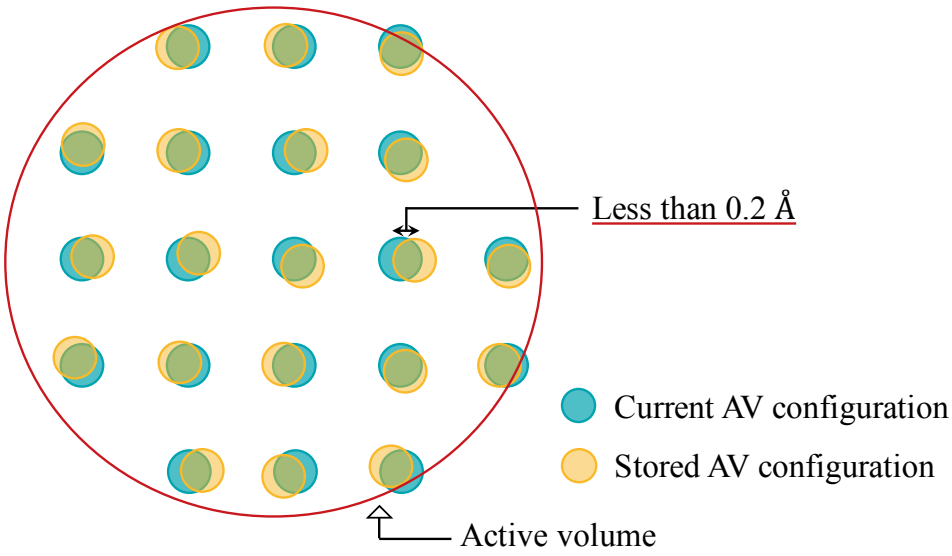

Figure 3.15 Schematic explanation of the manner of identification check between the current AV configuration and the stored one.

Figure 3.16 shows the computation time for an SPS with SP recycling. An SIA and a

vacancy bulk diffusion are used as the test cases, and the results are normalized by those without the recycling scheme. In both cases, the calculations are significantly accelerated; they are around 50–200 times faster than those without the recycling technique. Note that this acceleration is much more significant than that obtained by the multi-step procedure of SPS (see last subsection). In addition, we confirm that the obtained energy barriers are in excellent agreement with those with the original SEAKMC. These results demonstrate the notable power of the recycling technique while maintaining the fidelity.

Figure 3.16 Computation time for SPS with SP recycle in the case of SIA and vacancy bulk diffusion. The values of r_{AV} are $4.2a_0$ and $3.6a_0$ for the SIA and the vacancy diffusion case, respectively. The error bars represent the standard error.

3.2.4 Prediction-based SPS

In subsections 3.2.2 and 3.2.3, we describe the two acceleration schemes for SEAKMC, which, importantly, can coexist in one scheme (Figure 3.17). After the AV characterization, we check whether each AV configuration can be identified with either of the stored AV configurations. Depending on its result, we use different schemes: if identified, we use the stored SP configurations as SPS predictions, as described in subsection 3.2.3; otherwise, we

launch SPSs with smaller r_{AV} values to obtain the predictions for the SPSs with a sufficiently large r_{AV}, as described in subsection 3.2.2. In other words, we always generate SP predictions with either of the schemes depending on the current AV configuration, the SPS, which we refer to as the "prediction-based SPS." Furthermore, with an increase in the number of simulation steps, the number of stored AV configurations is increased, i.e., the probability of employing SP recycling increases. As the acceleration achieved by SP recycling is much more significant than that achieved by multi-step SPS, as mentioned above, the prediction-based SPS achieves increasing speed-up as the simulation proceeds. In addition, this scheme enables further saving of computer memory for storing SP configurations. As shown in Figure 3.14, the search converges to the SP quickly even with the larger r_{AV} once the SP prediction is obtained, indicating that storing and recycling the AV and SP configurations only of the smallest r_{AV} (= $2.4a_0$ in this case) will still afford sufficient efficiency. Note that the efficiencies and fidelities benchmarked above are valid in the hybrid scheme here because the two acceleration schemes never interfere with each other.

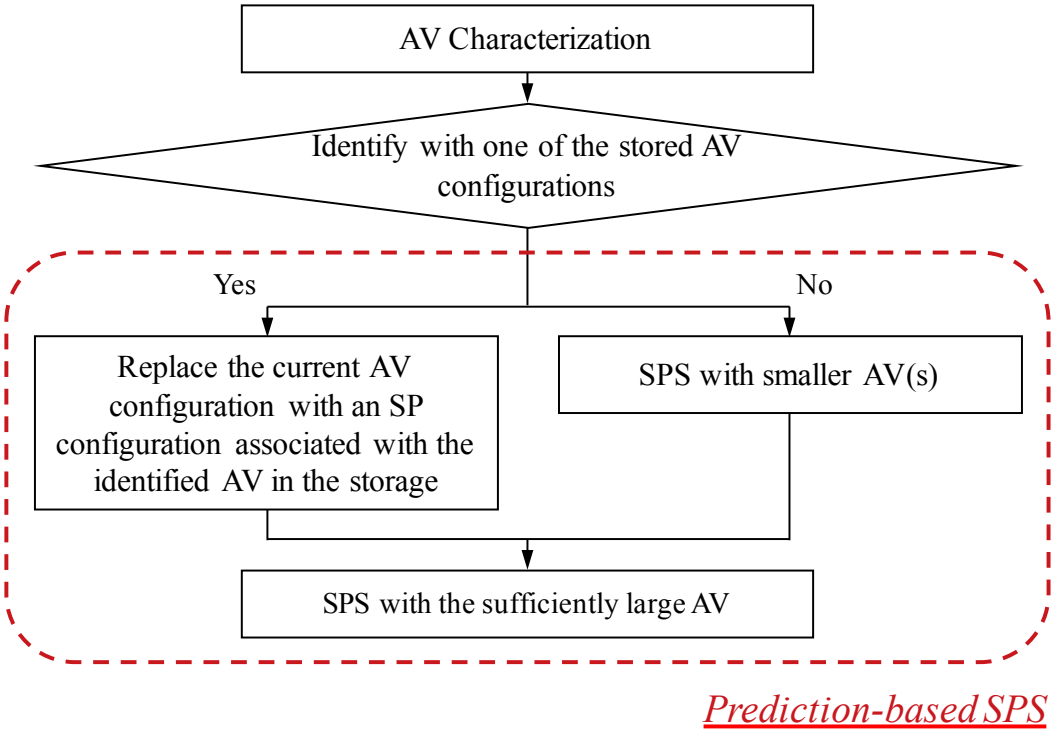

Figure 3.17 Flowchart of the prediction-based SPS.

3.3 Application of the accelerated SEAKMC to various problems

3.3.1 Diffusion of an SIA cluster in iron

Here, the diffusion dynamics of an SIA cluster are simulated using the accelerated SEAKMC, i.e., SEAKMC with the prediction-based SPS, for benchmarking it. We consider the diffusion of a three-SIA cluster in iron, which exhibits three-dimensional random diffusion in the bulk [19,20]. The axes of the simulation cell are set as $[1\ 1\ 1]$, $[1\ 1\ \bar{2}]$, and $[\bar{1}\ 1\ 0]$, and the dimensions of the cell are approximately 9.9, 9.8, and 10.5 nm in the x, y, and z directions, respectively. Periodic boundary conditions are applied in all directions and an interatomic potential developed by Ackland et al. is used to calculate the interatomic force [18]. The cluster is placed at the center of the cell and the system is then relaxed by the static method, generating the initial configuration for the simulations. During the simulations, the defect motion is tracked by analyzing the displacements of the center of the cluster mass, defining a cluster jump to occur when the center is displaced by $\sqrt{3}/2a_0$ (Δ). From the jump frequency (ν), the defect diffusivity (D_v^{d}) is estimated as,

$$D_v^{\mathrm{d}} = f_{\mathrm{C}} \frac{\nu \Delta^2}{6} \tag{2.4}$$

where f_{C} is the correlation factor of defect jumps estimated from the analysis of jump directions [21]. The temperature is varied from 250 to 500 K and over 1000 jumps are sampled under each condition to obtain statistically meaningful results. A constant attempt frequency is used for the kMC step (4.0×10^{12} s^{-1}). For the SPS, a two-step evolving AV is applied when there is no AV configuration identified in the storage. This is expected to realize the best calculation performance, as seen in subsection 3.2.2. One of the critical issues in performing SPS is the determination of the number of unique SPs that should be sampled at each step; the sufficiency of an event list can directly affect the fidelity of system dynamics and the accuracy in the simulated time, but finding all existing SPs around a given state is practically impossible for complex systems [12]. We use a self-consistent equation suggested in Ref. [12] as a criterion for stopping the SPS, which is based on the incremental change in the frequency of events (Δf) over a certain number of unique SPs (Δn). This is described as,

$$\delta = \frac{f_{\mathrm{n}}^{*}}{f_{\mathrm{total}}} \tag{2.5}$$

where $f_{\mathrm{n}}^{*} = \Delta f / \Delta n$ and f_{total} is the total frequency obtained from all unique SPs. In this study, the value of Δn is set as 20 and δ is evaluated every time a new unique SP is found. We stop the SPS when δ becomes less than 0.015 or the total number of SPSs increases to over 2000.

The D_v^{d} values for cluster diffusion as a function of temperature are shown in Figure 3.18, where r_{AV} of the initially introduced AV ($r_{\mathrm{AV}}^{\mathrm{ini}}$) and that of the following larger AV ($r_{\mathrm{AV}}^{\mathrm{fin}}$) are $2.7a_0$ and $4.5a_0$, respectively. From the plots, the effective activation energy for the diffusion can be evaluated using the Arrhenius law; the activation energy is 0.18 eV, which agrees well with the MD result (0.16 eV) [20]. This confirms that the criterion for stopping the SPS used here is quite reasonable for a sufficient number of unique SPs to be sampled, and that the accelerated SEAKMC describes the rate of defect diffusion with an accuracy comparable to that obtained by MD.

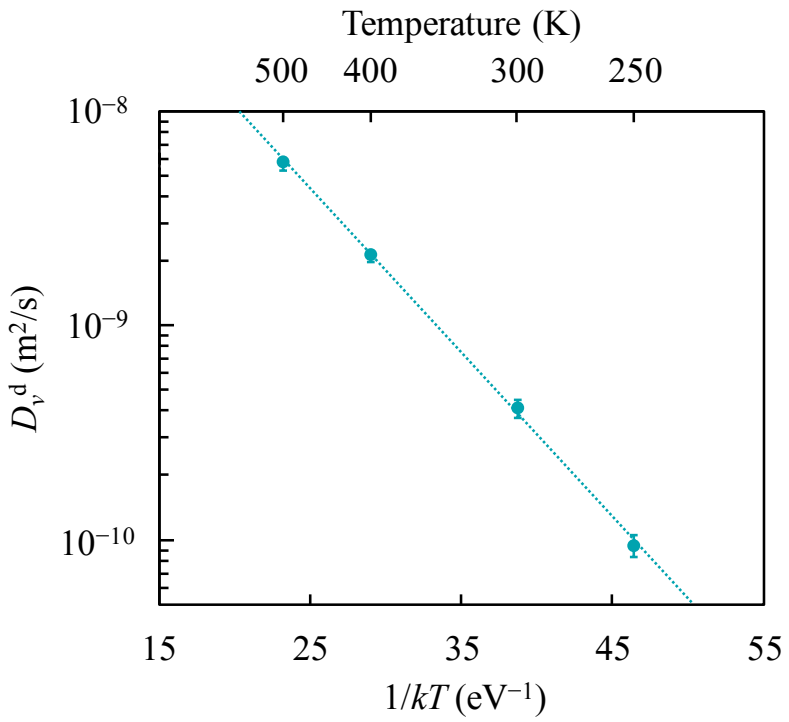

Figure 3.18 Values of $D_{\mathrm{v}}^{\mathrm{d}}$ as a function of temperature. The error bars represent twice the standard error of the mean. The letters k and T at the lower horizontal axis denote the Boltzmann constant and temperature, respectively.

The comparison of elapsed computation time for simulating the cluster diffusion between various r_{AV} is shown in Figure 3.19. The values of r_{AV}^{ini} and r_{AV}^{fin} are varied from $2.7a_0$ to $4.5a_0$ and from $4.5a_0$ to $6.3a_0$ in steps of $0.9a_0$, respectively. We also conduct the original SEAKMC simulations under the same condition, except for the value of r_{AV}, which is set as any of the three r_{AV}^{fin} values. It is clearly seen that the accelerated SEAKMC considerably accelerates the simulations. In addition, the computation time dependence on r_{AV} is quite different between the accelerated SEAKMC and the original SEAKMC; it is more apparent after several hundreds of simulation steps, where there is no significant difference in the slopes between the simulations with the accelerated SEAKMC, owing to the increasing employment of SP recycling. This indicates that, while it may take some time at the beginning to collect AV configurations and corresponding SP information for storage, once they are sufficiently compiled, the simulation will markedly accelerate, and more importantly, the computation time dependence on r_{AV} will significantly reduce. This leads to overcoming one of the challenges of the original SEAKMC, namely the significant dependence of computation time on r_{AV} (Figure 3.2).

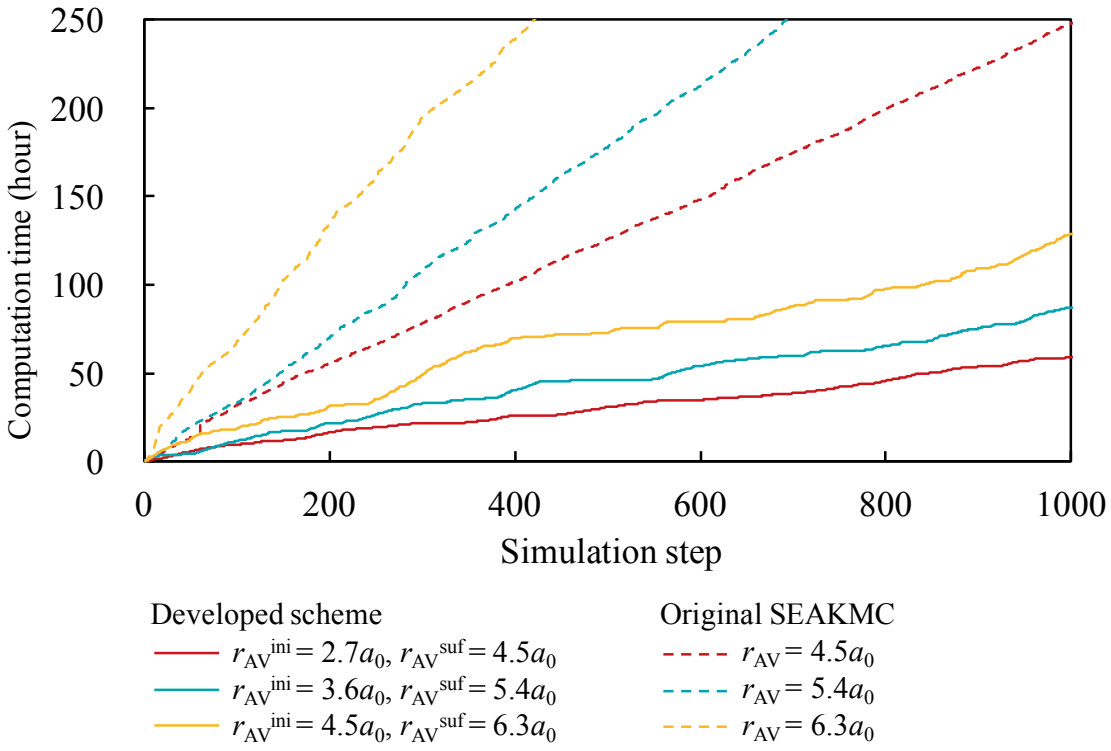

Figure 3.19 Comparison of elapsed computation time between the accelerated SEAKMC and original SEAKMC. The values of r_{AV}^{ini} and r_{AV}^{fin} are varied from $2.7a_0$ to $4.5a_0$ and from $4.5a_0$ to $6.3a_0$ in steps of $0.9a_0$ for the accelerated SEAKMC, while the value of r_{AV} is set from 4.5 to 6.3 in steps of $0.9a_0$ for the original SEAKMC.

3.4 Meso-timescale simulation of the behavior of irradiation-induced defect clusters using the accelerated SEAKMC

In this section, the application of the accelerated SEAKMC to irregularly shaped sessile SIA clusters observed in the MD cascade simulations in described Chapter 2 is discussed, and their meso-timescale behavior beyond the typical MD timescale is analyzed. The cell configuration of one of the 25 repeated calculation cases at $\Gamma_{SFE} = 44.1$ mJ m^{-2} under no strain was used in the MD simulations. The configuration at ~100 ps was used as an input to the SEAKMC simulations. An AV was set to one of the irregularly shaped sessile SIA clusters in the cell, and its evolution was simulated (Figure 3.20). Note that relatively large simulation cell containing more than 10,000,000 atoms was used in the MD cascade simulations. In the SEAKMC, however, there is minimal influence of the cell size on the calculation cost owing

to the introduction of AVs, which is one of the great benefits of SEAKMC. The value of r_{AV} was first set to $3.2a_0$ and then enlarged to $4.2a_0$ to obtain an accurate SP configuration. At every step, 180 SPSs were performed, and 36 repeated calculations were conducted using the same initial configuration and condition.

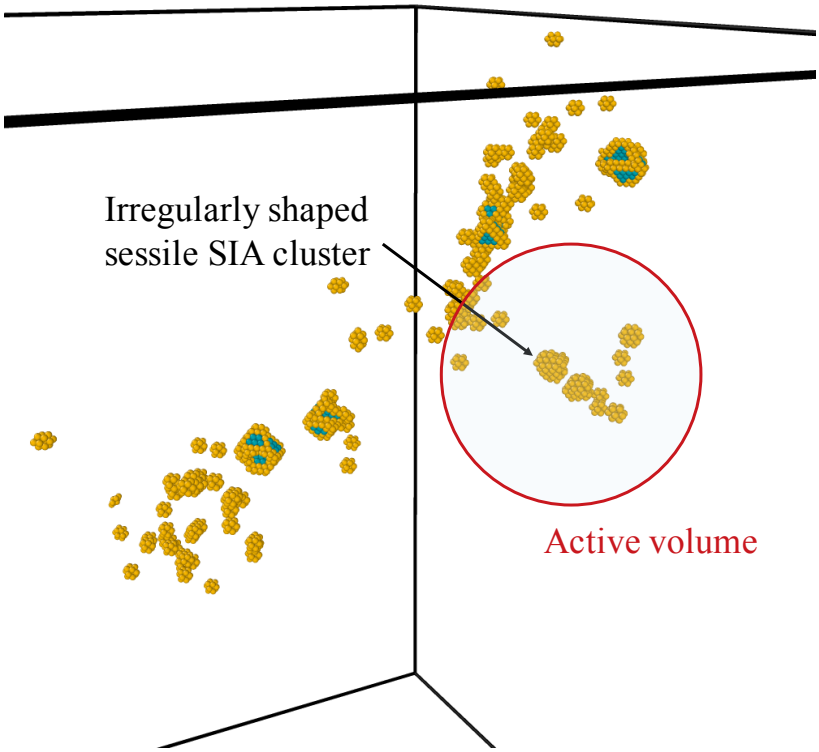

Figure 3.20 Schematic of the simulation cell.

Figure 3.21 shows the behavior of the cluster at one of the repeated calculations. The simulated time in the SEAKMC simulations is shown at the top of each figure. Initially, the cluster did not contain stacking fault areas, as shown in Figure 3.21(a). As the simulation proceeded, some atoms composing the cluster experienced core diffusions, and stacking fault areas were sometimes observed, as shown in Figure 3.21 (b); however, the cluster still retained an unstable three-dimensional configuration. Meanwhile, the cluster transformed into a platelet-like configuration at ~145.6 ps, which was similar to the configuration of a dislocation loop. A stacking fault also appeared on the habit plane of the cluster at this stage, while the area was not very large. Further, ~5.7 ps later, the cluster transformed into a two-dimensional dislocation loop. Here, it was observed that both sides of the habit plane of the

cluster contained a stacking fault, indicating that the cluster transformed into a Frank loop, as shown in Figures 3.21(d-1) and (d-2). The required time for the complete transformation process was ~151.3 ps, which is almost the limit of the timescale accessible to MD.

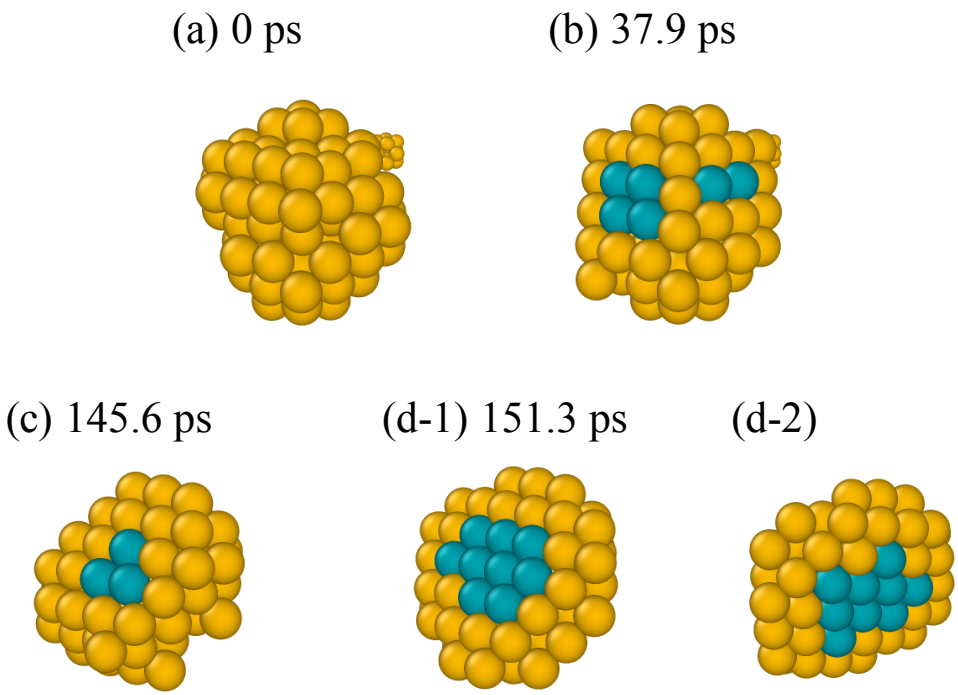

Figure 3.21 Cluster transformation into a Frank loop. The figure of (d-2) shows the habit plane at the opposite side of that in (d-1).

Figures 3.22 and 3.23 show the behavior of the cluster in another repeated calculation case. As shown in Figure 3.22, the transformation process of the cluster into a Frank loop was also observed in this calculation case. The required time for the transformation was ~847.6 ps, which was over five times more than that in the calculation case described above. Meanwhile, when the simulation further proceeded, blue atoms disappeared at the center of the habit plane of the loop, and a hole appeared instead in the CNA visualization. This indicates that the structure at the center of the habit plane transformed from HCP into FCC (Figures 3.23(c-1) and (c-2)). In addition, the loop glided back and forth along the direction perpendicular to the habit plane after the appearance of the FCC structure, indicating that the loop transformed into a perfect loop. The required time for the transformation from a Frank loop into a perfect loop was ~12.6 ns, which is approximately 100 times longer than the MD

timescale. After ~1.4 ns, the loop coalesced with a neighboring irregularly shaped SIA cluster, as in Figures 3.23(d-1) and (d-2), and a large SIA perfect loop was formed eventually through complex core diffusions of atoms (Figures 3.23(e-1) and (e-2)).

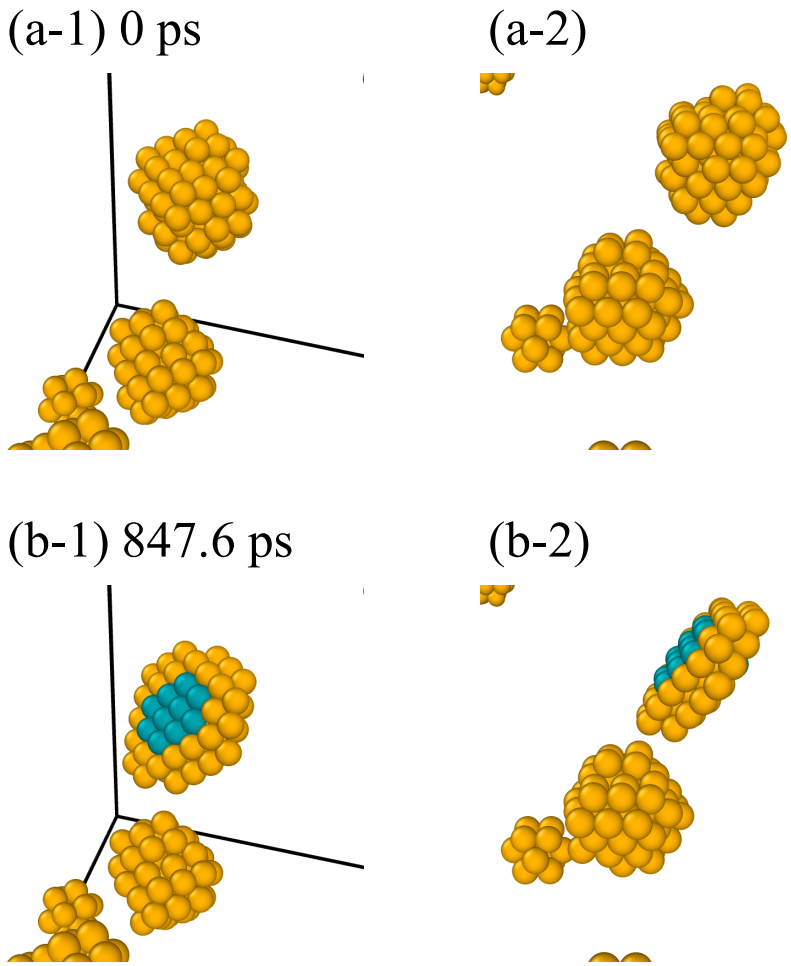

Figure 3.22 Transformation of an irregularly shaped SIA cluster into a Frank loop: (a-2) and (b-2) show the clusters in (a-1) and (b-1) from a different perspective, respectively.

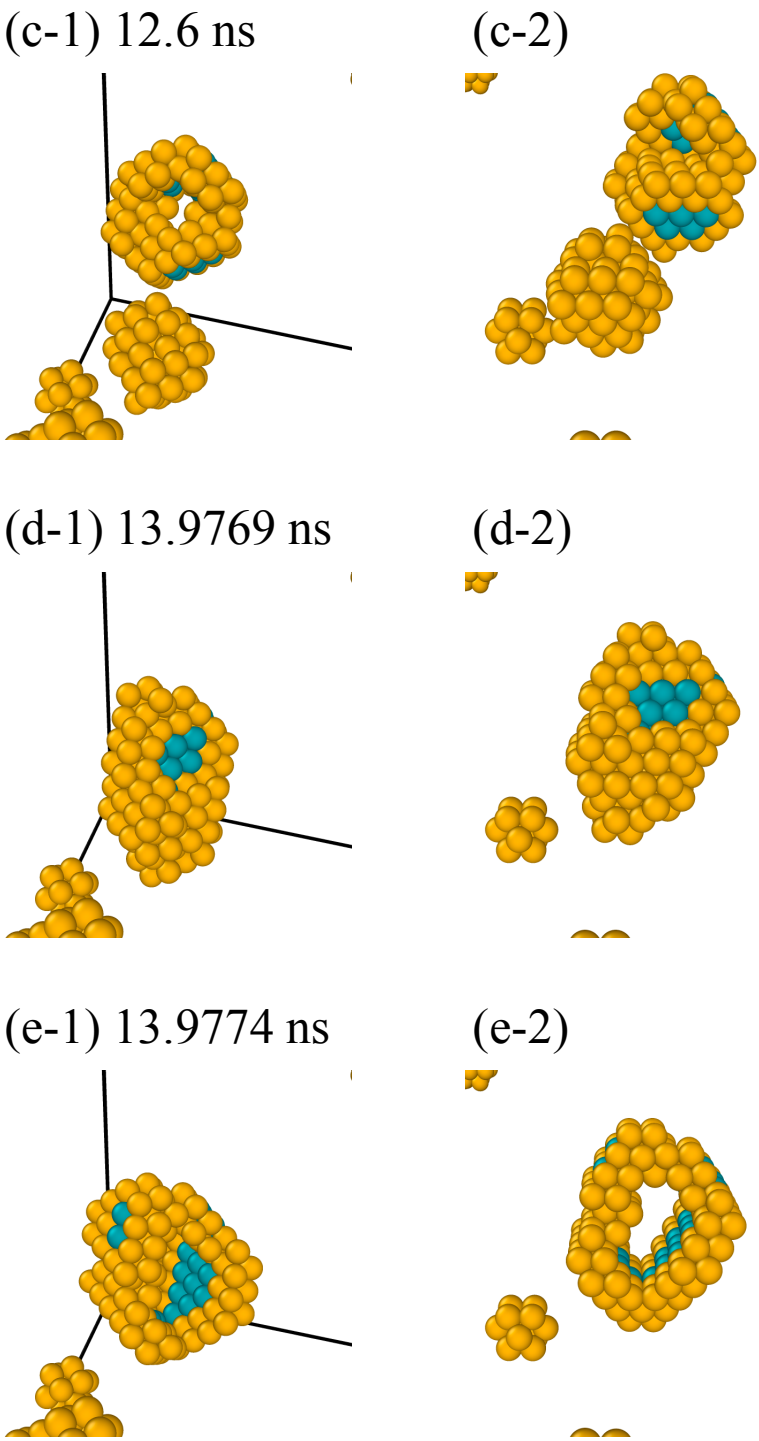

Figure 3.23 Coalescence of an SIA perfect loop with a neighboring irregularly shaped SIA cluster, followed by the formation of a larger SIA perfect loop: (c-2), (d-2), and (e-2) show the clusters in (c-1), (d-1), and (e-1), respectively, from a different perspective —the cluster in (c-1) was formed by the transformation of a Frank loop in Figure 3.22 (b-1).

In 10 of the 36 repeated calculations, the transformation process from the initial configuration to a Frank loop was observed, as seen in the two cases above. In addition, the required time for the transformation was of the order of 100 ps in most cases, which is almost the limit of the MD timescale. In three out of the 10 cases where the transformation into a Frank loop was observed, a further transformation process from the Frank loop into a perfect loop was also observed. Importantly, the required time for the transformation was more than several nanoseconds in all the three cases, which is much longer than the timescale accessible to MD. This indicates that the accelerated SEAKMC can simulate meso-timescale phenomena while tracking complex atomistic behavior. It should be noted that it has been difficult to treat the transformation processes observed here owing to the lack of the compatibility of atomistic fidelity and meso-timescale capability in MD and conventional kMC. The accelerated SEAKMC has great potential to reveal the detailed mechanism of such meso-timescale phenomena, which has been unknown with the use of conventional simulation methods for many decades.

3.5 Conclusions

- We proposed two acceleration schemes of SEAKMC for efficiently sampling SPs. First scheme was (i) a multistep procedure of SPS with increasing AV size, where a relatively small AV was first introduced, followed by SPSs with sufficiently large AVs to obtain an SP with the desired accuracy. Here, the result from the small-AV SPS was used as an input. Second scheme was (ii) the recycling of SPs sampled in previous steps as an input for the current-step SPSs. Each scheme was benchmarked by calculating the energy barriers of an SIA and a vacancy bulk diffusion in iron. Both schemes significantly accelerated SPS, while maintaining the fidelity comparable to the original method. Surprisingly, the simulation was accelerated by a factor of as much as ~100 in scheme (ii), while it was accelerated by a factor of 6–8 in scheme (i).
- These schemes were implemented together in the SPS procedure of SEAKMC, which was referred to as “prediction-based SPS.” The key of the prediction-based SPS is that, as the simulation proceeds, the more rapid simulation is achieved, because of more-frequent employment of scheme (ii), whose acceleration is much more

significant than that of the scheme (i). In addition, the prediction-based SPS has the potential to accelerate SEAKMC further by the construction of a vast database containing numerous AV and SP configurations applicable to various types of calculation; once it is constructed, a new calculation only goes through SPSs with the SP recycling, leading to the significant extension of the time-scale accessible to SEAKMC.

- The bulk diffusion of a three-SIA cluster in iron was simulated using the prediction-based SPS for evaluating its overall fidelity and efficiency; significant acceleration was achieved, and it was confirmed that it maintained the fidelity of the system dynamics comparable to MD results. In addition, the prediction-based SPS significantly lowered the dependence of computation time on AV size, suggesting its ability to treat relatively large defect dynamics, which has been a time-consuming task for the original SEAKMC.
- The accelerated SEAKMC was applied to the investigation of the stable configuration of an irregularly shaped sessile SIA cluster observed in the MD cascade simulations in Chapter 2. It was observed that the cluster transformed into an energetically stable configuration through very complex dynamics in the timescale beyond the typical MD simulations, i.e., more than several nanoseconds.
- SEAKMC has potential to be applied to various problems. For instance, the transformation process of an SIA Frank loop into an SIA perfect loop has been treated by using elasticity for many decades, where atomistic details are not considered, and a high energy barrier is required for the transformation. In addition, some studies have confirmed that even the direct interaction with a dislocation does not always induce the transformation process in the MD timescale [22]. In the SEAKMC simulations, however, the transformation process involving complex atomistic behavior was observed in a timescale of the order of more than several nanoseconds. This demonstrates that SEAKMC has a great capability to treat atomistic behavior of meso-timescale phenomena, which has been difficult under the use of conventional simulation methods. It is planned to reveal the underlying mechanisms of such phenomena in future studies.

References in Chapter 3

[1] C. H. Woo and B. H. Singh, "The concept of production bias and its possible role in defect accumulation under cascade damage conditions," *Physica Status Solidi,* vol. 159, pp. 609–616, 1990.

[2] C. H. Woo and B. N. Singh, "Production bias due to clustering of point defects in irradiation induced cascades," *Philosophical Magazine A,* vol. 65, pp. 889–912, 1992.

[3] G. Henkelman and H. Jonsson, "Long time scale kinetic Monte Carlo simulations without lattice approximation and predefined event table," *The Journal of chemical physics,* vol. 115, pp. 9657–9666, 1999.

[4] A. B. Bortz, M. H. Kalos and J. L. Lebowitz, "A new algorithm for Monte Carlo simulation of ising spin systems," *Journal of Computational Physics,* vol. 17, pp. 10–18, 1975.

[5] D. T. Gillespie, "Monte Carlo simulation of random walks with residence time dependent transition probability rates," vol. 28, pp. 395–407, 1978.

[6] L. Xu and G. Henkelman, "Adaptive kinetic Monte Carlo for first-principles accelerrated dynamics," *The Journal of Chemical Physics,* vol. 129, pp. 114104-1–114104-9, 2008.

[7] A. Kara, O. Trushin, H. Yildirim and T. S. Rahman, "Off-lattice self-learning kinetic Monte Carlo: application to 2D cluster diffusion on the fcc(111) surface," *Journal of Physics: Condensed Matter,* vol. 21, pp. 084213-1–084213-9, 2009.

[8] G. Nandipati, A. Kara, S. I. Shah and T. S. Rahman, "Off-lattice pattern recognition scheme for kinetic Monte Carlo simulations," *Journal of Computational Physics,* vol. 231, pp. 3548–3560, 2012.

[9] F. El-Mellouhi, N. Mousseau and L. J. Lewis, "Kinetic activation-relaxation technique: An off-lattice self-learning kinetic Monte Carlo algorithm," *Physical Review B,* vol. 78, pp. 153202-1–153202-4, 2008.

[10] L. K. Beland, P. Brommer, F. El-Mellouhi, J. Joly and N. Mousseau, "Kinetic activation-relaxation technique," *Physical Review E,* vol. 84, pp. 046704-1–046704-11, 2011.

[11] H. Xu, Y. N. Osetsky and R. E. Stoller, "Simulating complex atomistic processes: On-the-fly kinetic Monte Carlo scheme with selective active volumes," *Physical Review B,*

vol. 84, pp. 132103-1–132103-4, 2011.

[12] H. Xu, Y. N. Osetsky and R. E. Stoller, "Self-evolving atomistic kinetic Monte Carlo: fundamantals and applications," *Journal of Physics: Condensed Matter,* vol. 24, pp. 375402-1–375402-10, 2012.

[13] H. Xu, R. E. Stoller, L. K. Beland and Y. N. Osetsky, "Self-evolving atomistic kinetic Monte Carlo simulations of defets in materials," *Computational Materials Science,* vol. 100, pp. 135–143, 2015.

[14] A. Ervin and H. Xu, "Mesoscale simulations of radiation damage effects in materials: A SEAKMC perspective," *Computational Materials Science,* vol. 150, pp. 180–189, 2018.

[15] H. Xu, R. E. Stoller and Y. N. Osetsky, "Cascade defect evolution processes: Comparison of atomistic methods," *Journal of Nuclear Materials,* vol. 443, pp. 66–70, 2013.

[16] G. Henkelman and H. Jonsson, "A dimer method for finding saddle points on high dimensional potential surfaces using only first derivatives," *Journal of Chemical Physics,* vol. 111, pp. 7010–7022, 1999.

[17] A. Heyden, A. T. Bell and F. J. Keil, "Efficient methods for finding transition states in chemical reactions: Comparison of improved dimer method and partitioned rational function optimiztion method," *The Journal of Chemical Physics,* vol. 123, pp. 224101-1–224101-13, 2005.

[18] G. J. Ackland, M. I. Mendelev, D. J. Srolovitz, S. Han and A. V. Barashev, "Development of an interatomic potential for phosphorus impurities in a-iron," *Journal of Physics: Condensed Matter,* vol. 16, pp. S2629–S2642, 2004.

[19] N. Soneda and T. Diaz de la Rubia, "Migration kinetics of the self-interstitial atom and its clusters in bcc Fe," *Philosophical Magazine A, vol.* 81, pp. 331–343, 2001.

[20] N. Anento, A. Serra and Y. N. Osetsky, "Atomistic study of multimechanism diffusion by self-interstitial defects in a-Fe," *Modelling and Simulation in Materials Science and Engineering,* vol. 18, pp. 025008-1–025008-18, 2010.

[21] Y. N. Osetsky, "Atomistic study of diffusional mass transport in metals," *Defect and Diffusion Forum,* vol. 188–190, pp. 71–92, 2001.

[22] S. Hayakawa, Y. Hayashi, T. Okita, M. Itakura, K. Suzuki and Y. Kuriyama, “Effects of stacking fault energies on the interaction between an edge dislocation and an 8.0-nm-

diameter Frank loop of self-interstitial atoms," *Nuclear Materials and Energy*, vol. 9, pp. 581–586, 2016.

Chapter 4 Exploring the stable configuration of microstructures using an optimization algorithm

4.1 Motivation and background

In Chapter 3, we proposed an acceleration scheme for SEAKMC, which is one of the on-the-fly kMC techniques. In addition, we applied the accelerated SEAKMC to a meso-timescale simulation of the irregularly shaped SIA clusters produced using cascade simulations in Chapter 2. The obtained results indicated that the accelerated SEAKMC had the capability to efficiently simulate meso-timescale phenomena while maintaining atomistic fidelity. Meanwhile, it should also be stressed that this does not mean that any irregularly shaped SIA clusters can transform into Frank loops or perfect loops through SEAKMC simulations. For instance, one of the irregularly shaped SIA clusters observed in the MD simulations in Chapter 2 is shown in Figure 4.1. Note that this cluster is not the same as that simulated in Chapter 3. When the accelerated SEAKMC was applied to this cluster, no transformation into a Frank loop or a perfect loop was seen, even after several hundred simulation steps. This was because most of the simulation steps were spent on simulating events involving only trivial atomic displacements, which do not directly lead to the transformation process.

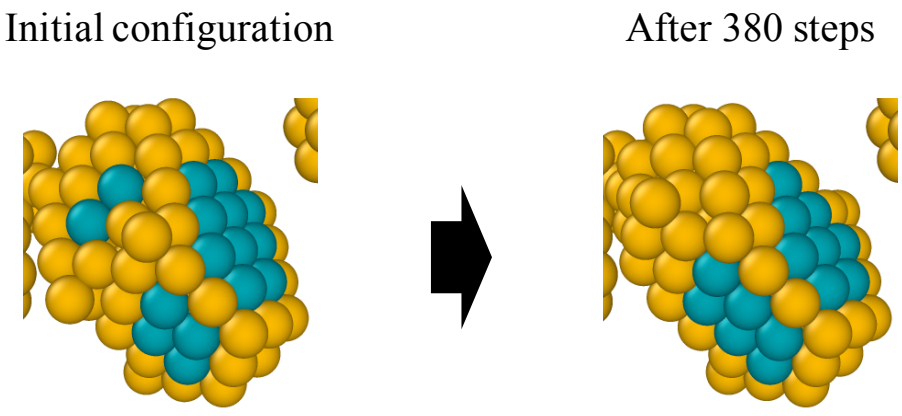

Figure 4.1 Irregularly shaped SIA cluster that retained an irregular shape after several hundred SEAKMC simulation steps. Blue indicates a stacking fault, while yellow indicates irregular structure.

As described in Chapter 3, event selection in SEAKMC is conducted stochastically using a random number, and importantly, when events with a low energy barrier (E_a) and those with a high E_a are found together in a list, the former events are chosen in most cases. For instance, when an event with E_a = 0.1 eV and one with E_a = 1.0 eV are listed together, their frequencies are calculated as ~2.1 × 10^{10} s^{-1} and ~1.6 × 10^{-5} s^{-1} at 300 K, respectively, based on Eq. (4.1).

$$\nu = A \exp\left(-\frac{E_a}{k_B T}\right) \tag{4.1}$$

Note that A, k_B, and T denote a pre-exponential factor, the Boltzmann constant, and temperature, respectively. The value of A is set to 10^{12} s^{-1} here. Because the probability of each event to be chosen is weighted by its frequency, an event with E_a = 0.1 eV would be chosen in almost all event selections. Considering the fact that many irregularly shaped clusters did not transform into either a Frank loop or a perfect loop within the MD timescale (see Chapter 2), the entire transformation process would need to go through a relatively high E_a. In other words, when the list contains trivial events with low E_a, for example, events involving only slight displacements of a few atoms, it is tremendously time-consuming to simulate the entire transformation process that we desire to observe. Such trivial events are called “flicker events,” and flicker events have been known as a common problem not only in SEAKMC but also in general kMC approaches. Due to this, it is difficult to avoid the effect of flicker events while using a kMC method framework, suggesting that it would be useful to employ other approaches, maintaining the meso-timescale simulation capability, rather than using the kMC alone.

The key to the meso-timescale capability of kMC is the concept of state-to-state dynamics, wherein the dynamics are modeled not by the numerous interactions of atomic vibrations, but by climbing the PES slope toward an SP and descending into the energy basin beyond the SP (Figure 4.2). A modeling approach that follows the state-to-state dynamics seems quite useful for extending the simulation timescale. When considering the PES of the system, the transformation process of irregularly shaped clusters into stable ones corresponds to the transition from higher-energy basins to lower-energy basins on the PES, i.e., the transformation process can be modeled as the system’s hopping on energy basins toward

lower-energy states (Figure 4.3 (a)). When rephrasing it with a more general expression, it corresponds to energy minimization in the topological space composed of the set of energy basins on the PES (Figure 4.3 (b)).

Based on these understanding, we develop a simulation method to investigate the stable configuration of microstructures through the application of an optimization algorithm (EM/BCS). The key feature of EM/BCS is that exploration of the stable configuration is modeled as an energy minimization problem. In addition, EM/BCS is applied to the irregularly shaped SIA clusters observed in the MD cascade simulations in Chapter 2, and we investigate their transformation process into stable configurations, namely Frank loops or perfect loops, which occurs beyond the typical MD timescale.

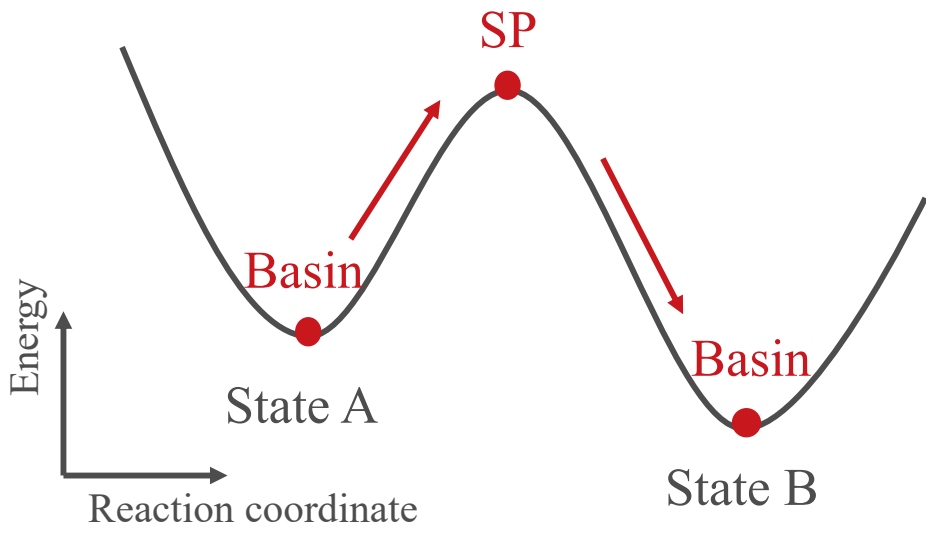

Figure 4.2 Schematic image of the concept of state-to-state dynamics.

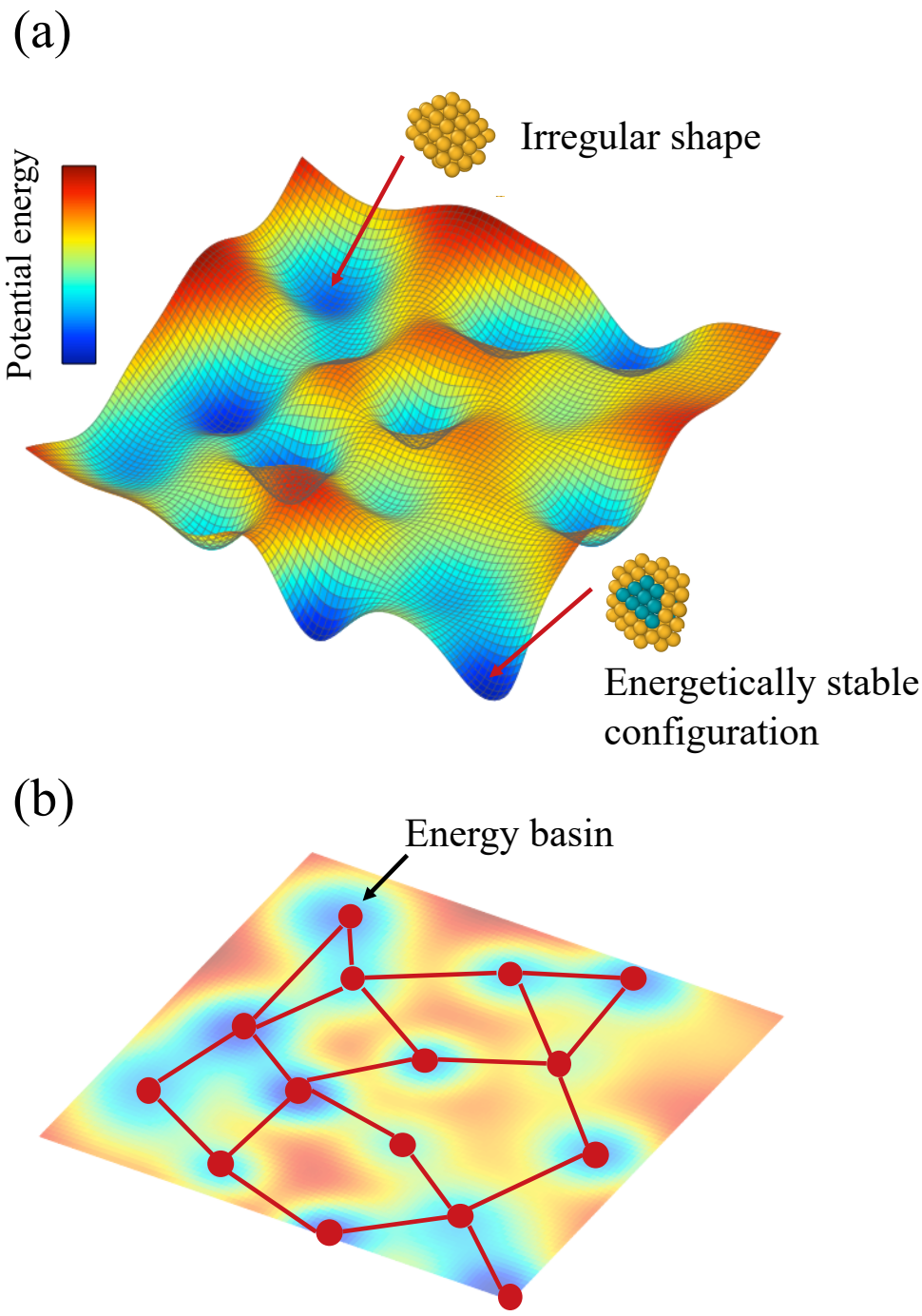

Figure 4.3 (a) Schematic image of the PES of the system, and (b) schematic image of the set of energy basins on the PES.

4.2 Simulation method

In principle, various optimization algorithms can be implemented in EM/BCS, and it is considered that the suitable algorithm is dependent on the focus problem. In selecting an optimization algorithm suitable for this study, there were two factors to be concerned with.

1. The PES in this study appears quite complicated, because the high number of atoms contained in the simulation cell renders the degree of freedom of the system quite large. This leads to the creation of many local minima, indicating that global optimization capability is required to prevent the system from being trapped at a local minimum.

2. Optimization is performed with real dynamics in mind; thus, energy basins that the system visits during the simulation should be limited to basins that are reachable from the initial basin within a practical timescale. This indicates that an optimization algorithm based on neighborhood search is more suitable here, where the solution is updated through the slight displacements of atomic coordinates. Another typical optimization procedure, where initial solutions are dispersed over the whole topological space at random and the most favorable solution obtained is defined as the optimized solution, is not suitable here.

Based on these factors, we employ TPSA [3,4] as the optimization algorithm in this study. The TPSA algorithm is based on the simulated annealing (SA) method [5], and it overcomes the difficulty of adjusting the cooling schedule of the temperature parameter and the high computational cost of SA. The SA and TPSA procedures are briefly summarized below.

4.2.1 Simulated annealing

SA, developed by Kirkpatrick et al. [5], is a stochastic algorithm for global optimization, and it has been employed in a wide range of applications for both discrete and continuous optimization problems because of its simple framework and easy implementation [5–17]. One of the differences between SA and other typical optimization algorithms, such as the steepest descent method and the conjugate gradient method, is that SA allows the solution to deteriorate stochastically, which helps the system escape from a local minimum. Figure 4.4 shows a flowchart of the SA algorithm.

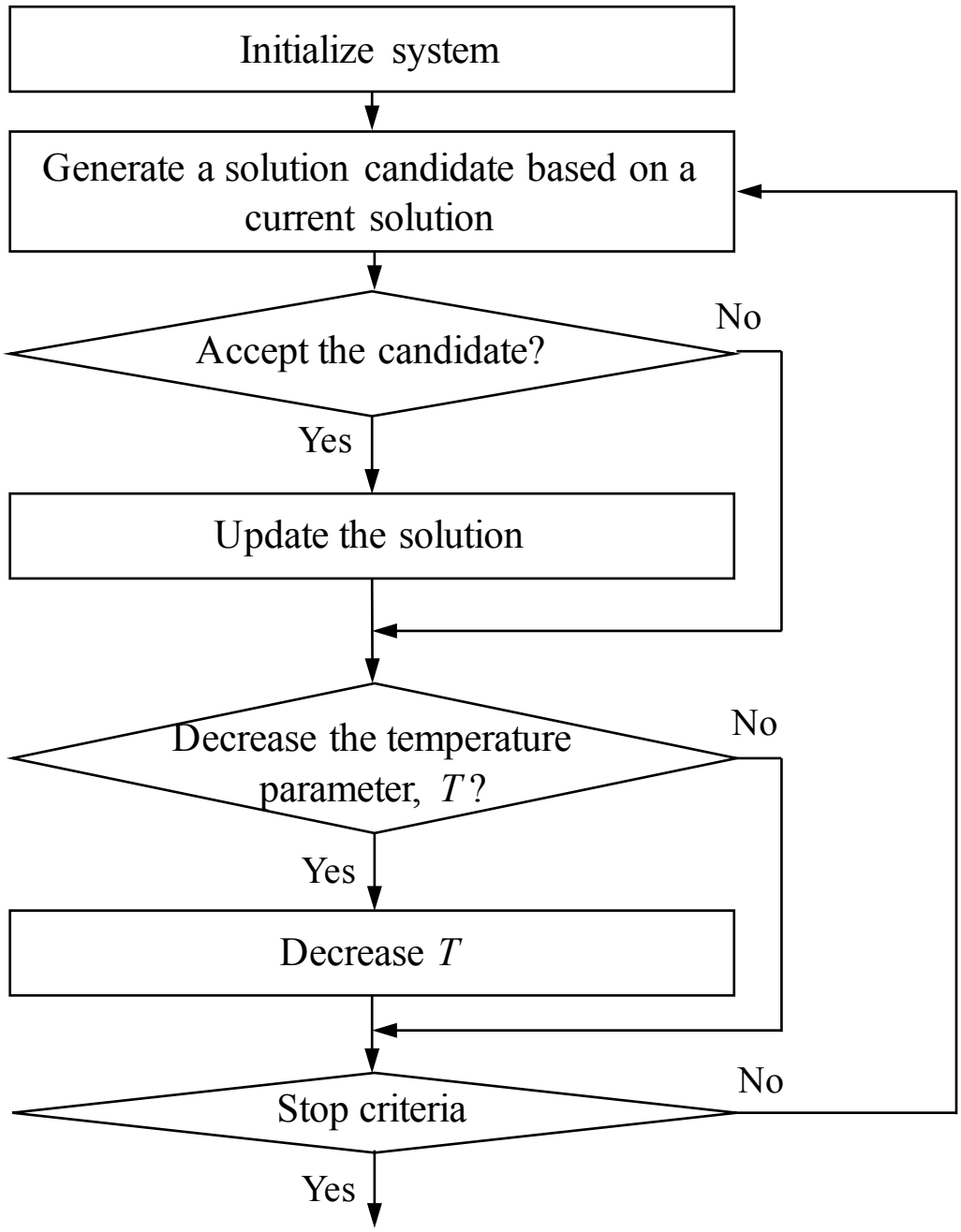

Figure 4.4 Flowchart of the SA algorithm.

At each step, we begin with a neighborhood search, wherein a candidate of the next-step solution is sought in the neighboring area of the current solution. Once the candidate is found, we evaluate it using the acceptance function, P_{acp}, and judge whether the candidate is acceptable or not. In principle, various kinds of functions can be used as P_{acp}. Here, we use the Metropolis algorithm [18], where P_{acp} is described as:

$$P_{\mathrm{acp}} = \begin{cases} 1 & \text{if } \Delta E < 0 \\ \exp\left(-\dfrac{\Delta E}{T_i}\right) & \text{otherwise} \end{cases} \tag{4.2}$$

$$\Delta E = E_{\mathrm{new}} - E_{\mathrm{current}}$$

where E_{new}, E_{current}, and T_i denote the energy of the solution candidate, the energy of the current solution, and the temperature parameter, respectively. The T_i decreases gradually as the simulation proceeds, as shown in Figure 4.5. This lowers the acceptance probability of events that deteriorate the solution in later stages of the simulation, while such deteriorating events are accepted with a relatively higher probability at earlier stages of the simulation (Figure 4.6). This procedure corresponds to the annealing workflow in real situations, where a certain metal is cooled after it is heated. This explains the origin of the term "simulated annealing." In theory, it has been proved that the SA can explore the global minimum if the cooling schedule of T_i satisfies the condition below [15,19]:

$$T_i \leq \frac{A}{\log i} \tag{4.3}$$

where A and i denote a parameter expressing the complexity of the PES and the number of changes in T_i, respectively. This indicates that a vast amount of calculation is required for obtaining the global minimum. Hence, in many practical applications, the aim of the simulation shifts to exploring the approximate global minimum, and the cooling schedule is set to follow the equation below:

$$T_{i+1} = \alpha T_i, \quad 0 < \alpha < 1 \tag{4.4}$$

In general, the cooling schedule of T_i is problem dependent. Thus, it is necessary to set the cooling schedule to suit the focus problem, and it is usually determined empirically.

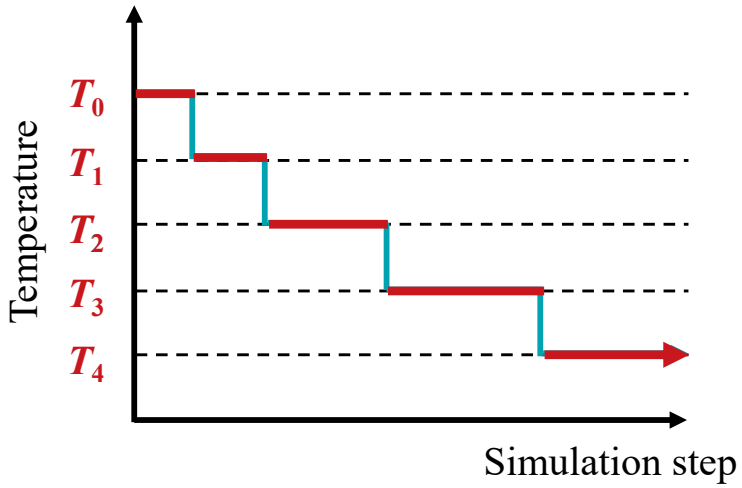

Figure 4.5 Decrease in T_i with increase in the simulation steps.

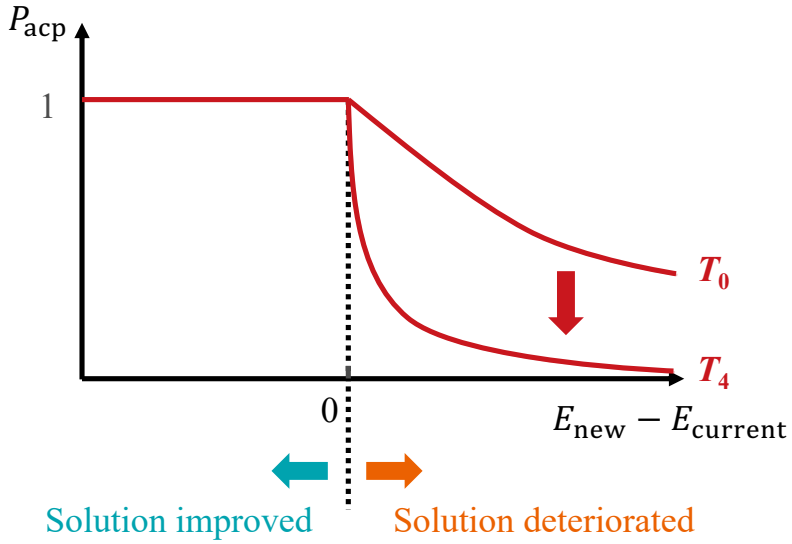

Figure 4.6 The decrease in the acceptance probability of events that deteriorate the solution, in accordance with the decrease in T_i.

4.2.2 Temperature parallel simulated annealing

In spite of its power and wide applicability, the disadvantages of the SA algorithm are also well recognized.

1. It tends to take quite a long computation time to obtain the solution with the desired accuracy [10,14]. For instance, for the traveling salesman problem, widely known as a typical optimization problem, a previous study has reported that computation time required for obtaining a solution with good accuracy by SA is larger than that for brute-force search [15].

2. It is difficult to determine a suitable cooling schedule for T_i for the focus problem. In addition, a previous study has shown that unsuitable cooling schedules can lead to deterioration of the obtained solution [16]. Further, additional calculations are needed beforehand, in some cases.

For the acceleration of SA, some parallel computation approaches have been proposed [20–23]. One of the most typical methods of parallel computation is to conduct SA simulations with multiple processors using initial solutions that differ from each other; then, the most favorable solution is copied to all the processors at a certain step interval. However, the difficulty in determining a suitable cooling schedule remains.

These considerations motivated the development of TPSA [4], which was previously called time-homogenous parallel annealing [3]. The TPSA flowchart is shown in Figure 4.7. In TPSA, a sequential SA with an unchanged T_i is conducted on each processor, while different values of T_i are assigned to different processors. After a pre-set number of simulation steps, the processors go through a procedure where the solution can be exchanged with the processor that has the adjacent T_i (Figure 4.8). The cooling process in the sequential SA, where the value of T_i is decreased to the adjacent value, corresponds to the solution exchange procedure in TPSA, where solutions are exchanged between two processors that have adjacent values of T_i. Also, the cooling schedule in the sequential SA corresponds to the solution exchange frequency in TPSA. The timing of the solution exchange is determined by calculating the probability P_{ex} in Eq. (4.5), which solves the problem of empirically determining the T_i cooling schedule in the sequential SA:

$$P_{\mathrm{ex}} = \begin{cases} 1 & \text{if} \quad \Delta T \cdot \Delta E < 0 \\ \exp\left(-\dfrac{\Delta T \cdot \Delta E}{T_i \cdot T_{i+1}}\right) & \text{otherwise} \end{cases} \qquad (4.5)$$

$$\Delta E = E_{i+1} - E_i, \qquad \Delta T = T_{i+1} - T_i$$

Note that E_i and E_{i+1} denote the system energy of the processor with T_i and T_{i+1}, respectively. Under the definition of P_{ex} as in Eq. (4.5), solutions are always exchanged when the higher-temperature processor has a lower-energy solution, while solutions are stochastically exchanged otherwise based on the difference in the temperature and energy between the processors. This means that lower-energy solutions tend to gather at lower-temperature processors and experience more intense energy minimization, while higher-energy solutions tend to gather at higher temperature processors and explore lower-energy states across a wider area of the PES. It should be mentioned that the TPSA algorithm has another advantage. In sequential SA, an annealing procedure where T_i is increased again is necessary if one would

like to obtain a better solution after the optimization. However, the increase amount and the increase period are not clear in most cases. The TPSA algorithm, on the other hand, does not have parameters dependent on simulation steps, meaning that one can simply restart the TPSA simulation that was terminated at any point during the simulation period without any change in the parameter values if one is not satisfied with the accuracy of the obtained solution. Because of its advantages, TPSA is employed in a wide range of applications to both discrete and continuous optimization problems, which have demonstrated its power and usefulness [3,4,24–27].

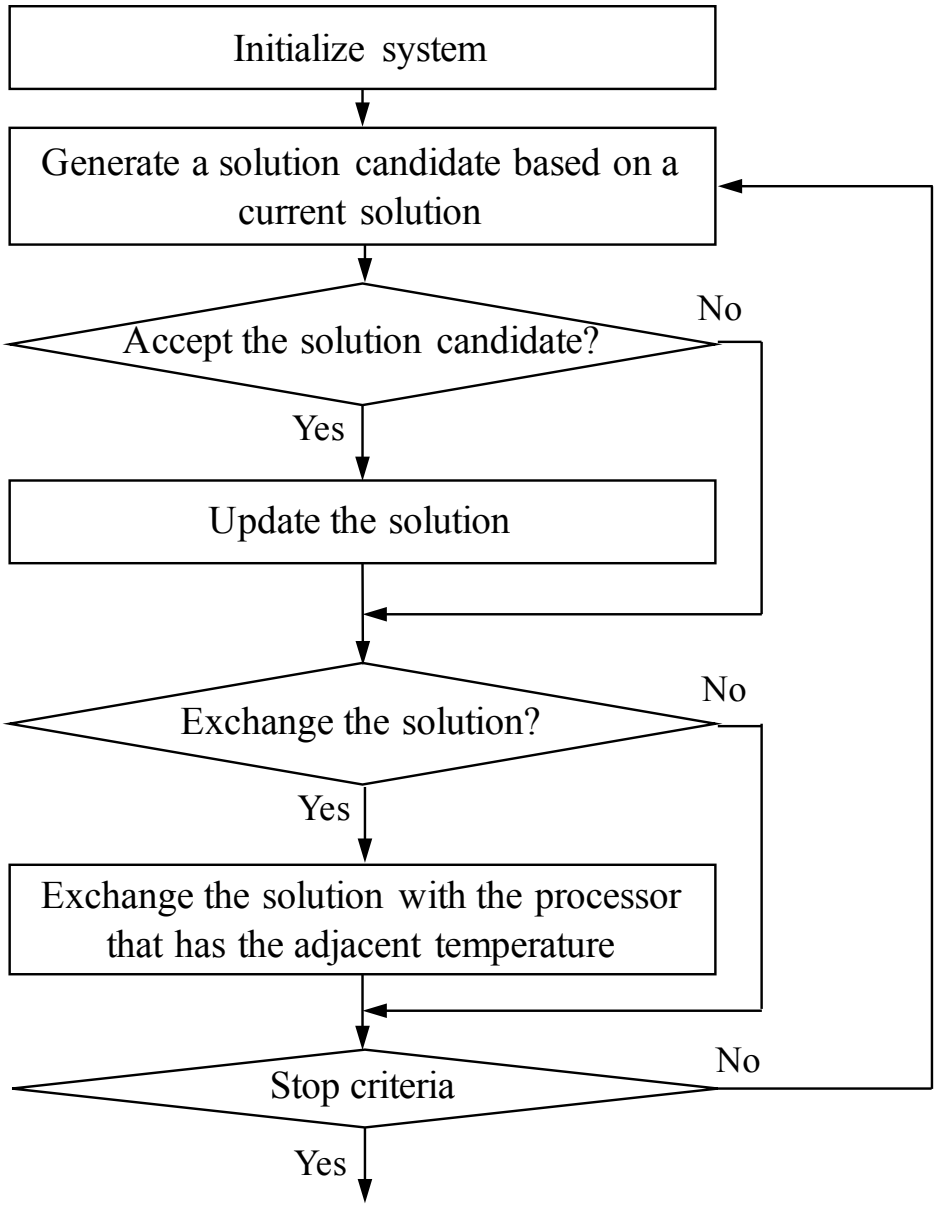

Figure 4.7 Flowchart for TPSA.

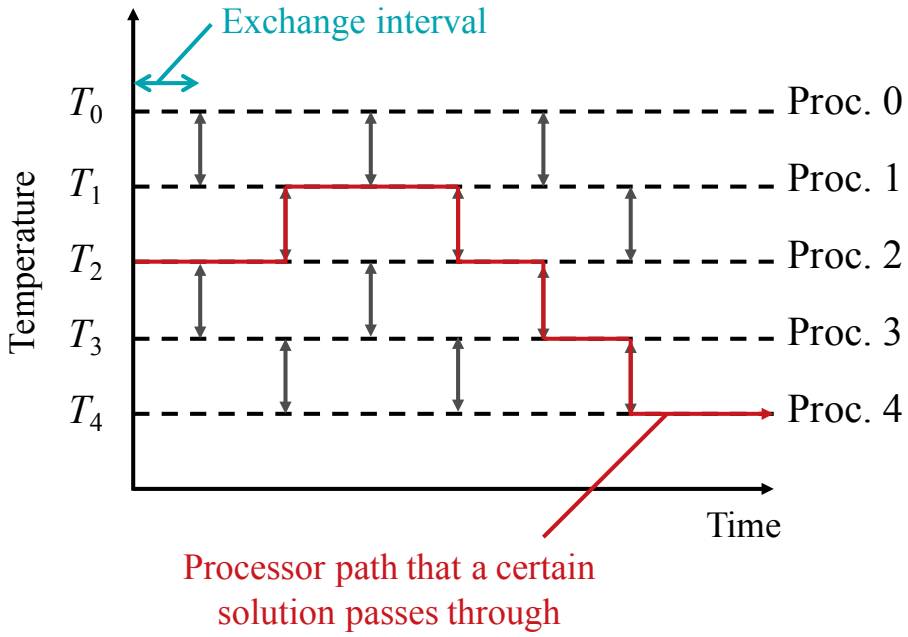

Figure 4.8 Solution exchange procedure in TPSA.

4.3 Investigating the stable configuration of irradiation-induced defect clusters based on TPSA

In this study, we investigate the stable configuration of irregularly shaped sessile SIA clusters, observed in the MD cascade simulations in Chapter 2, by using EM/BCS with TPSA. As stated in the last section, a candidate for the new solution is sought in the neighborhood of the current solution in TPSA (neighborhood search). Here, it should be noted that the definition of "neighborhood" in this study is different from that in the application of TPSA (SA) to general continuous optimization problems. Typically, the neighborhood is defined by a probability distribution function with respect to the distance from the current solution. The probability distribution function is selected so that the probability is relatively higher around the origin while it drastically decreases with increasing distance from the origin, e.g., Gaussian distribution and Cauchy distribution [28,29]. Such a definition of neighborhood is also applicable in this study because the system energy is continuous; however, some disadvantages arise: (i) it is not clear which distribution function is suitable, (ii) multiple steps are necessary for one basin-hop, rendering the calculation cost high, and (iii) the arbitrary definition of the neighborhood incurs the risk of skipping several basins within one step, which can lead to unrealistic state-to-state dynamics. Based on these, we define the

neighborhood in this study as the set of basins neighboring the current basin, and the system experiences state-to-state transitions by hopping to neighboring basins. To search for neighboring basins, we first use the dimer method with the employment of AV to find SPs, and then perform energy minimization to locate the basin beyond the found SP, as in SEAKMC (see Chapter 3). This enables us to track the dynamics accurately based on the PES while maintaining efficiency through the employment of AV. As in Chapter 3, we introduce spherical AVs with a radius of r_{AV}, centered around each SIA identified with Wigner–Seitz defect analysis. If the identified defects compose a cluster, resulting in an overlap of the AV region with those of neighboring SIAs, we combine the regions and treat them as one AV (Figure 4.9). Further, it should be stressed that the acceleration scheme proposed in Chapter 3 is applicable to SPS here, as well. In the present calculations, we first conduct SPS with $r_{AV} = 3.2a_0$, followed by SPS with $r_{AV} = 4.2a_0$ while using the first SPS result as an input.

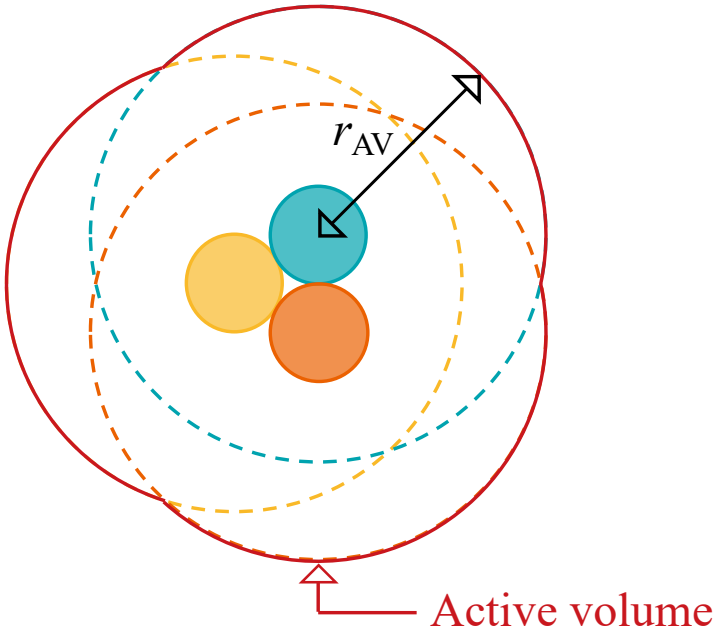

Figure 4.9 Schematic explanation of the manner of characterizing an AV when several AV regions overlap (reproduced from Figure 3.4).

It should be noted that, in evaluating the acceptance of a found event, we consider the energy difference between the current basin and the found basin, and do not take into account the E_a between the basins. EM/BCS is based on an optimization algorithm and aims to explore

energetically favorable states in principle. In other words, the simulated process does not necessarily follow real dynamics. This means that events with a relatively high E_a can be accepted as long as the system energy is decreased, or the energy increase is very small. We should thus bear in mind that the check of E_a values that the system experiences through the simulation is necessary for examining whether the observed transformation process is energetically feasible with real dynamics.

In TPSA, we need to set several input parameters beforehand, namely the maximum T_i (T_{max}), the minimum T_i (T_{min}), the number of processors, the manner of distributing the temperature values to each T_i, and the interval for exchanging basins between the processors. Konishi et al. [4] determined the value of T_{max} in a combinational optimization problem so that the worst solution update would be accepted with a probability of 50 % at T_{max}. Based on this, we also determined the value of T_{max} so that the basin hop with ΔE = 2.5 eV would be accepted with a probability of 50 % at T_{max}. Note that the 2.5 eV difference between two basins means that the E_a between the basins is at least 2.5 eV. Considering that the occurrence frequency of a certain dynamic is described with the Boltzmann factor, the waiting time of an event with E_a = 2.5 eV is estimated to be approximately 3 yr at 600 K, as shown in Eq. (4.6):

$$\tau_{wt} = A^{-1}\exp\left(\frac{E_a}{k_B T}\right) \tag{4.6}$$

where τ_{wt}, A, and k_B denote the waiting time, a pre-exponential factor, and the Boltzmann constant, respectively. This indicates that the determined value of T_{max} here is adequate for searching the PES areas reachable within a practical timescale. In addition, we determined the value of T_{min} so that a basin hop with ΔE = 0.01 eV would be accepted with a probability of 50 % at T_{min}, as in the case of T_{max}. The specific values of T_{max} and T_{min} were calculated with the equation below, obtained through the transformation of Eq. (4.2):

$$\begin{aligned} T_{max} &= -\frac{\Delta E_{max}}{\ln a_{max}}, \\ T_{min} &= -\frac{\Delta E_{min}}{\ln a_{min}} \end{aligned} \tag{4.7}$$

where ΔE_{max}, ΔE_{min}, a_{max}, and a_{min} are set to 2.5, 0.01, 0.5, and 0.5, respectively. The number of processors was set to 12, and the temperature values were distributed to the processor using Eq. (4.4) in this study (Table 4.1). Note that, in TPSA, one of the processors has an ultra-low temperature (i.e., the temperature is set to 0), where only basin hops with $\Delta E < 0$ are accepted during the entire simulation period. The basin exchange between the processors was conducted at intervals of 10 simulation steps. In concept, the value of T_i is consistent throughout the simulations, and the basins are exchanged between the processors. The amount of information to exchange, however, would be quite large in this process because the basin information in this study contains the coordinates of tens of millions of atoms. Due to this, we exchanged the temperature values instead of the basins between the processors in the performed simulations. This considerably reduced the amount of information passed between processors without affecting the algorithm, resulting in an acceleration of the simulations [3]. We simulated 45 patterns of the irregularly shaped SIA clusters observed in Chapter 2, and more than 10 repeated calculations were conducted under the same conditions in order to check the variations of the obtained results.

Table 4.1 The values of T_i at each processor. Note that the values in the right column indicate the energy difference between the current basin and the newly found basin when the acceptance probability is 50 % at each T_i.

Proc. ID	T_i	ΔE (eV) at $P_{ex} = 0.5$
0	0	–
1	167.4	0.010
2	290.8	0.017
3	505.1	0.030
4	877.4	0.052
5	1524.0	0.091
6	2647.2	0.158
7	4598.1	0.275
8	7986.9	0.477
9	13873.0	0.829
10	24097.1	1.439
11	41856.1	2.500

Now let us discuss the obtained results. Figure 4.10 shows one of the observed transformations of a cluster into a Frank loop, which is one of the stable configurations of SIA clusters in FCC metals. In this case, the transformation was observed after ~60 simulation steps, after which little change in the cluster shape was observed although we further proceeded with more than 100 simulation steps. Figure 4.11 shows the system energy history during the transformation process shown in Figure 4.10. Note that only the energies in the basins are depicted in the figure; E_a values are not included. We can clearly see a drastic decrease in the system energy around simulation step 60, corresponding with the cluster transformation process shown in Figure 4.10.

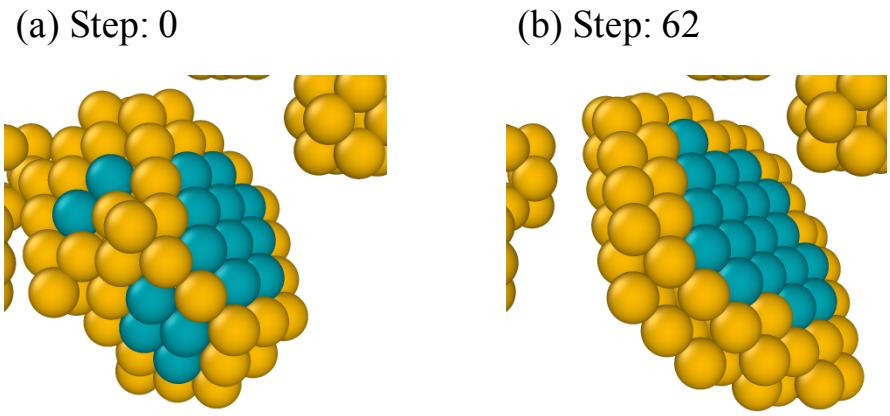

Figure 4.10 Observed transformation process: (a) Irregularly shaped SIA cluster, and (b) a Frank loop.

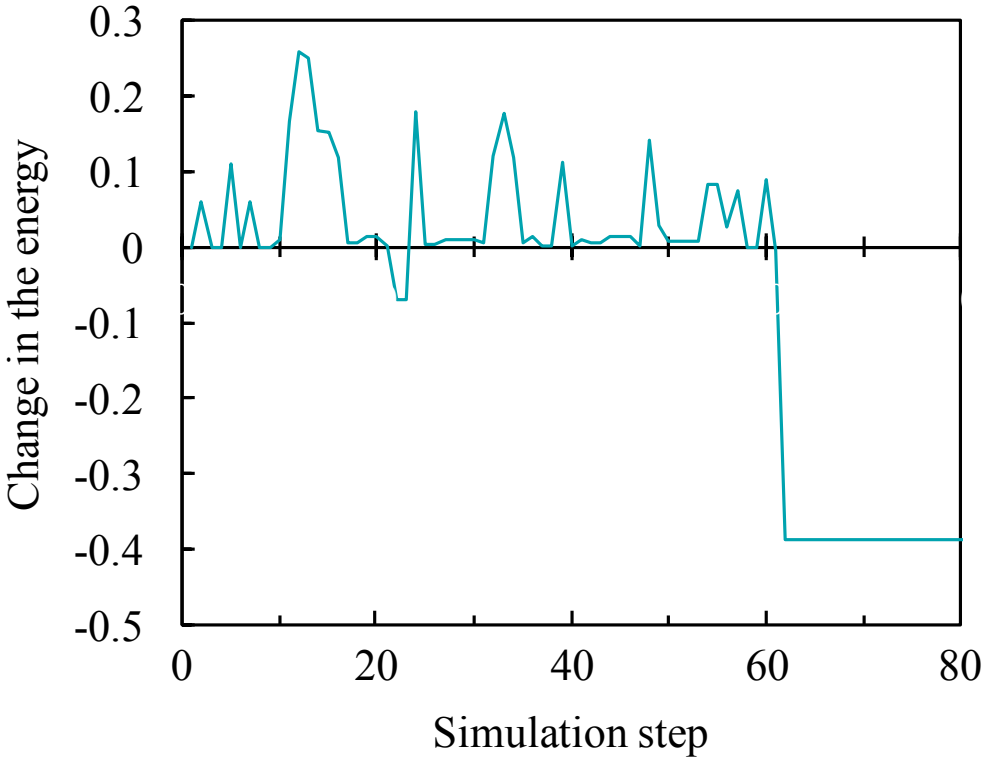

Figure 4.11 System energy history during the transformation process shown in Figure 4.10.

Figure 4.12 shows one of the observed transformations of a cluster into a perfect loop, which is another stable configuration of SIA clusters in FCC metals. As shown in Figure 4.12 (b-1) and (b-2), a hole was seen at the center of the cluster around step 150 in CNA visualization, indicating that the habit plane of the cluster had an FCC structure. Further, some of the cluster edges split into partial dislocations, with a stacking fault area between them. On the other hand, stable SIA perfect loops typically have stacking fault areas at all their edges, as shown in Figure 4.13, indicating that the configuration observed in Figure 4.12 (b-1) and (b-2) is a meta-stable configuration. After ~100 simulation steps, all the four edges contained stacking fault areas, and the stable configuration of a perfect loop was observed, as shown in Figure 4.12 (c-1) and (c-2). We further proceeded with over 100 steps of the simulation; however, no significant change in the configuration was observed. Figure 4.14 shows the system energy history during the transformation process shown in Figure 4.12. It is evident that the energy gradually decreases as the simulation proceeds, and the energy eventually converges to a certain value at approximately step 200. Further, we can confirm that the system energy remained ~ –1.2 eV at approximately steps 150–200. During this plateau-like period, the

cluster was in a meta-stable configuration, as shown in Figure 4.12 (b-1) and (b-2), demonstrating a reasonable agreement between the energy history and the observed transformation process. These results indicate that the method developed here, namely, EM/BCS, accurately simulates the dynamics that the system experiences.

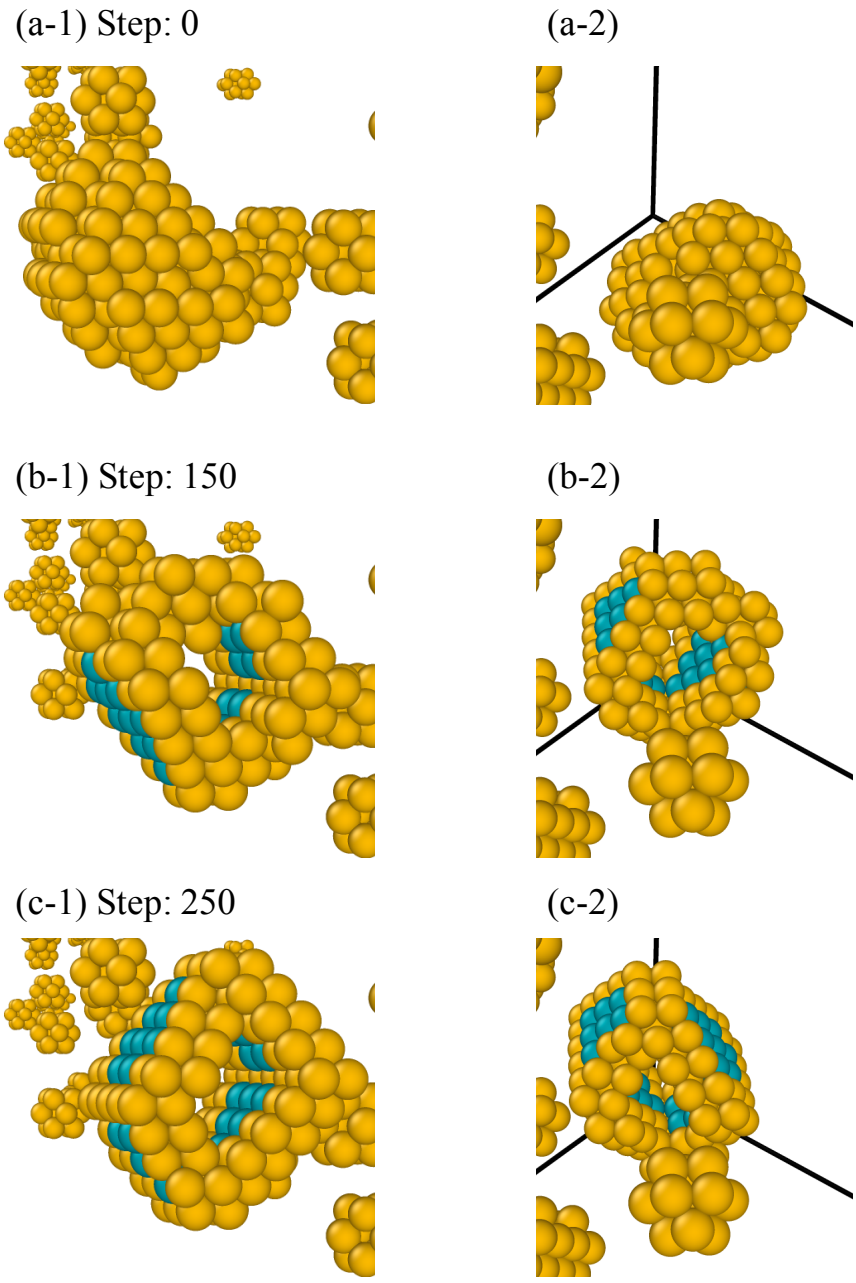

Figure 4.12 Observed transformation process: (a-1) irregularly shaped SIA cluster, (b-1) a meta-stable configuration, and (c-1) a perfect loop. (a-2), (b-2) and (c-2) show the clusters in (a-1), (b-1) and (c-1) from a different perspective, respectively.

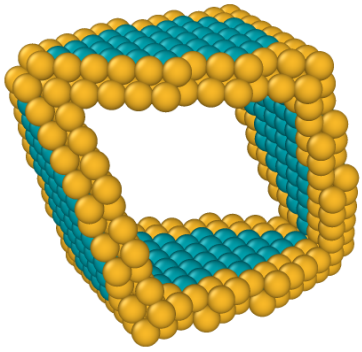

Figure 4.13 SIA perfect loop (reproduced from Figure 2.1 (c)).

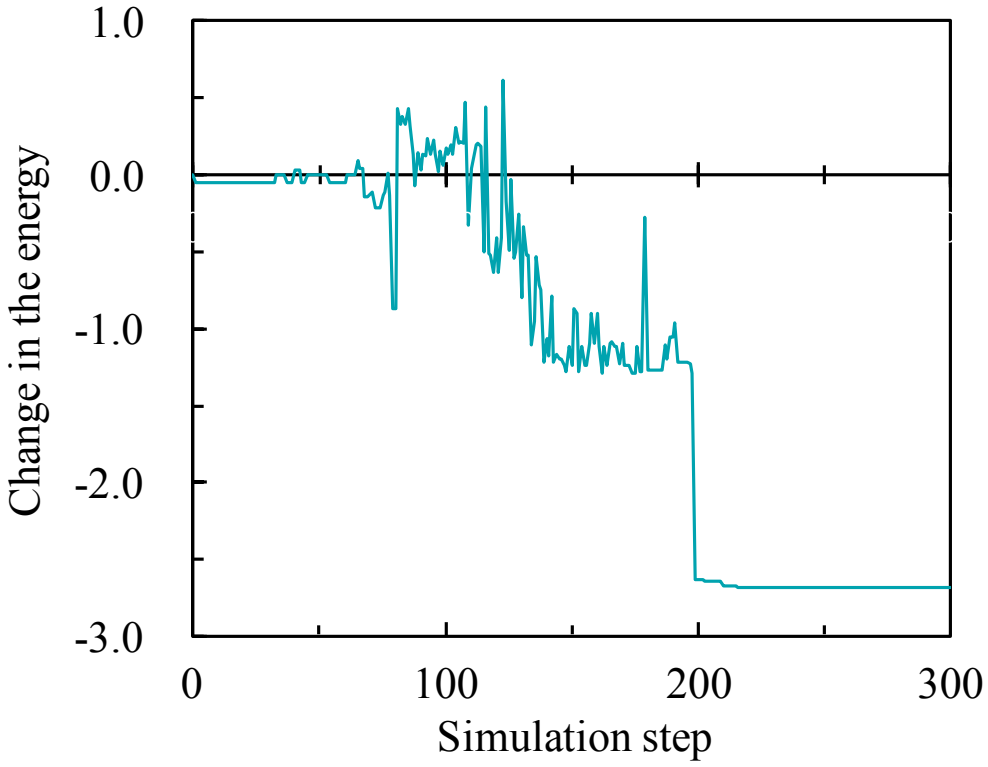

Figure 4.14 System energy history during the transformation process shown in Figure 4.12.

Figure 4.15 shows the ratios of the irregularly shaped clusters that transformed into stable configurations, namely perfect loops or Frank loops. It is evident that almost half the clusters transformed into either perfect loops or Frank loops. This indicates that EM/BCS can simulate the transformation process of irregularly shaped defect clusters into stable configurations, which can occur far beyond the typical MD timescale.

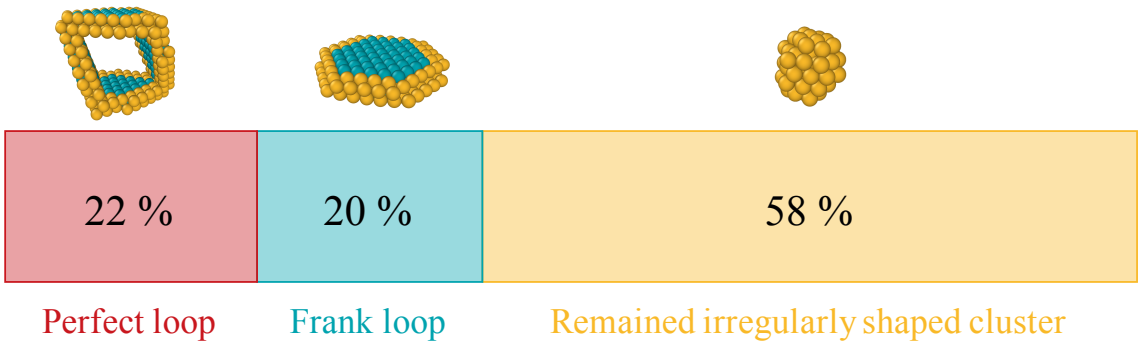

Figure 4.15 Ratio of irregularly shaped clusters that transformed into stable configurations.

At each transformation process, the system experienced state-to-state transitions through multiple basin hops on the PES; the highest E_a of all the hops corresponded to the activation energy of the rate-determining process, which controls the occurrence frequency of the whole transformation. Figure 4.16 shows the activation energy of the rate-determining process for the transformation of the irregularly shaped SIA clusters shown in Figure 4.10 (a), for 20 repeated calculations. Note that EM/BCS is stochastic, and the obtained transformation processes, i.e., the PES path that the system passes through, can be different between the repeated calculations. As seen in the figure, in the 20 calculations, a cluster transformed into a Frank loop in 18 cases, and into a perfect loop in the other 2 cases. In addition, we observed a difference in the activation energy of the rate-determining process up to ~1.8 eV in the 18 cases where the cluster transformed into a Frank loop. This indicates that the system went through a totally different PES path in these cases, depending on the repeated calculation. In real situations, the transformation process tends to occur with as low an E_a value as possible. Judging from the results shown in Figure 4.16, the paths of calculation ID 7 and 8 are energetically favorable paths on the PES, with a rate-determining process activation energy of ~0.82 eV. Meanwhile, when performing a larger number of repeated calculations, we could find paths that have a further low rate-determining process activation energy. This means that it is not practical to find the MEP of the transformation process by using EM/BCS because there is no reliable criterion to know whether a found path is an MEP or not. From this we deduce a way to discuss the obtained results: the results indicate only that there is a PES path where the cluster transforms into a stable configuration with an activation energy of ~0.82 eV, and not that the activation energy required for traveling the MEP is ~0.82 eV. In other words, EM/BCS can estimate the activation energy necessary for the transformation of a

cluster into a stable configuration, while it does not guarantee that the estimated activation energy is that for the MEP.

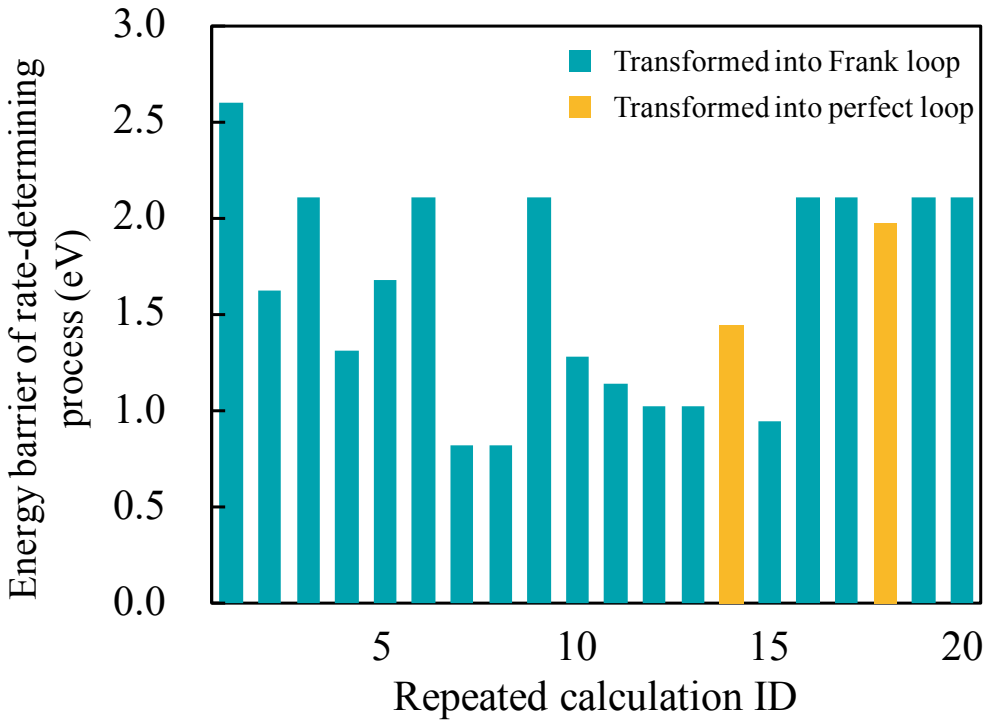

Figure 4.16 Activation energies of the rate-determining process for 20 repeated calculations.

SEAKMC is also a meso-timescale simulation technique; thus, it is very fruitful to compare the obtained results between SEAKMC and EM/BCS in order to contrast their features. Figure 4.17 shows the behavior of the irregularly shaped cluster shown in Figure 4.10 (a) when SEAKMC was employed under a condition comparable to that when EM/BCS was employed. It is evident that only trivial changes in the cluster configuration were observed throughout the simulation, and the cluster shape hardly changed even after 300 steps. This means that the system was hopping only around basins located closely beyond very low E_a values (Flicker events). Although we performed the simulation over several hundred steps, no transformation into a stable configuration like that observed in EM/BCS simulations was observed.

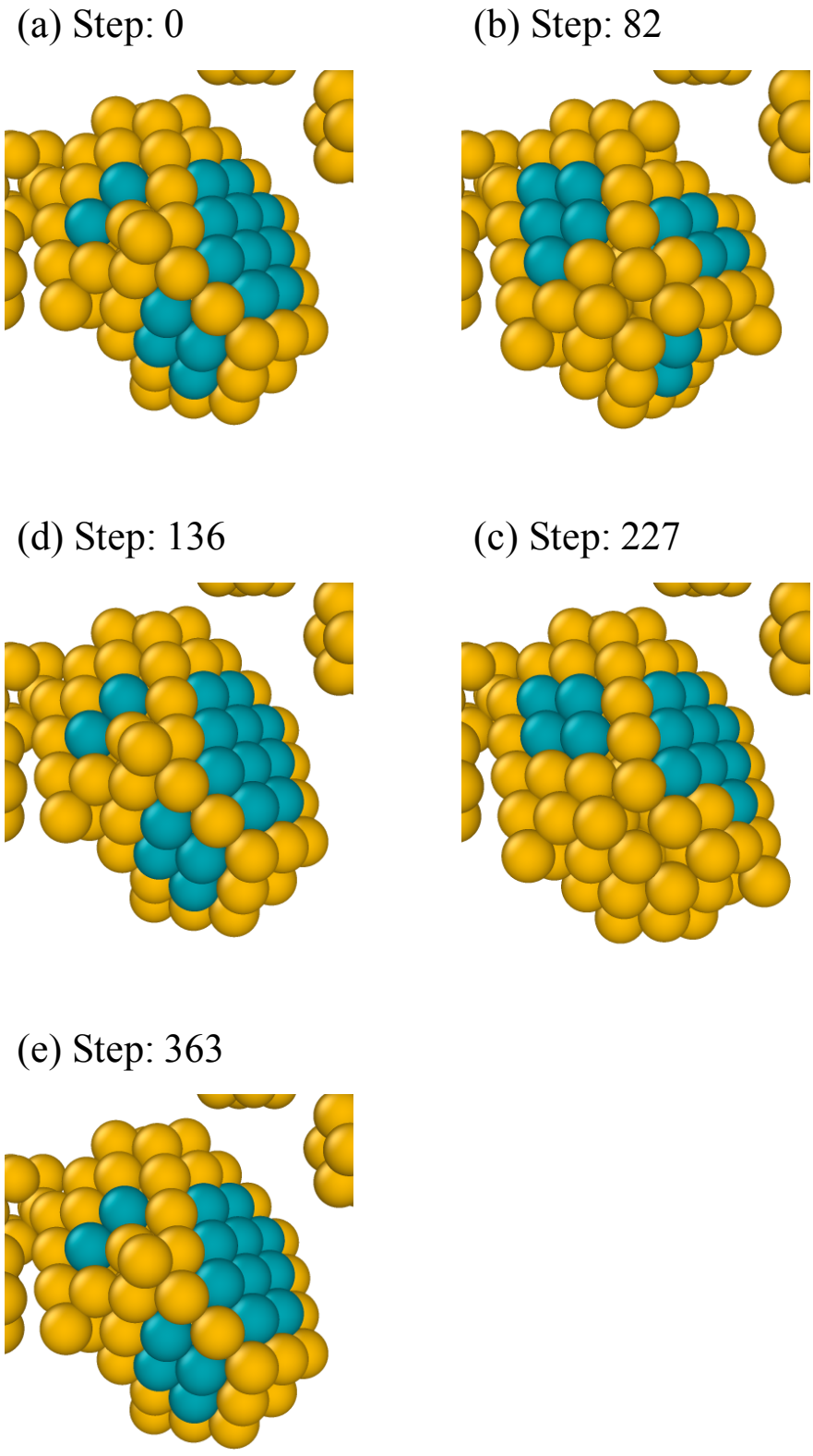

Figure 4.17. Behavior of an irregularly shaped cluster when simulated using SEAKMC.

Figure 4.18 shows the values of E_a that the system experienced at each step during the simulation of the irregularly shaped cluster shown in Figure 4.10 (a): (a) the simulation by EM/BCS and (b) that by SEAKMC. Note that the values of E_a are not plotted at all the steps in Figure 4.18 (a), because the event occurred stochastically at each step in the simulations by EM/BCS. It is evident that almost all the E_a values observed in the SEAKMC simulation were lower than 0.2 eV, while events with relatively high E_a were observed in the simulation by EM/BCS even though the conducted simulation steps are considerably fewer than in SEAKMC. The difference stems from the fact that flicker events were chosen with a relatively high probability in the SEAKMC event selection once the flicker events were found and listed in the event list. For other irregularly shaped clusters simulated in this study, we often observed such hindrance of the transformation caused by flicker events, while the transformation of the same cluster was observed in the application of EM/BCS. These results indicate that EM/BCS reduced the effect of flicker events on the transformation process, which was a serious problem when SEAKMC was employed.

On the other hand, we should bear in mind that the results above do not necessarily mean EM/BCS is superior to SEAKMC in general. One of the critical differences between EM/BCS and SEAKMC lies in the manner of event selection. In SEAKMC, events with a lower E_a are preferentially chosen when low-energy events and high-energy events are listed together in the event list. Because of this, the system may need to go through a vast number of simulation steps if the event we desire to observe has a relatively high E_a. In EM/BCS, the acceptance probability of a found event is dependent only on the energy difference between the current basin and the found basin, meaning that the event can be accepted relatively easily even if basins that correspond to flicker events are located around the current basin. Meanwhile, EM/BCS is based on an optimization algorithm, and it cannot calculate the simulation time for the dynamics that the system experiences. The timescale of the dynamics can be estimated with the activation energy of the rate-determining process; still, it should be stressed that the simulated process does not exactly follow real dynamics. In this respect, the advantage of SEAKMC should be highlighted: SEAKMC can output simulation time and track accurate dynamics of the system under the assumption that all possible events are listed in the event list. For an application that investigates the stable configuration of microstructure, as in this study, EM/BCS seems more suitable because it is less affected by flicker events. On the other

hand, when the simulation time itself is of interest, or when no significant energy decrease is expected throughout the simulation, SEAKMC would be more suitable. Understanding the features of each method and their compatibility with the nature of the focus problem is quite important for effective meso-timescale modeling (Table 4.2).

Table 4.2 Comparison between EM/BCS and SEAKMC.

SEAKMC	EM/BCS
○ Simulate dynamics itself	△ Search for the PES path toward the energetically favorable state
○ Calculate the simulated time	× Cannot calculate the simulated time
○ Derive the energy barriers the system experiences	○ Derive the energy barriers the system experiences
× Significant effect of flicker events	○ Less effect of flicker events

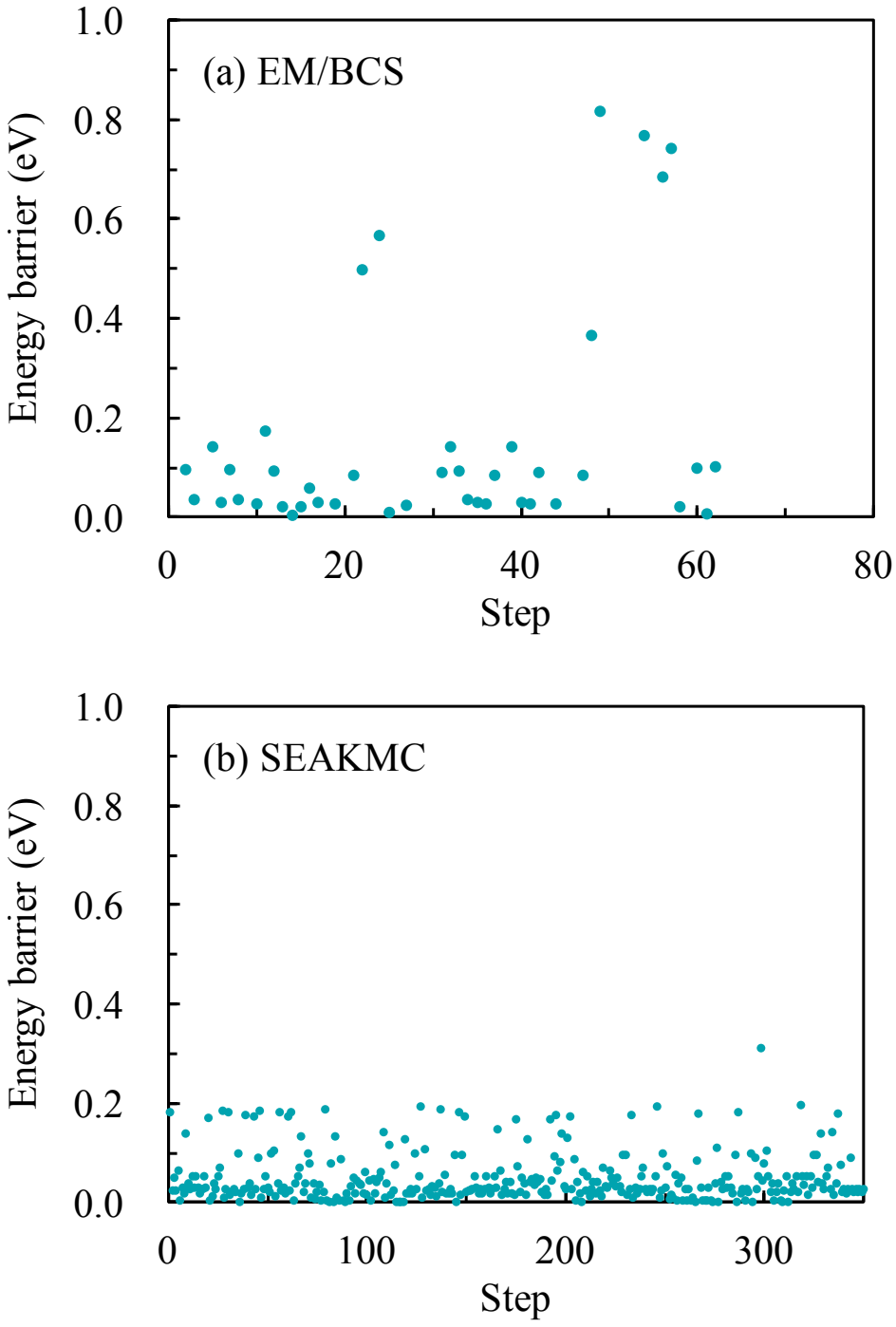

Figure 4.18. The values of E_a that the system experiences at each step during the simulation of the irregularly shaped cluster shown in Figure 4.10 (a): (a) simulation by EM/BCS and (b) that by SEAKMC.

4.4 Conclusions

- We developed a method to explore the stable configuration of microstructures based on an optimization algorithm (EM/BCS), in particular, TPSA. Note that the framework of EM/BCS is not limited to TPSA; other global optimization algorithms are also applicable, suggesting wide applicability of EM/BCS.
- EM/BCS was employed to investigate the stable configurations of irregularly shaped SIA clusters formed through displacement cascades. We found that almost half the clusters transformed into a stable configuration, namely, perfect loops or Frank loops, and that the change in the system energy was consistent with the cluster transformation process. This indicates that EM/BCS can accurately simulate the transformation process of the clusters.
- We observed that the clusters that did not transform into stable configurations in the SEAKMC simulations transformed into stable configurations when EM/BCS was employed. This suggests that EM/BCS reduced the effect of flicker events on the transformation process and efficiently simulated the events we desired to observe.
- We compared EM/BCS with SEAKMC and elaborated the characteristic features of both methods. Owing to the lesser effect by flicker events, application of EM/BCS would be more suitable if one is interested in energetically favorable system states, as in this study. Meanwhile, in the case where one would like to simulate real dynamics and obtain simulation time, the application of SEAKMC is preferable because EM/BCS does not track real dynamics or output simulation time. EM/BCS can only estimate the timescale of the occurrence of the dynamics through the E_a values that the system experiences, while there is no guarantee that the obtained E_a values are those of the MEP.

References in Chapter 4

[1] A. B. Bortz, M. H. Kalos and J. L. Lebowitz, "A new algorithm for Monte Carlo simulation of ising spin systems," *Journal of Computational Physics,* vol. 17, pp. 10–18, 1975.

[2] D. T. Gillespie, "Monte Carlo simulation of random walks with residence time dependent transition probability rates," vol. 28, pp. 395–407, 1978.

[3] K. Kimura and K. Taki, "Time-homogeneous parallel annealing algorithm," in *The 13th IMACS World Congress of Computation and Applied Mathematics*, Dublin, 1991.

[4] K. Konishi, K. Taki and K. Kimura, "Temperature parallel simulated annealing algorithm and its evaluation," *Transaction on Information Processing Society of Japan,* vol. 36, pp. 797–807, 1995.

[5] S. Kirkpatrick, C. D. Gelett Jr. and M. P. Vecchi, "Optimization by simulated annealing," *Science,* vol. 220, pp. 671–680, 1983.

[6] M. Miki, T. Hiroyasu, J. Wako and T. Yoshida, "Adaptive temperature schedule determined by generic algorithm for parallel siulated annealing," in *The 2003 Congress on Evolutionary Computation*, Canberra, 2003.

[7] E. L. Piccolomini and F. Zama, "The conjugate gradient regularization method in computed tomography problems," *Applied Mathematics and Computation,* vol. 102, pp. 87–99, 1999.

[8] W. Cai and L. Ma, "Applications of critical temperature in minimizing functions of continuous variables with simulated annealing algorithm," *Computer Physics Communications,* vol. 181, pp. 11–16, 2010.

[9] W. Cai, D. J. Ewing and L. Ma, "Application of simulated annealing for multispectral tomography," *Computer Physics Communications,* vol. 179, pp. 250–255, 2008.

[10] A. Corana, M. Marchesi, C. Martini and S. Ridella, "Minimizing multimodal functions of continuous variables with the ‘‘simulated annealing’’ algorithm," *ACM Transactions on Mathematical Software (TOMS),* vol. 13, pp. 262–280, 1987.

[11] L. Ma and W. Cai, "Determination of the optimal regularization parameters in hyperspectral tomography," *Applied Optics,* vol. 47, pp. 4186–4192, 2008.

[12] L. Ma and W. Cai, "Numerical investigation of hyperspectral tomography for simultaneous temperature and concentration imaging," *Applied Optics,* vol. 47, pp.

3751–3759, 2008.

[13] L. Ma, W. Cai, A. W. Caswell, T. Kraetscmer, S. T. Sanders, S. Roy and J. R. Gord, "Tomographic imaging of temperature and chemical species based onhyperspectral absorption spectroscopy," *Optics Express,* vol. 17, pp. 8602–8613, 2009.

[14] W. H. Press, B. P. Flannery, S. A. Teukolsky and W. T. Vetterling, Numerical Recipes in FORTRAN, The Art of Scientific Computing, Cambridge: Cambridge University Press, 2007.

[15] E. Aarts and J. Korst, Simulated annealing and Boltzmann machines, New York: Wiley, 1989.

[16] L. Ingber, "Simulated Annealing: Practice versus Theory," *American Journal of Mathematical and Computer Modelling,* vol. 18, pp. 29–57, 1993.

[17] H. Szu and R. Hartley, "Fast simulated annealing," *Physics Letters A,* vol. 122, pp. 157–162, 1987.

[18] N. Metropolis, A. Rosenbluth, M. Rosenbluth and A. Teller, "Equation of state calculations by fast computing machines," *Journal of Chemical Physics,* vol. 21, pp. 1087–1092, 1953.

[19] S. Geman and D. Geman, "Stochastic relaxation, Gibbs distributions, and the Bayesian restoration of images," *IEEE Transactions on Pattern Analysis and Machine Intelligence,* vol. 6, pp. 721–741, 1984.

[20] K. Holmqvist, A. Migdalas and P. M. Pardalos, "Parallelized heuristics for combinatorial search," in *Parallel Computing in Optimization*, Boston, Springer, 1997, pp. 269–294.

[21] S. W. Mahfoud and D. E. Goldberg, "Parallel recombinative simulated annealing: a genetic algorithm," *Parallel Computing,* vol. 21, pp. 1–28, 19995.

[22] J. P. Leite and B. H. Topping, "Parallel simulated annealing for structural optimization," *Computer & Structures,* vol. 73, pp. 545–564, 1999.

[23] E. E. Witte, R. D. Chamberlain and M. A. Franklin, "Parallel simulated annealing using speculative computation," *IEEE Transactions on Parallel and Distributed Systems,* vol. 2, pp. 483–494, 1991.

[24] K. Konishi, M. Yashki and K. Taki, "An Application of Temperature Parallel Simulated Annealing to the Traveling Salesman Problem and its Efficient Implementation on the Distributed Memory Parallel Machine," *1996 Joint Symposium of Parallel Processing,*

*p*p. 153–160, 1996.

[25] M. Miki, T. Hiroyasu and M. Kasai, "Application of the temperature parallel simulated annealing to continuous optimization problems," *JSPP,* vol. 41, pp. 1607–1616, 1999.

[26] M. Miki, T. Hiroyasu, M. Kasai, K. Ono and T. Jitta, "Temperature parallel simulated annealing with adaptive neighborhood for continuous optimization problem," *Computational Intelligence and Applications,* pp. 149–154, 2002.

[27] W. Cai, D. J. Ewing and L. Ma, "Investigation of temperature parallel simulated annealing for optimizing continuous functions with application to hyperspectral tomography," *Applied Mathematics and Computation,* vol. 217, pp. 5754–5767, 2011.

[28] B. Rosen, "Functional Optimization based on Advance Simulated Annealing," IEEE Workshop on Physics and Computation, pp. 289–293, 1992.

[29] H. Szu and R. Hartley, "Fast simulated annealing," *Physics Letters A,* vol. 122, pp. 157–162, 1987.

[30] H. Date , K. Taki, “A standard cell placement program based on the time-homogeneous simulated annealing method,” *Proceedings of the annual conference of the Japanese Society for Artificial Intelligence,* vol. 7, pp. 31–34, 1993.

Chapter 5 Summary

5.1 Summary of this dissertation

Ensuring the integrity of the structural materials in artifact systems is essential because it directly correlates to their subsequent safety. Computational approaches are useful for understanding the behavior of the structural materials while considering drastically changing social environments which surround the system. Since material property changes are governed by changes on a microstructural level, we need to investigate material behavior based on phenomena at an atomistic scale. The lengthscales and timescales that each simulation method requires, varies between atomistic and macroscopic scales, resulting in the necessity of schemes that seamlessly bridge these scale gaps. Regarding multi-lengthscale schemes, several pioneering studies have focused on extending the accessible lengthscale while maintaining atomistic fidelity. For the multi-timescale schemes, however, there has been a lack of sufficient schemes that bridge the timescale gaps between each simulation method. In other words, there is an ever-growing demand to fill this gap in the multi-timescale simulation technology arena to challenge conventional simulation methods.

Based on this, we improved and developed multi-timescale simulation methods that have both the capability of meso-timescale simulation and atomistic fidelity. The results and insights obtained in this dissertation are summarized below.

Chapter 2

MD simulations were performed to investigate the defect formation process through displacement cascades in FCC metals. We focused on the SFE dependence and subsequent strain effect of the defect formation. Through additional MD and MS simulations, we calculated defect formation energies and discussed the results of the MD simulations. We note that the collision phase occurs in the order of 10^{-15} s and involves complex atomistic dynamics. With a fidelity which reaches the atomic vibration level, the MD technique is best suited for cascade simulations. The results and insights obtained here provide useful inputs for larger-scale models used to simulate meso-timescale phenomena, which are beyond the scope of MD. The results obtained in Chapter 2 include:

- There was no clear SFE dependence of the number of residual defects, and the applied strain did not change this trend. On the other hand, the absolute number of residual defects increased under the applied strain, owing to the change in the formation energy of a Frenkel pair.
- While we observed little SFE dependence of the size distribution of SIA clusters, the applied strain enhanced the formation of larger SIA clusters more strongly. This is because the decrease in formation energy due to the applied strain was more significant for larger SIA clusters than for smaller ones.
- The number of SIA perfect loops increased with a decrease in SFE. Under the applied strain, the absolute number of SIA perfect loops increased over the whole SFE range, while the trend with respect to SFE was not affected This trend led to a higher ratio of glissile SIA clusters at lower SFE. We found that the difference in formation energy between an SIA Frank loop and an SIA perfect loop was a key factor of preferential formation of SIA perfect loops at lower SFE. Because the ratio of glissile SIA clusters significantly affects subsequent microstructural evolution, the results indicate that it is very important to consider the effect of strains when modeling the defect formation process in FCC metals through displacement cascades.

Chapter 3

On-the-fly kMC techniques have gathered much attention in recent years as effective meso-timescale simulation methods with atomistic fidelity. With this method, the event list is re-constructed at each step in accordance with the system state at that moment, which enables the simulation of complex dynamics beyond our intuition. SEAKMC is one of these on-the-fly kMC techniques, and it introduces quite a unique concept of AV. The employment of AV significantly reduces calculation costs and allows for the treatment of relatively large system sizes of over 100,000 atoms. Hence, SEAKMC is a promising on-the-fly kMC technique, and improvements in SEAKMC will significantly contribute to an improvement in multi-timescale modeling schemes. In Chapter 3, we worked on improving SEAKMC by focusing on the acceleration of the SPS procedure, which represents a calculation bottleneck in SEAKMC simulations.

- Two acceleration schemes were proposed: the first scheme (i) is a multi-step procedure of SPS with increasing AV size, where a relatively small AV was first introduced, followed by SPSs with larger AVs to obtain an SP with the desired accuracy. Here, we used the result from the small-AV SPSs as an input. The second scheme (ii) recycles SPs sampled in the preceding steps as an input for the current-step SPSs. We simulated bulk diffusion of point defects in iron using the acceleration schemes as a benchmark. The resulting acceleration was increased significantly by a factor of ~100 in scheme (ii) and ~6–8 in scheme (i).

- Following this, we proposed a hybrid acceleration scheme of schemes (i) and (ii), referred to as the 'prediction-based SPS'. One of the notable benefits of the prediction-based SPS is, that as the simulation proceeds, increased acceleration is achieved owing to the more frequent use of scheme (ii), whose acceleration is more significant than scheme (i). Furthermore, the stored information on AV and SP configurations can also be used for other calculation cases, such as repeated and varying temperature calculations. This means that through the construction of a vast database of AV and SP configurations, we can conduct greatly accelerated SEAKMC simulations, relying mostly on scheme (ii).

- Using SEAKMC with prediction-based SPS, we simulated the bulk diffusion of a 3-SIAs cluster in iron. We observed significant acceleration of the simulations was achieved while maintaining atomistic fidelity. In addition, we confirmed that prediction-based SPS has a considerably weakened dependence on the calculation cost on AV size. This indicates that the exponential increase in calculation cost observed with increased AV size, which has been one of the major problems of SEAKMC, can be mitigated through the employment of prediction-based SPS.

- We applied accelerated SEAKMC to the investigation of meso-timescale evolution of an irregularly shaped sessile SIA cluster observed in the MD cascade simulations discussed in Chapter 2. The transformation of the cluster into a Frank loop was observed in several calculation cases, and the required time for the transformation almost reached the limit of the timescale accessible to MD. In addition, the cluster was further transformed into a perfect loop in some of the cases in which the

transformation into a Frank loop was observed. It should be highlighted that the transformation into a perfect loop took ~100 times longer than the MD timescale, i.e., on the order of nanoseconds. These results indicate that SEAKMC can track complex atomistic behavior while reaching a timescale far beyond that of MD, demonstrating the promising potential of SEAKMC to reveal mechanisms of various meso-timescale phenomena that have not been clarified through the use of conventional simulation methods.

Chapter 4

- We developed a method to explore the energetically stable state of microstructures in materials based on an optimization algorithm, which we refer to as the energy minimization with basins-constructed space (EM/BCS). TPSA was used as the optimization algorithm because it is a global optimization algorithm and the generation of the next-step solution is based on a neighborhood search. Note that, in principle, another optimization algorithm can also be implemented in EM/BCS. This means that, depending on the nature of the problem, a suitable optimization algorithm can be implemented to efficiently explore the stable state.

- We applied EM/BCS to irregularly shaped sessile SIA clusters observed in the MD simulations of Chapter 2, and subsequently investigated the stable configurations which these clusters transformed into beyond the MD timescale. Almost half of the clusters transformed into stable configurations, namely, a Frank loop or a perfect loop. The transformation processes were consistent with the system energy changes, indicating that EM/BCS can correctly simulate the transition process of an irregularly shaped defect cluster into an energetically stable state.

- By applying EM/BCS, we were able to observe the transformation process for some clusters that did not transform into a stable configuration using SEAKMC simulations. This is because most simulation steps in SEAKMC simulations are spent on simulating flicker events of clusters, showing that EM/BCS can mitigate the effect of flicker events.

- We compared the characteristic features of EM/BCS and SEAKMC. If one is

interested in the stable state of the system, as in this study, EM/BCS is more suitable due to its lighter effect of flicker events. However, it should be stressed that EM/BCS is based on an optimization algorithm, and therefore, cannot accurately track the dynamics of the system. In other words, if one is interested in the system dynamics or would like to evaluate the required time for a certain phenomenon, or if the change in system energy is insignificant, SEAKMC is preferred. Each method has its own advantages and disadvantages; it is therefore very important to understand the characteristics of the methods as well as the nature of the focused problem in order to conduct effective meso-timescale simulations.

To date, numerous computational atomistic studies employed classical simulation methods, such as MD and conventional kMC., and constructing a multi-scale model has remained a challenging task for many decades. Further, adding to the challenge, there has been a lack of development of schemes that bridge the timescale gap between each simulation method. The accelerated SEAKMC and EM/BCS possess the efficiency, the atomistic fidelity, and the meso-timescale simulation capabilities necessary to provide a breakthrough to the current shortfalls of multi-timescale simulation technology (Figure 5.1). The obtained results in this dissertation have the potential to elevate current multi-scale simulation technologies to the next level, and significantly contribute to predicting the behavior of structural materials based on computational approaches.

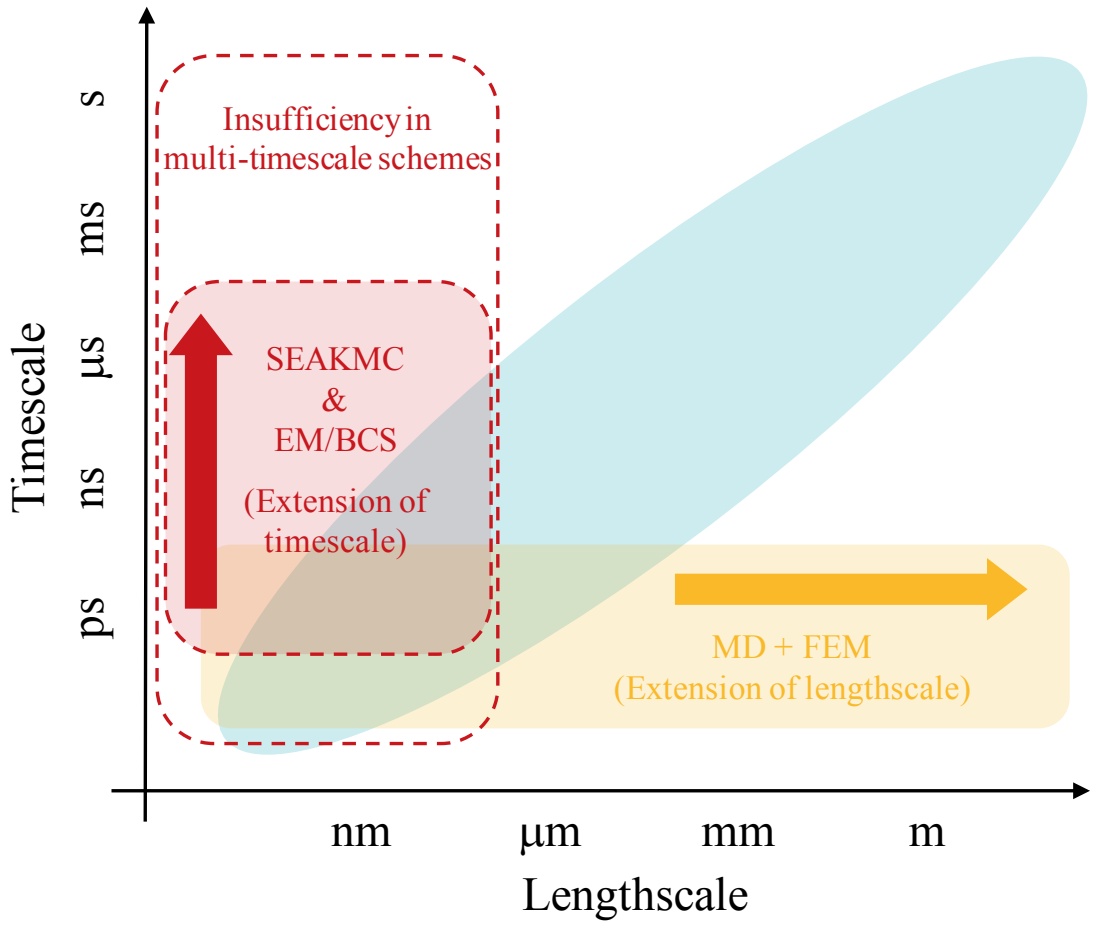

Figure 5.1 Extension of the timescale through SEAKMC and EM/BCS.

5.2 Challenges and future prospects

Here, we mention the challenges and future prospects of accelerated SEAKMC and EM/BCS.

Application to various meso-timescale phenomena

By using accelerated SEAKMC and EM/BCS, we aim to reveal the mechanisms of various meso-timescale phenomena from atomistic perspectives which have not been clarified under the use of conventional simulation methods. This is exemplified by the process of transformation of an SIA Frank loop into an SIA perfect loop. Some experimental studies have confirmed the unfaulting of SIA Frank loops, that is, a stacking fault on the habit plane of the loop is removed and an SIA perfect loop is formed [1,2]. However, their detailed

mechanism is not well known because of the spatial and time resolution limits of TEM. A treatment within the framework of elasticity theory has also been employed; and yet, the detailed mechanism was unclear due to the lack of atomistic fidelity. A recent MD study reported the unfaulting of an SIA Frank loop, wherein even the direct contact of an SIA Frank loop with a gliding dislocation does not always lead to the loop unfaulting in the MD timescale [3]. This dissertation has however confirmed that an SIA Frank loop can transform into a perfect loop without any direct interaction with other defects through meso-timescale SEAKMC simulations on the order of nanoseconds with the atomistic fidelity. This result occurred due to the compatibility of the atomistic fidelity and the meso-timescale simulation capabilities of SEAKMC, and further research aims to reveal the detailed mechanisms of the transformation in order to obtain insights for quantifying microstructural evolution in materials.

Another example is the mechanism of the coalescence between microstructures, such as SIA clusters and bubbles/voids. These microstructures have been known to migrate within materials and grow through coalescence with the same type of microstructures. These coalescence events have been observed in experimental studies, and their significant effects on microstructural evolution have been recognized for many decades [4,5]. Because their elementally process involves complex atomic diffusion dynamics, their detailed mechanisms have not been clarified through analytical or experimental approaches. In addition, modeling of coalescence events using conventional atomistic simulation methods has been a challenging task owing to their occurrence in the experimental timescale. However, by utilizing the accelerated SEAKMC and EM/BCS simulations, we have confirmed that complex atomic diffusions can be precisely tracked while reaching timescales that vastly exceed that of MD, demonstrating that the accelerated SEAKMC and EM/BCS can precisely simulate such phenomena involving the coalescence of microstructures. Furthermore, the occurrence timescale is comparable to that of experiments, indicating that the study is also meaningful from the perspective of the validation of the methods with experimental results.

There have been numerous puzzling problems under the use of conventional simulation methods for many decades. The accelerated SEAKMC and EM/BCS has the potential to contribute to clarifying unknown mechanisms of various meso-timescale phenomena in future studies.

Limitations of the accelerated SEAKMC and EM/BCS

The accelerated SEAKMC and EM/BCS has broad applications: not limited purely to the structural materials of nuclear power plants. However, the limitations of the application should also be noted. The accelerated SEAKMC and EM/BCS focuses on a specific phenomenon of a microstructure in a specific region at nanometer-scale. The simulated dynamics does therefore not always represent the dynamics of the entire material. For instance, a climb-enhanced glide of dislocations is known as one of the controlling mechanisms for thermal creep in metallic materials, where dislocations are de-pinned by obstacles through climb motion induced by the absorption of vacancies and they continue to glide beyond the obstacles. To accurately model this mechanism, focus must be placed on the dynamics of dislocations, obstacles and vacancies, and the simulation of the absorption process of vacancies by the dislocations. Indeed, the accelerated SEAKMC and EM/BCS are suitable to such dynamics, capable of evaluating the effects of various conditions, such as temperature and applied stress, on the dynamics. Meanwhile, it is also known that a dominant mechanism for thermal creep is highly dependent on conditions, e.g., atomic diffusion along grain boundaries can be another dominant mechanism, particularly in low temperature conditions. There is therefore no guarantee that the simulated dynamics is always a key mechanism for the focused materials degradation, and importantly, the inappropriate extrapolation of the obtained results could, in some cases, occur inadvertently.

For mitigating this limitation, the extension of lengthscale in order to cover phenomena in wider regions would be one solution. In the example above, one can use a relatively large system that encompasses dislocations and grain boundaries together, so that both mechanisms can be simulated in accordance with the conditions. This fact eventually leads us to the consideration of the balance between accessible lengthscales and timescales, because the calculation costs of the two scales are usually not compatible. Because of this, it is very important to recognize the lengthscale and timescale to be simulated, as well as the nature of the problem, and to model the dynamics with these considerations in mind.

Deriving interatomic forces based on first principle

In this dissertation, we used interatomic potential functions that treat only a single element when performing accelerated SEAKMC and EM/BCS simulations. One of the well-known limitations of the use of these potential functions is that it is difficult to treat

multicomponent systems and that the type of available elements is limited. In general, practical materials contain various minor elements and impurities, and even a concentration of only 0.1 % can drastically change the material properties. It is therefore unfeasible to directly model the behavior of practical materials using simulation methods with currently existing empirical interatomic methods. When considering the employment of first principle MD, which can, in principle, incorporate several types of elements, we also face an inevitable simulation hurdle due to the limited system size on the order of hundreds of atoms. For instance, to model the behavior of the diffusion and interaction of 0.1 % minor elements, a system with a minimum of 10^4–10^5 atoms is necessary, because only one out of 1000 atoms in the system corresponds to the minor element. Furthermore, the energy barrier of typical diffusion events varies around 1.0 eV, meaning that even classical MD cannot sufficiently treat the dynamics of minor elements. Therefore, it is desperate to model the behavior of minor elements by using first principle MD in terms of both lengthscales and timescales. The framework of the accelerated SEAKMC and EM/BCS affords derivation of interatomic forces based on first principle. Moreover, these techniques employ AVs during simulations, which means that we need only to give freedom to the minor elements and the atoms surrounding them. This considerably lessens the effect of a large system size on the calculation costs. It should also be stressed that the accelerated SEAKMC and EM/BCS are very suitable for simulating meso-timescale dynamics, such as diffusion, since their algorithms are based on state-to-state dynamics.

The accelerated SEAKMC and EM/BCS, based on first principle, have promising potential to produce valuable insights that contribute to the integrity of structural materials in practical use. Conventionally, the prediction of materials degradation and the evaluation of the integrity of structural materials have tended to be conservative due to the variation of the results of material testing prior to their service operation. This has forced the safety margin to be larger than it is supposed to, leading to limitations in the materials use below the performance they potentially have. One of the main factors for the variation is the presence of minor elements and impurities, their content, and the change in their distribution during the operation period. Meanwhile, the employment of the accelerated SEAKMC and EM/BCS, based on first principle, enables the incorporation of the behavior of minor elements and impurities, significantly contributing to revealing the mechanisms of degradation phenomena

in practical materials; concurrently opening the possibility of reducing variations in observed materials behavior. Consequently, it would be possible to design structural materials so that the materials exhibit their best performance and to define reasonable safety margins based on reliable scientific grounds, which we wish will be addressed in future studies.

References in Chapter 5

[1] T. Okita, W. G. Wolfer, F. A. Garner and N. Sekimura, “Effects of titanium additions to austenitic ternary alloys on microstructural evolution and void swelling,” *Philosophical Magazine*, vol. 85, pp. 2033–2048, 2005.

[2] G. V. Saada, Paper presented at the International Conference on Crystal Lattice Defects, *Conference Journal of the Physical Society of Japan*, vol. 18, pp. 41, 1963.

[3] S. Hayakawa, Y. Hayashi, T. Okita, M. Itakura, K. Suzuki and Y. Kuriyama, "Effects of stacking fault energies on the interaction between an edge dislocation and an 8.0-nm-diameter Frank loop of self-interstitial atoms," *Nuclear Materials and Energy,* vol. 9, pp. 581–586, 2016.

[4] J. A. Turnbull, “The coalescence of dislocation loops by self climb,” *Philosophical Magazine*, vol. 21, pp. 83–94, 1970.

[5] R. Trocellier, S. Agarwal and S. Miro, “A review on helium mobility in inorganic materials,” *Journal of Nuclear Materials*, vol. 445, pp. 128–142, 2014. and references therein.